Synthesis and Characterization of Vertical and Horizontal Nanowires for Functional Device Fabrication

Dissertation

Zur Erlangung des akademischen Grades
Doktor der Ingenieurwissenschaften
(Dr.-Ing.)
der Technischen Fakultät
der Christian-Albrechts-Universität zu Kiel

Seid Jebril

Kiel
2010

1. Gutachter:	Prof. Dr. Rainer Adelung
2. Gutachter:	Prof. Dr. Helmut Föll
3. Gutachter:	Prof. Dr. Lorenz Kienle
4. Gutachter:	Prof. Dr. Achim Walter Hassel
Datum der mündlichen Prüfung:	29.10.2009

Acknowledgments

I would like to take this opportunity to express my deep gratitude to all of the people who accompanied and supported me throughout my PhD period.

First and foremost, my sincerest gratitude to my supervisor Prof. Dr. Rainer Adelung for consistent and considerate guidance, insight advice and fruitful scientific discussions. His supervision improved not only my research ability but also broadened my view as well as my interest in the field of material science.

I also avail this opportunity to express my heartiest thanks to Prof. Dr. Franz Faupel for his enormous support during my study and for allowing me to work in his laboratory.

I would like to express my sincere thanks to Prof. Dr. Lorenz Kienle and his coworker Dr. Andriy Lotnyk for characterizing the ZnO nanstructures by transmission electron microscope tirelessly.

It is a great pleasure to me to express my sincere thanks to Dr. B. Schmidt in Forschungszentrum Dresden-Rossendorf, Institute of Ion Beam Physics and Materials Research for his collaboration in preparing the microstructured photoresist by photo-lithography.

I am deeply thankfull to Dr. V. Cimalla and Prof. O. Ambacher (Fraunhofer Institut für Angewandte Festkörperphysik, Freiburg) for doing the ZnO ozone test.

I gratefully thank Dr. D. Kabiraj and Dr. D. Avasti, Inter University Accelerator Center (IUAC) India, for their cooperation in measuring deep temperature electrical current measurement.

It is pleasure for me to express my sincere thanks to Prof. Dr. Klaus Ratzke, Dr. Vladimir Zaporojtchenko and Dr. Thomas Strunskus for their enormous support during my study.

I would like to express my especial gratefulness to Dipl.-Ing. Stefan Rehders for constructing the deposition chamber and for his expertise in solving technical problems and Dipl.-Ing. Rainer Kloth for fast computer problem solving.

Many thanks to our secretaries Mrs. Christiane Otte-Hüls, Dipl.-Chem. Sieglinde Kastaun and Dipl.-Geol. Beate Minten for their help concerning official work.

I would like thank students who did many of the experiments during their master and bachelor thesis: MSc. Dawit Minale, MSc. Samia Essa, MSc. Kittitat Subannajui, MSc. Getachew Tizazu, Arnim Schuchardt and MSc. Hanna Kuhlmann.

I would like to thank Dr. Yogendra Kumar Mishra and Maria Claus for doing some of the experiments specially for synthesizing the ZnO nanoseaurchins. Special thanks to Dipl.-Min. Marlies Schwitzke for teaching me how to use the scanning electron microscopy.

My special thanks to all my friends specially Dr.-Ing. Haile Takele, Dr.-Ing. Mady Elbahri, Dipl.-Ing Chem. Christina Pakula, M.Sc. Muhammad Qasim Shaikh, M.Sc. Venkata Sai Kiran Chakravadhanula, Dr.-Ing. Sebastian Wille, Dr.-Ing. Christian Hanisch and Dipl.-Ing. Sören Kaps. And I also deeply thank all members in the group of Functional nanomaterials and Multicomponent Materials who helped me directly or indirectly in completing my thesis work successfully and for creating a very good working atmosphere.

Certainly, I greatly appreciate the financial support extended to me by the German Research Foundation (DFG).

Last but most, I would like to express my heartiest thanks to my family: my father Jebril Mohammed, my brothers: Mohammed Jebril, Hamdihun Jebril, Ali Jebril, Kedir Jebril and my sisters: Hannan Jebril, Hayat Jebril and Fetiha Jebril for their endless love and support. I am very thankful to Mr. Beyene Aleme for encouraging and motivating me throughout my study.

Contents

Acknowledgments I

1 Introduction 1
1.1 Nanotechnology . . . 1
1.2 Organization of The Thesis . . . 2

2 Theoretical Considerations 3
2.1 Size Effect on Properties of Materials . . . 3
2.2 Electrical Transport in Nanostructures . . . 7
2.2.1 Diffusive and Ballistic Transport . . . 7
2.2.2 Quantum Tunneling . . . 8
2.2.3 Temperature Dependence of Conductivity . . . 11
2.3 Nanowire Synthesis Techniques . . . 13
2.3.1 Thin Film Fracture . . . 14
2.3.2 Vapor-Liquid-Solid Growth Mechanism . . . 17

3 Material Deposition Techniques 20
3.1 Spin Coating . . . 20
3.1.1 Photolithography based Resist Microstructuring . . . 22
3.2 Physical Vapor Deposition . . . 23
3.2.1 Thin Film Deposition by Evaporation . . . 25
3.2.2 Thin Film Deposition by Sputtering . . . 27
3.2.3 *In-Situ* Film Thickness Monitoring . . . 28
3.2.4 Atomistic Film Growth . . . 31

4 Characterization Techniques 34
4.1 Light Microscopy . . . 34
4.2 Atomic force microscopy . . . 35
4.2.1 Probe-Sample Interaction . . . 37
4.3 Scanning Electron Microscopy . . . 39
4.3.1 Principle of Operation . . . 40
4.3.2 Electron-Sample Interactions . . . 42
4.4 Energy Dispersive X-Ray Analysis . . . 44
4.5 Transmission Electron Microscopy . . . 46
4.6 X-ray Photoelectron Spectroscopy . . . 49

4.7 Electrical Measurement Device 51

5 Synthesis and Characterization of Horizontal Nanowires 53
5.1 Experimental Details 54
5.1.1 Nanowire Fabrication 54
5.2 Results and Discussion 65
5.2.1 Electrical Characterization of Nanowires 65
5.3 Conclusion 90

6 Synthesis and Characterization of Vertical Nanowires 92
6.1 Synthesis and Characterization of ZnO Nanosail 93
6.1.1 Experimental Details 94
6.1.2 Result and Discussion 97
6.2 Synthesis and Characterization of ZnO Nanoseaurchins 107
6.2.1 Experimental Details 108
6.2.2 Result and Discussion 109
6.3 Conclusion 114

7 Summary and Outlook 116

Bibliography XVI

List of Figures XXIV

List of Publications and Patent XXV

1 Introduction

1.1 Nanotechnology

Nanotechnology is a design, synthesis and implementation of nanostructures or nanomaterials. It paves a way for fundamental understanding of materials' dimension and their corresponding physical properties for a desired application. Synthesis and processing of nanostructures are the essential aspects of nanotechnology. Studies on their new physical properties and applications are possible only when nanostructured materials are made available with desired size, morphology, microstructure and chemical composition. In general, there are two philosophically distinct approaches for creating small objects: top-down and bottom-up. In the top-down approach, small features are patterned in bulk materials by a combination of lithography, etching and deposition to form functional devices and their integrated systems. The top-down approach has been exceedingly successful in many venues, with perhaps, microelectronics being the best example today. While developments continue to push the resolution limits of the top-down approach, these improvements in resolution are associated with a near exponential increase in cost associated with each new level of manufacturing facility. Whereas, in the bottom-up approach the functional structures are assembled from well defined chemically and/or physically synthesized nanoscale building blocks. The optimization of this bottom-up approach for nanotechnology requires a focus on two key areas that are at the heart of devices and integration processes. First of all, the bottom-up approach necessitates nanoscale building blocks with precisely controlled and tunable chemical composition, structure, size and morphology, as these characteristics determine their corresponding physical properties. To meet this goal, it requires developing methods that enable rational design and predictable synthesis of building blocks. Secondly, it is critical to explore and develop

the limits of functional devices based on these building blocks. In this doctoral work, the above basic principles are taken into consideration for the selection of both vertical and horizontal nanowire fabrication techniques, the integration of the synthesized functional nanowires into device and their characterization under different conditions.

1.2 Organization of The Thesis

This dissertation is organized into seven chapters including the current one. **Chapter** 2 discusses some of the theoretical concepts of the low dimensional systems. It begins with introducing the size effect on properties of materials. The two types of electron transport mechanisms and the basic concept of the nanowire synthesis techniques are also presented. **Chapter** 3 discusses the techniques used for various thin film deposition: resist and various metals. Details about the resist film preparation and microstructuring processes which were used mainly for a horizontal nanowire synthesis is explained. The metal film deposition technique and some of its basic concepts regarding the atomistic thin film growth mechanisms are also discussed. This technique is used mainly for two different purposes: for deposition of a nanowire material and for catalyst preparation for horizontal and vertical (mainly for Vapor-liquid-solid technique) nanowire synthesis, respectively. The characterization techniques which are used to elemental, morphological, and structural analysis of these nanostructures are also briefly discussed in **chapter** 4. The next two chapters focus on the main work of the dissertation which discuss the three different techniques of various nanowire synthesis. On one hand, **Chapter** 5 presents the thin film fracture based synthesis of horizontal nanowires. In this chapter, the basic processing steps as well as various investigation of the as-synthesized and locally oxidized nanowires are discussed. On the other hand, **chapter** 6 presents the vertical nanowires synthesized by two different techniques: Vapor-liquid-solid and direct oxidation of metal powder. The discussion regarding elemental and morphological analysis, their electrical as well as various sensoric properties are also included. Finally, **chapter** 7 concludes the dissertation with a summary of the principal results and brief experimental discussions followed by an outlook.

2 Theoretical Considerations

The present chapter discusses the basic theories of the observed phenomena in low dimensional systems. It is divided into three main sections. The fist section introduces some of the concepts associated with electron states in one dimensional systems such as nanowires. The second section discusses selectively the two electron transport mechanisms which is observed on dimensionally constrained materials. Finally, the basic concepts regarding the two main techniques used for the here-synthesized horizontally and vertically aligned nanowires will also be briefly presented.

2.1 Size Effect on Properties of Materials

Reduced dimensionality arises when at least one dimension of a physically active region is small compared to a relevant scale length. As a result, condensed matters exhibits some remarkable peculiar properties, such as physical, chemical etc., when their dimension changes from bulk to nanoscale. The unique properties exhibited by nanostructures, in general, can be attributed to different origins: for example, due to large fraction of surface atoms, large surface energy, spatial confinement etc. Some of the observed phenomena are as follows:

- Significantly low melting point or phase transition temperature and appreciably reduced lattice constant, due to huge fraction of surface atoms.
- One or two order magnitude higher mechanical strength. This effect could be due to reduced probability of defects.
- A high resistivity due to dominant surface and grain boundary scattering.
- Significantly different optical properties due to an increase in band gap etc.

The dimension dependence of these properties shows that the general physical behavior of a material can be tuned considerably by adjusting its shape or size. One of the simplest illustration of low dimension behavior is the particle in a box, by considering a rectangular structure with a flat potential inside (taken as zero) and infinitely high mathematically sharp walls. The three dimensional Schrödinger equation of an electron can be written as follows;

$$-\frac{\hbar^2}{2m^*}\nabla^2\psi(x,y,z)+V(x,y,z)\psi(x,y,z)=E\psi(x,y,z) \tag{2.1}$$

where m^* is the effective mass of an electron. Considering a nanowire, the total potential $V(x,y,z)$ can be written as the sum of a two dimensional confinement potential plus the potential along the wire. The potential along the axis can be best set to zero by considering its length as infinite when compared to its cross-section (thickness).

$$V(x,y,z)=V(x)+V(y,z) \tag{2.2}$$

The eigenfunction can be written as the product of the free carrier solution which is a plane wave and the confined solutions as written in equation 2.3

$$\psi(x,y,z)=\psi(x)\psi(y,z)=\varphi_{n,m}(r)\exp\frac{ik_x x}{L} \tag{2.3}$$

where r is the position vector in the yz plane parallel to the wire cross-section and L is the normalization length of the wire. The function $\varphi_{n,m}(r)$ satisfies the two dimensional Schrödinger equation.

$$-\frac{\hbar^2}{2m^*}\nabla^2\psi_{n,m}(y,z)+V(y,z)\psi_{n,m}(y,z)=E\psi_{n,m}(y,z) \tag{2.4}$$

As a model system, the wire can be considered as a rectangular cross-section and assume the potential $V(y,z)$ to be infinite out side of the wire. Then $\psi_{n,m}(y,z)$ equals

$$\psi_{n,m}(y,z)=\left(\frac{4}{L_yL_z}\right)^{\frac{1}{2}}\sin(\frac{n\pi y}{L_y})\sin(\frac{m\pi z}{L_z}) \tag{2.5}$$

where n, m = 1, 2, 3... and L_y and L_z are the dimensions in the y and z-directions, respectively. Since the motion is taken to be free electron-like, it leads

to a continuum of states called subbands with energies

$$E_{k_x,n,m} = E_{k_x} + E_{n,m} = \frac{\hbar^2\kappa_x^2}{2m^*} + \frac{n^2\hbar^2\pi^2}{2m^*L_y^2} + \frac{m^2\hbar^2\pi^2}{2m^*L_z^2} \tag{2.6}$$

Thus in the effective mass approximation, the motion along the axis of the wire can be described by a parabolic dispersion relation.
The density of states is defined as the number of states (N) per unit energy and per unit volume of real space, which can be expressed mathematically as

$$\rho(E) = \frac{dN}{dE} \tag{2.7}$$

Hence, for nanowires the total number of states N is equal to the length of the line in **k**-space ($2\kappa_x$), divided by the length occupied by one state ($2\pi/L$), and divided by the length in real space;

$$N^{1D} = 2 \times 2\kappa_x \frac{1}{2\pi/L}\frac{1}{L} \tag{2.8}$$

The "2" prefactor accounts for the spin degeneracy. Therefore

$$N^{1D} = \frac{4\kappa_x}{2\pi} \tag{2.9}$$

and thus

$$\frac{dN^{1D}}{d\kappa_x} = \frac{2}{\pi} \tag{2.10}$$

The density of states for a one dimensional wire is:

$$\rho^{1D}(E) = \frac{dN^{1D}}{dE} = \frac{dN^{1D}}{d\kappa}\frac{d\kappa_x}{dE} \tag{2.11}$$

From equation 2.6, the energy dispersion along the axis is still a parabola:

$$\frac{d\kappa_x}{dE} = \left(\frac{2m^*}{\hbar^2}\right)^{\frac{1}{2}} \frac{E^{-\frac{1}{2}}}{2} \tag{2.12}$$

Then equations 2.10 and 2.12 result in

$$\rho^{1D}(E) = \left(\frac{2m^*}{\hbar^2}\right)^{\frac{1}{2}} \frac{1}{\pi E^{\frac{1}{2}}} \tag{2.13}$$

where the energy E is measured upwards from a subband minimum. Comparing the density of states for bulk (3D), quantum wells (2D) and quantum wires (1D), a successive reduction in the freedom of the electron motion results in a reduction in the functional form of the density of state by factors of $E^{\frac{1}{2}}$. Figure 2.1 summarizes the relationship among the different dimension of materials with their corresponding density of states.

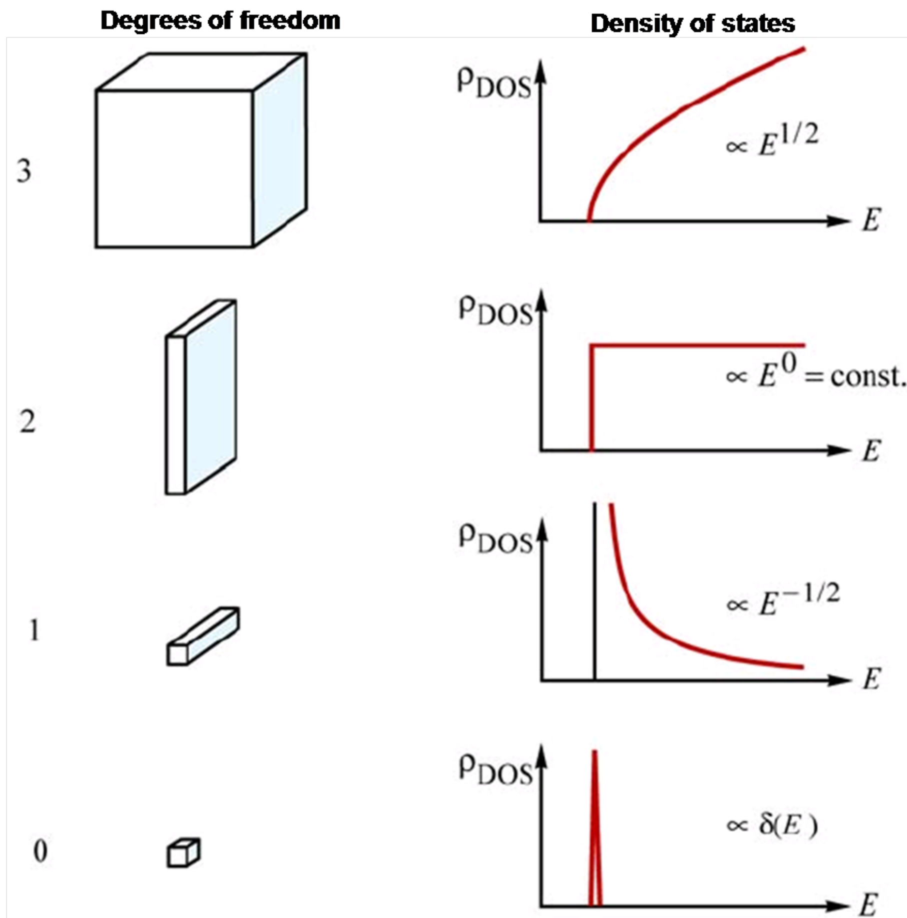

Figure 2.1: *Schematic illustrating of electronic density of states (DOS) with their corresponding degree of freedom . Systems with* 3*,* 2*,* 1 *and* 0 *dimensions can be referred as bulk, quantum well, quantum wire and quantum dots, respectively.*

2.2 Electrical Transport in Nanostructures

The electrical transport process of low dimensional structures depends on many physical scale lengths such as screening length, Fermi wave length, mean free path, coherence length, thermal length etc. Among these property determining factors, the influence of electron mean free path and Fermi wave length on the property of the materials will only be discussed in the following subsection. The quantum tunneling as well as the temperature dependence of conductivity will also be discussed.

2.2.1 Diffusive and Ballistic Transport

The electrical transport mechanism can be ballistic or diffusive depending on the size of lateral dimensions as well as the type of a nanowire (e.g. single crystal, polycrystalline etc.). For instance, as the length of the wire (L) is reduced to the mean free path of an electron l (*i.e.* the average distance between two consecutive collisions) the electron transport mechanism changes from diffusive to ballistic as shown in Figure 2.2. The diffusive electron transport ($L > l$) is mainly as a result of numerous scattering events (e.g. grain boundary or defects) [1] and can be observed in macroscopic materials as well as in polycrystalline nanowires. Whereas, a ballistic electron transport occurs when the length of the conductor is smaller than the electron mean free path ($L < l$) phenomenon of electrons traveling from one electrode to another without scattering. In this case, the conductivity of the conductor no longer depends on its length.

When the width of the wire (W) is further reduced to the wave length of electrons at the Fermi surface (called Fermi wavelength) λ_F (*i.e* $w \ll \lambda_F$), the conductance through the nanowire will be quantized in a step of $2e^2/h$ where e is the electron charge and h is plank's constant. Thus, the conductance will be independent of the length of the wire. In typical bulk metals the Fermi wavelength associated with the conduction electron Bloch waves is on the order of 0.1 nm. This short wavelength is due to the high spatial density of electrons.

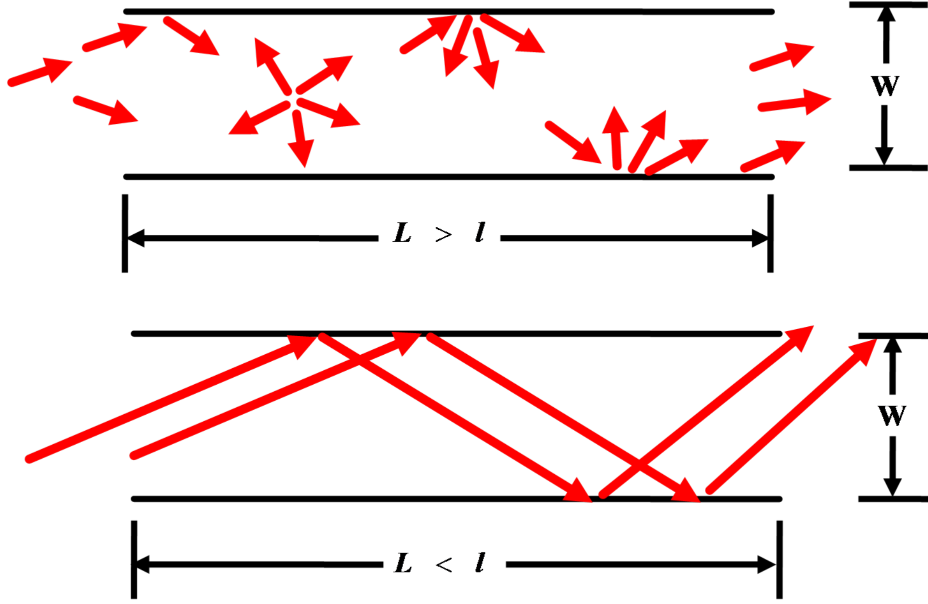

Figure 2.2: *Sketch showing the two possible electron transport mechanisms. Diffusive electron transport. Numerous scattering (top) and ballistic electron transport: Electrons are only backscattered at the boundary (bottom). l refers to the mean free path of the conduction electrons.*

2.2.2 Quantum Tunneling

Tunneling is a phenomenon which involves a charge transport through an insulating media separating two conductors that are extremely closely spaced. It is an evanescent wave coupling effect that occurs in the context of quantum mechanics at which the behavior of particles is governed by Schrödinger's wave equation. Considering a particle (e.g., an electron) with energy E approaching from the left to a finite potential barrier U, where $E < U$ and width L as schematically shown in Figure 2.3 (top), the wave associated with the particle can be described by a time independent Schrödinger equation. On both sides of the barrier (region I and III) $U = 0$ where no force acts on the particle, the one dimension Schrödinger's equation of the particle takes the form:

$$\frac{\hbar^2}{2m^*}\frac{d^2\psi_I}{dx^2} + (E)\,\psi_I = 0 \tag{2.14}$$

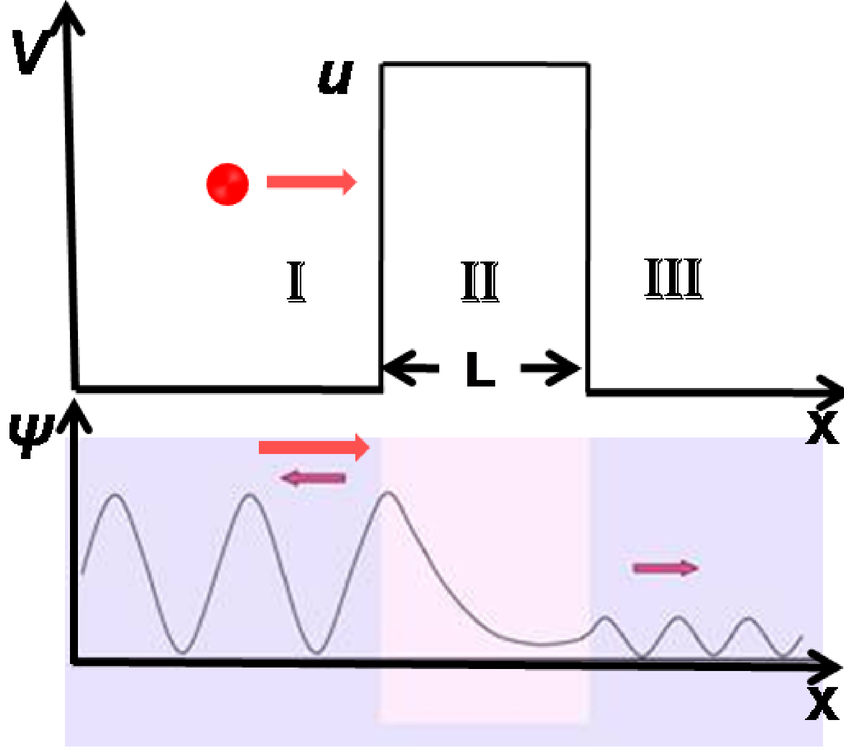

Figure 2.3: *Sketch showing quantum tunneling: finite potential wall (top) and the incident, partly reflected and partly transmitted wave function of the particle as the function of distance (x) (bottom).*

$$\frac{\hbar^2}{2m^*}\frac{d^2\psi_{III}}{dx^2} + (E)\,\psi_{III} = 0 \tag{2.15}$$

where m^* is the effective mass, h is Planck's constant and ψ_I and ψ_{III} are the wave function of the particle at region I and III, respectively. Like wise, the Schrödinger equation of the particle inside the potential barrier can also be written as

$$\frac{\hbar^2}{2m^*}\frac{d^2\psi_{II}}{dx^2} + (E-U)\,\psi_{II} = 0 \tag{2.16}$$

where ψ_{II} is the wave function of the particle inside the barrier.
The corresponding possible solutions to these equations which represent the wave function of the particle at the three different regions are :

$$\psi_I = Ae^{ik_1x} + Be^{-ik} \tag{2.17}$$

$$\psi_{II} = Ce^{ik_2x} + De^{k_2x} \tag{2.18}$$

$$\psi_{III} = Fe^{ik_1x} \tag{2.19}$$

where k_1=$\sqrt{2m^*E}/\hbar$ and k_2=$\sqrt{2m^*(U-E)}/\hbar$ represent the wave number of the de Broglie waves outside and inside the barrier, respectively and A, B, C, D and F are coefficients. The incident particle which encounters the potential barrier faces two phenomena: transmission and reflection from the barrier. In order calculate the transmission probability T, appropriate boundary conditions to ψ_I, ψ_{II} and ψ_{III} should be applied [2]. Thus, considering these conditions A/F ratio yields

$$\frac{A}{F} = \left[\frac{1}{2} + \frac{i}{4}\left(\frac{k_2}{k_1} - \frac{k_1}{k_2}\right)\right] e^{(ik_1+k_2)L} + \left[\frac{1}{2} - \frac{i}{4}\left(\frac{k_2}{k_1} - \frac{k_1}{k_2}\right)\right] e^{(ik_1-k_2)L} \tag{2.20}$$

Assuming that the potential barrier U is high relative to the energy E of the incident particle (i.e., $k_2/k_1 > k_1/k_2$), the ratio of the wave numbers can be approximated as follows

$$\frac{k_2}{k_1} - \frac{k_1}{k_2} \approx \frac{k_2}{k_1} \tag{2.21}$$

The width of the barrier can also be considered as wide enough so that ψ_{II} will be severely weakened inside the barrier. This means that $k_2L >> 1$ and $e^{k_2L} >> e^{-k_2L}$. Hence, (A/F) ratio in equation 2.20 can be approximated as

$$\frac{A}{F} = \left[\frac{1}{2} + \frac{ik_2}{4k_1}\right] e^{(ik_1+k_2)L} \tag{2.22}$$

By considering the complex conjugate of (A/F), the transmission probability T of the particle can then be described as

$$T = \left(\frac{AA^*}{FF^*}\right)^{-1} = \left[\frac{16}{4 + \left(\frac{k_1}{k_2}\right)^2}\right] e^{-2k_2L} \tag{2.23}$$

After substituting the corresponding values of k_1 and k_2, the ratio of the wave numbers $(k_2/k_1)^2$ in equation 2.23 yields

$$\left(\frac{k_2}{k_1}\right)^2 = \frac{U}{E} - 1 \tag{2.24}$$

This shows that the value in the square bracket of equation 2.23 varies much less with E and U than does the exponential. Thus, a reasonable approximation of the transmission probability of the incident particle is

$$T \approx e^{-2k_2 L} \tag{2.25}$$

Equation 2.25 shows that the width of the barrier plays a role on the tunneling probability of the particle *i.e.,* the smaller the barrier thickness is , the higher the tunneling probability will be. Hence, it is possible for a particle to be found in the other side of the potential barrier even if it has lower energy than the barrier, which is classically forbidden. This kind of description can be used to explain the tunneling of an electron between metal clusters or grains which are insulated by a nano scale medium (*e.g,* thin oxide films). For instance, a thin, non-conducting layer sandwiched between a metal grains can be referred as a barrier potential and can be treated mathematically as discussed above. Figure 2.3 (bottom) an example of a typical wave function for an incident and transmitted particle.

2.2.3 Temperature Dependence of Conductivity

The electronic transport depends in general on the density of states (ρ), the position of the Fermi level, the temperature and the applied field [3]. The tunneling transition of electronic carriers from occupied to unoccupied states involves one or more phonons, and is called ”hopping”. When both the number of phonons and the energy decrease, the hopping between states that are closer in energy (even if they are wider spaced) becomes more preferable than that between the nearest neighbors whose energies differ substantially. This mechanism is known as variable range hopping (VRH) conductivity, or Mott's conductivity which is often used to describe a low temperature conductivity in strongly disordered systems with localized states.
The quantum confinement of carriers in the one dimensional materials changes their electronic energy states significantly, and makes the transport properties of these systems very different from their bulk counterparts. Some of the experimental data on the resistance of metal nanowires, for example, have been explained by hopping mechanisms [4, 5] which is an exponential dependence on

temperature as

$$R(T) = R_\infty \exp[(\frac{T_0}{T})^\gamma] \tag{2.26}$$

where γ depends on the dimensionality d of the hopping process, and R_∞ and T_0 are material dependent constants.

$$\gamma = \frac{1}{1+d} \tag{2.27}$$

where d = 1, 2 and 3 for 1-D, 2-D and 3-D variable range hopping, respectively. For instance, the variable range hopping for one dimensional structures $\gamma = \frac{1}{2}$, the Mott's "$T^{\frac{1}{2}}$" law can be rewritten as;

$$R(T) = R_\infty \exp[(\frac{T_0}{T})^{\frac{1}{2}}] \tag{2.28}$$

where

$$T_0 = \frac{18}{k_B \xi_L^3 \rho(E_f} \tag{2.29}$$

where $\rho(E_F)$ electronic density of states at the Fermi level, ξ is the localization length (spatial extension of localized wave function) and k_B Boltzmann constant. The basic concept of electron localization (ξ) was first introduced by Anderson [6] and named after him. Anderson pointed out that the electric wave function in a random potential may be profoundly altered if the randomness is sufficiently strong. The traditional view had been that scattering by the random potential causes the Bloch waves to loose phase coherence on the length scale of the mean free path l. Nevertheless, the wave function remains extended through out the sample. Anderson pointed out that if the disorder is very strong, the wave function may become localized, in that the wave function decays exponentialy from some point in space *i.e.*,

$$|\varphi(r)| \sim exp\left(\frac{|\mathbf{r}-\mathbf{r}_0|}{\xi}\right) \tag{2.30}$$

At a particular temperature, the probability of an electron hopping from one localized state to another depends on two parameters; R the spatial separation of the sites, and W their energy separation. The range R between two sites determines the probability of hopping between them, thus the shorter the range the greater the hopping probability, but as conduction through the material is a re-

sult of chains of successive hops, it is the "average nearest-neighbor range" which governs the conductivity. Following Mott, the probability of hopping between two states of spatial separation R and energy separation W has the form:

$$P \sim exp(-2\alpha R - \frac{W}{kT}) \tag{2.31}$$

where α^{-1} is the attenuation length for a hydrogen-like localized wave function. Rewriting 2.31 gives

$$P \sim exp(-R^{'} + W^{'}) = exp(-\Re) \tag{2.32}$$

where $R^{'} = 2\alpha R$, $W^{'} = W/kT$ and $\Re = R^{'} + W^{'}$ is the range between the two states. The particular hop is represented by a point in a plane defined by $R^{'}$ and $W^{'}$ axes.
The states can be regarded as points in a four-dimensional random array (three spatial coordinates and one energy coordinate) where the 'distance' between two states is given by the range $\Re$. The probability of hopping between two states is determined by the "distance" $\Re$ between them, and the shorter this "distance" the greater the hopping probability. Conduction is the result of many series of hops through this four-dimensional array, and as short-range hops are favored, it is the average nearest-neighbor "distance" between states in this four-dimensional space which determines the overall conductivity.

2.3 Nanowire Synthesis Techniques

The nanowire synthesis techniques used in this work are based on three different approaches: the thin film fracture based for the horizontal nanowire formation, the direct oxidation method and vapor-liquid-solid (VLS) technique where both techniques are used for vertical nanowire synthesis. The coming sections merely discusses the basics of two of the techniques used (*i.e* both thin fracture properties of brittle films and VLS in general context) where as the direct oxidation technique will be discussed in section 6.2 for convenience.

2.3.1 Thin Film Fracture

The fracture behavior of thin films on a substrates differs from the bulk behavior due to the small film thickness and the presence of the substrate [7]. In contrast to the bulk behavior where a propagating crack of critical length leads to fracture and total failure, a cracked film may still remain bonded to the substrate. This leads to multiple crack formation since a single crack reduces the film stress in the film only locally as result of the constraining effect of the substrate. Thin films on a substrate are usually in a biaxial stress state, especially for thermal stresses induced by differences in thermal expansion coefficient between film and substrate. The constraining effect of the substrate on the released strain energy in thin film under biaxial stress is schematically compared in Figure 2.4 to a free standing sheet under uniaxial load.

In a free standing sheet, the volume V_{sheet} affected by the release of the energy

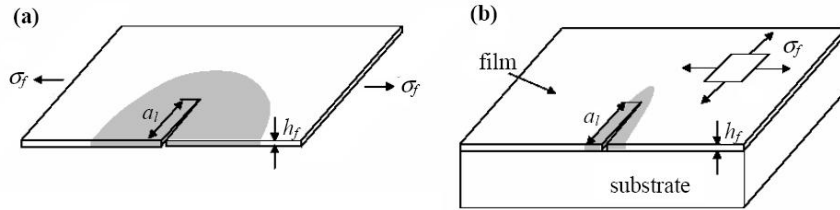

Figure 2.4: *The volume of strain energy released by the formation of a crack is larger in a freestanding film under uniaxial tension (a) than in a film bonded to a substrate subjected to a biaxial film stress (b).*

due to crack formation scales with the crack length a_l and the film thickness h_f according to equation 2.33

$$V_{sheet} \propto a_l^2 h_f \tag{2.33}$$

In contrast, for a film on a substrate, the volume V_{film} in which the strain energy is released yields a stronger influence of the film thickness due to the substrate constraint and scales as

$$V_{film} \propto a_l h_f^2 \tag{2.34}$$

For a film bonded by a substrate, the energy W_{el} released by the introduction of a crack is given by

$$W_{el} \propto -\frac{\sigma_{fr}^2}{E_f} a_l h_f^2 \tag{2.35}$$

where σ_{fr} is the film fracture-stress, defined as the maximum stress prior to crack formation, and E_f represents the plane-strain elastic modulus of the film. The energy release rate G is defined as the reduction of the elastic energy associated with a crack advancing by unit area A (where $A \propto a_l h_f$) is:

$$G = Z \frac{\sigma_{fr}^2 h_f}{E_f} \tag{2.36}$$

This dependency implies that the film thickness plays the role of a critical crack length. For homogeneous films, the driving force for crack propagation parallel to the surface is reached at every site along the film once the stress reaches the fracture stress. The crack propagation parallel to the surface is called channel cracking since the crack forms a channel of constant width as it propagates in the film. The parameter Z in equation 2.36 comprises the elastic mismatch between film and substrate and the crack geometry. There are different geometries for thin film cracking; Isolated surface cracks, crack channeling including the formation of a network of cracks, debonding at the film/substrate interface and crack penetration into the substrate.

One of the reasons for this induction of stress in films can be a thermal expansion difference between the film and the substrate. When the temperature is changed from some temperature T_0 to a different temperature T, the thick substrate acquires thermal strain, but remains stress-free [8]. The film also acquires a thermal strain which differs from that of the substrate by

$$\epsilon_T = \int_{T_0}^{T} (\alpha_f - \alpha_s) dT \tag{2.37}$$

where α_f and α_s are thermal expansion coefficients of the film and the substrate respectively. When the film and substrate are well bonded, the net in plane strain in the film is equal to the thermal strain of the substrate. So the mismatch strain in the above equation must be accommodated by elastic and inelastic deformation in the film. If the film remains elastic during the temperature change, this mismatch strain induces a biaxial stress in the plane of the film, σ_T, given

by

$$\sigma_T = \frac{E_f \epsilon_T}{1 - \nu_f} \tag{2.38}$$

where E_f is Young's modulus and ν_f is Poisson's ratio of the film. Stress can also be generated by applying a bending moment to the film-substrate composite in which the ductile substrate remain unfractured but brittle thin film fractures. So the total stress in the film is the sum of the gross stress, the thermal stress, and the applied stress.

2.3.1.1 Crack Driving Force and Crack Resistance

The crack driving force G is the elastic energy reduction associated with the crack advancing per unit area. The crack resistance Γ is the energy needed to advance the crack per unit area. A crack cannot grow when the driving force is below the resistance and grows when the driving force equals the resistance. The three locations of the crack resistance that is in the film, Γ_f, in the substrate, Γ_s, and on the interface, Γ_i, have different values. The crack resistance also depends on the crack velocity and on the environment. If a film is under tension and is brittle a possible failure mode is cracking in the film. The crack elongates laterally in the film until it meets the film edge or another crack. The lateral crack length can be many times the film thickness. This kind of crack is called a channel crack. Since the film may have many pre-existing flaws under a large stress, many channel cracks can form.
The origin of the first channel crack is from the worst pre-existing flaw in the film. Let h be the film thickness, σ the stress in the film and a the size of the pre-existing crack in the film, the crack driving force is given by [8].

$$G = k \frac{(1 - \nu_f^2)\sigma^2 a}{E_f} \tag{2.39}$$

where k is a parameter which is shape dependent. The pre-existing crack grows when the crack driving force G equals the crack resistance Γ_f that is

$$G = k \frac{(1 - \nu_f^2)\sigma^2 a}{E_f} = \Gamma_f \tag{2.40}$$

There are two cases: if $a << h$, the crack front runs both toward the interface and laterally in the film. In the other case if $a \approx h$, the crack can only elongate laterally in the film. When the lateral crack length exceeds several lengths to the film thickness, the driving force attains a steady state value.
A film under a tensile stress may debond from the root of a channel crack or from the edge of the film. When the debond length exceeds several times the film thickness, the debonding process attains a steady-state and the driving force becomes independent of the debond length. Under the plane strain conditions, the debond driving force is given by

$$G = \frac{(1-\nu_f^2)\sigma^2 h}{2E_f} \tag{2.41}$$

The film debonds steadily when the driving force equals the resistance, $G = \Gamma_i$. In general if stored elastic energy is greater or equal to the critical energy for fracture and delamination, then fracture and delamination may occur simultaneously.

2.3.2 Vapor-Liquid-Solid Growth Mechanism

The vapor liquid-solid technique was used for the synthesis of vertical ZnO nanowires (see 6.1). In this technique, a second phase material, commonly referred to as either an impurity or a catalyst is purposely introduced to confine the crystal growth. A catalyst forms a liquid droplet by itself or alloying with growth material during the growth, which acts as a trap of growth species. Enriched growth species in the catalyst droplets subsequently precipitates at the growth surface resulting in one dimensional growth.
The VLS technique was first described by Wagner [9] in 1964 by using a Au particles as catalysts to grow crystalline semiconductor whiskers from vapor sources such as $SiCl_4$ or SiH_4. The principle for Si whisker growth is schematically shown in Figure 2.5 (a). The Au particles deposited on the surface of an Si substrate react first with Si to form Au-Si alloy droplets at a certain temperature. As shown in the Au-Si phase diagram in Figure 2.5 (b), the melting temperature of the Au-Si alloy at the eutectic point is very low (about 363 °C at an Au:Si ratio of 4 : 1) compared with that of Au or Si. Au and Si can form a solid solution for all Si content (0-100%). In the case of Si deposition from the vapor mixture

of $SiCl_4$ and H_2, the reaction between $SiCl_4$ and H_2 happens at a temperature above 800 °C without the assistance of catalysts. Below this temperature, almost no deposition of Si occurs on the substrate surface [10]. At a temperature above 363 °C, Au particles can form Si-Au eutectic droplets on Si surfaces, and the reduction of Si occurs at the Au-Si droplets due to a catalytic effect. The Au-Si droplets absorb Si from the vapor phase resulting in a supersaturated state. Subsequently, the supersaturated silicon will diffuse from the liquid-vapor interface and precipitates at the solid-liquid interface resulting in the growth of the silicon. The growth will proceed in the solid-liquid interface as shown in Figure 2.5 (a). Once the growth species is adsorbed onto the liquid surface, it will dissolve into the liquid. The material transport in the liquid is diffusion controlled and occurs under essentially isothermal conditions. This technique, in general, is widely used for the synthesis of a variety of 1D nanomaterials that include elemental semiconductors [11, 12], II-VI semiconductors [13, 14] and III-V semiconductors [15, 16], oxides [17, 18] etc.

Some of the requirements for the VLS growth are summarized as follows [9]:

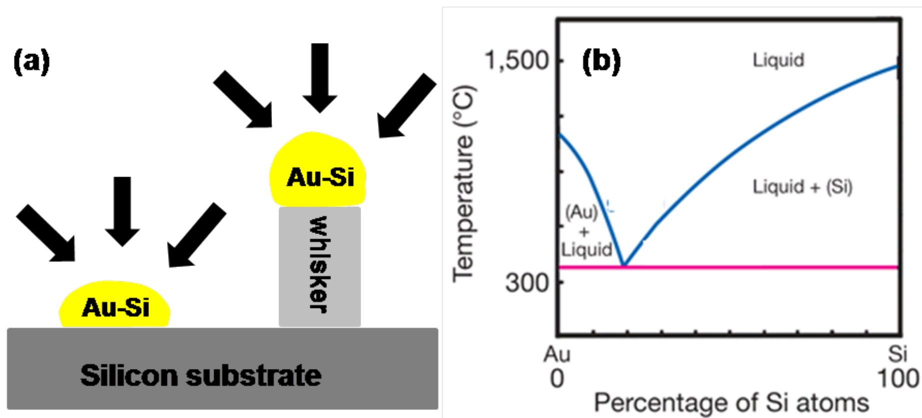

Figure 2.5: *Schematic showing the principal steps of VLS growth : initial nucleation and continued growth (a), and a phase diagram of Au-Si binary system (b).*

- The catalyst or impurity must be inert chemically. It must not react with chemical species such as by-products present in the growth chamber.
- The interfacial energy plays a very important role. The wetting characteristics influence the diameter of the grown nanowire. For a given volume of

liquid droplet, a small wetting angle results in a large growth area, leading to a large diameter of nanowires.

- The catalyst or impurity must form a liquid solution with the crystalline material to be grown at the deposition temperature.
- The distribution coefficient of the catalyst or impurity must be less than unity at the deposition temperature.

3 Material Deposition Techniques

Deposition of thin films has been a subject of intensive study for almost a century, and many methods have been developed and improved. Among the various techniques developed, electrochemical deposition, laser ablation, vacuum deposition (thermal evaporation or sputtering), and electron-beam physical vapor deposition are the most used in recent time.
This chapter discusses the three mainly used material deposition techniques: spin coating, thermal evaporation, and magnetron sputtering. The first section discusses spin coating which is a routinely used method for the formation of thin photoresist/polymer films under ambient condition. The next sections are devoted for the two main PVD techniques (*i.e.* evaporation and sputtering) which requires high vacuum conditions. Moreover, the principle of the *in-situ* thickness monitoring and the discussion about the atomistic film growth process will also be briefly presented .

3.1 Spin Coating

Spin coating is widely used in microelectronics to deposit photoresist and specialty polymers on flat surface at the start of the lithographic patterning process [19, 20]. In order to achieve high-fidelity lithography, a smooth, a uniform photoresist film of predictable and reproducible thickness is required. The spin coating process can be broken down into the four stages as shown in Figure 3.1. The deposition, spin-up, and spin-off stages occur sequentially while the evaporation stage occurs throughout the process, becoming the primary means of thinning near the end.

The deposition process involves the dispense of an excessive amount of fluid onto a stationary or slowly spinning substrate. The fluid is deposited through a

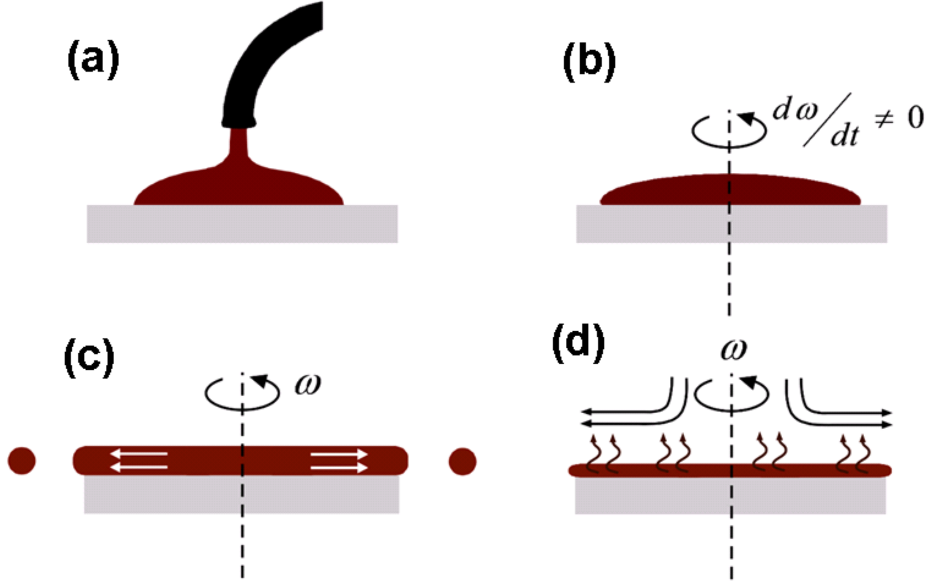

Figure 3.1: *Spin coating stages: deposition (a), spin-up (b), spin-off (c) and evaporation (d).*

nozzle at the center of the substrate or over some programmed path. An excessive amount of fluid is used to prevent coating discontinuities caused by the fluid front drying prior to it reaching the wafer edge.
In the spin up stage, the substrate is accelerated to the final spin speed. As rotational forces are transferred upward through the fluid, a wave front forms and flows to the substrate edge by centrifugal force, leaving a fairly uniform layer of photoresist behind.
The spin off stage is the spin coating stage where the excess solvent is flung off the substrate surface as it rotates at speeds between 2000 and 8000 rpm. The fluid is being thinned primarily by centrifugal forces until enough solvent has been removed to increase viscosity to a level where flow ceases.
When flow in the thin coating is no longer possible, evaporation takes over to further reduce the film thickness. A uniform film can be obtained when the viscosity is not dependent on shear rate (i.e. Newtonian) and the evaporation rate is independent of position. The thickness of a spin coated film, H, is given by [20]

$$H = \left(1 - \frac{\rho^0 A}{\rho A}\right)\left(\frac{3\eta e}{2\rho^0 A\omega^2}\right) \tag{3.1}$$

where ρA is the mass of the volatile solvent per unit volume, ρ^0A is its initial volume, ω is the angular velocity, η is the liquid viscosity, and e the evaporation rate, which is related to the mass transfer coefficient. Equation 3.1 reveals that the film thickness can be controlled by adjusting the solution properties and the deposition conditions.
The Shipley 1813 photoresist coating on a silicon substrate (76- mm diameter, p-doped, 1-10 Ωcm resistivity, 380 mm thick, ⟨100⟩ oriented and coated with 100nm thick thermally grown SiO_2) by spincoating (Spin-Coater GYRSET RC 518 (SUESS)) was then microstructured by using photolithography technique. This resist microstructuring was done in collaboration with Dr. Bernd Schmidt (Forschungszentrum Dresden-Rossendorf Institute of Ion Beam Physics and Materials Research, Dresden, Germany).

3.1.1 Photolithography based Resist Microstructuring

Lithography is also often referred to as photoengraving, and is the process of transferring a pattern into a reactive polymer, termed as resist, which will subsequently be used to replicate that pattern into an underlying thin film or substrate [21, 22]. Many techniques of lithography have been develop in the last decades with various lens systems and exposure radiation sources including photons, *x*-rays, electrons, ions and neutron atoms. These techniques share the same approaches and are based on similar fundamentals despite of having different exposure radiation sources. However, here, the resist microstructuring was mainly done by using photolithography (*i.e.*, using a UV light source) which is the most widely implemented technique in microelectronic fabrications.
Figure 3.2 (a) outlines some of the basic steps of photolithographic process, in which the positive resist material is applied as a thin coating over some base (e.g., silicon substrate) and subsequently exposed in an image wise fashion through a mask (shown in black line in (ii)), such that light strikes selected areas of the resist material. The exposed resist is then subjected to a development step. As the result, the exposed areas will be rendered more soluble in some developing solvent than the unexposed areas, thereby producing a positive tone image of the mask. These process are shown schematically in Figure 3.2 (a) (i-iii).
Figure 3.2 (b) shows the photo of the microstructured Shipley 1813 photore-

sist on the oxide coated silicon substrate. It consists of 24 equally sized ($\sim$ 1 cm^2) microchips, where three of them were differently microstructured. The microstructured resist was used as a base for the synthesis of well organized nanowires (discussed in chapter 5). The choice of the optimal thickness of the

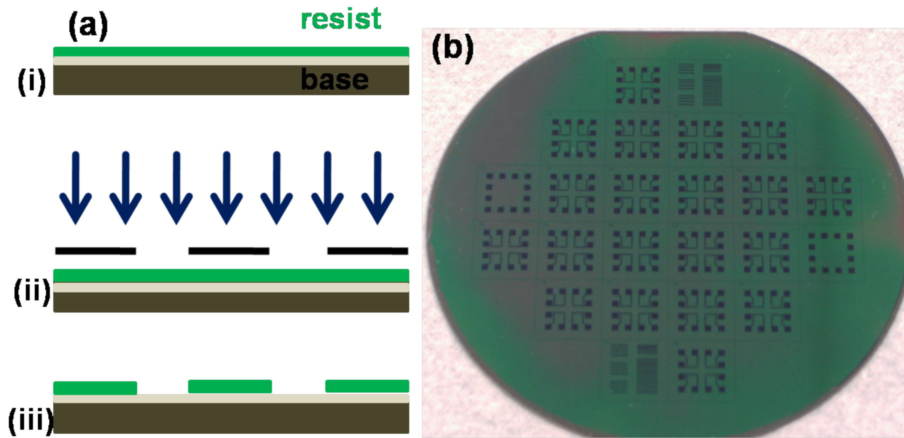

Figure 3.2: *Schematic representation of the photolithographic process sequence (a) such as positive resist coating (i), photoexposing (ii), and developing (iii), and the photo of the microstructured resist on a silicon wafer prepared by this technique (b).*

microstructured resist film to obtain a desirable cracks upon thermal cycling was done by analyzing the fracture properties of various thicknesses. Table 3.1 summarizes details of the microstructuring by photolithography on various thickness of the resist. All of the resists were subsequently hard baked at a temperature of 120 °C for 30 minutes in order to further improve the adhesion. The hard bake step concludes the photolithography sequence by creating the desired pattern on the wafer. The resist with thickness about 560 nm were found optimal for the desired crack formation and selectively used for the nanowire synthesis.

3.2 Physical Vapor Deposition

Physical vapor deposition (PVD) is a technique whereby physical processes, such as evaporation, sublimation, or ionic impingement on a target, facilitate the transfer of the atoms from a solid or molten source onto a substrate.

Table 3.1: *Details of the microstructuring process of various thickness of the resist by photo-lithography.*

Coating speed $[R/min]$	Soft-Bake [°C]/Time $[min]$	Light-exposing Time $[s]$	Development time$[s]$	Thickness $[nm]$
5000	100/30	2.0	30	580.6
5000	100/30	2.0	30	558.4
5000	120/30	2.0	65	446.8
5000	120/30	2.0	90	376.4
5000	100/30	2.2	40	616.4
5000	100/30	2.0	30	590.3

All of the thin film deposition in this work were done by using a custom made vacuum chamber which was integrated in both evaporation and sputtering. Figure 3.3 shows both the external and the internal part of the chamber. The chamber consists of sputter targets, evaporation sources, two quartz microbalances for an *in-situ* film thickness monitoring and a sample holder.

The Chamber is equipped with a rotary pump (Pfeiffer DUO 005 M), to gen-

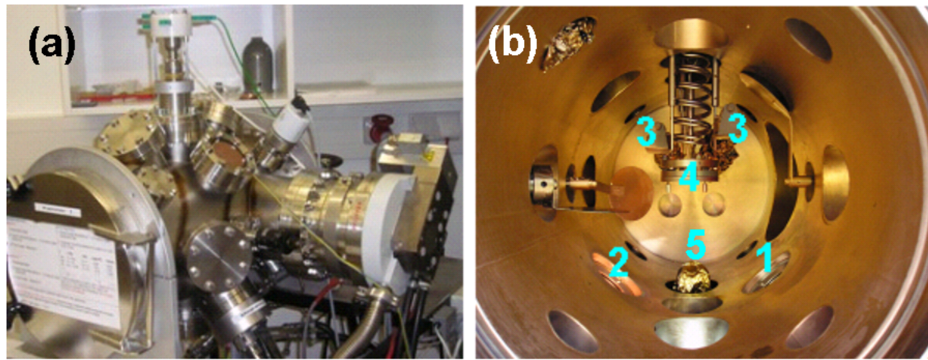

Figure 3.3: *The physical vapor deposition chamber used for thin film preparation: Photo (a) and inner part of the chamber (b). The numbers represent sputtering sources (1 and 2), evaporation source (5), quartz crystal microbalance (3) and a sample holder (4).*

erate the pre-vacuum (10^{-1} torr) together with a turbomolecular pump (Pfeiffer TMU 260) were used for creating the end-vacuum in the range of 10^{-7} - 10^{-8} torr. A relatively good vacuum condition is required to reduce collision of the transported material with the residual gas. Thus, the reduction in the rate of

deposition and oxidation of the materials were prevented.

3.2.1 Thin Film Deposition by Evaporation

This technique was mainly used for the deposition of adhesion promoter such as Chromium (purity = 99.99%, Goodfellow) prior to nanowire material deposition into cracks (see chapter 5) and for the deposition of gold before the synthesis of ZnO nanosails (see chapter 6.1) in which gold was used as a catalyst for the growth of the nanostructures.
The basic process of this technique is based on thermal energy which is supplied to a source from which atoms are evaporated for deposition onto a substrate. The vapor source configuration is intended to concentrate the heat near to the source material and to avoid heating the surroundings. Heating of the source material can be accomplished by any of several methods. The simplest is resistance heating [23, 24] of a wire (tungsten (W), tantalum (Ta)) or stripe of a refractory metal to which the material is attached. Larger volume of the source materials can be heated in crucibles of refractory metals, oxides or carbons by resistance heating, high frequency induction or electron beam heating. The evaporated atoms travel through reduced back ground pressure in the evaporation chamber and condense on the growth surface.
Figure 3.4 shows the home made metal evaporator which is designed to reduce any possible thermal coupling problem. The Tantalum (Ta) heater coil filament was selected to carry the high current and generate the heat required to evaporate the charge. Ta is known for its high melting point, thermal shock resistance, and ductility among the refractory metals. In this design, the Ta heater coil is minimally supported within notched ceramic support rods to reduce heat sinking. The coil extends well below the bottom of the crucible so that the thermocouple touching the crucible bottom is immersed within the same heating environment as the crucible and thus stabilizes at the same temperature. Moreover, the coil is extended towards the crucible mouth, above the level of the charge, which leads the mouth of the crucible to be at higher temperature than the temperature of the charge. This prevents condensation of evaporant droplets at the mouth and also prevents evaporants which wet the crucible from migrating out of it. In addition, the radiation heat shielding consists of several wraps corrugated Ta

foil is used to reflects radiation from the coil and crucible, thereby improving source temperature and reducing out gassing of nearby hardware. A cup shaped crucible sources (length = 17mm, and inner diameter = 3mm) made of aluminum oxide, molybdenum, and boron nitride were used as a source of the evaporant. Crucible materials should be chosen whose residual contaminants are the least harmful to the film being deposited. However, much of the volatile contaminant were removed from the crucibles and associated components by firing it at higher temperature than the desired evaporation temperature prior to the filling with new evaporant.

The quantitative interpretation of evaporation phenomena was first studied by

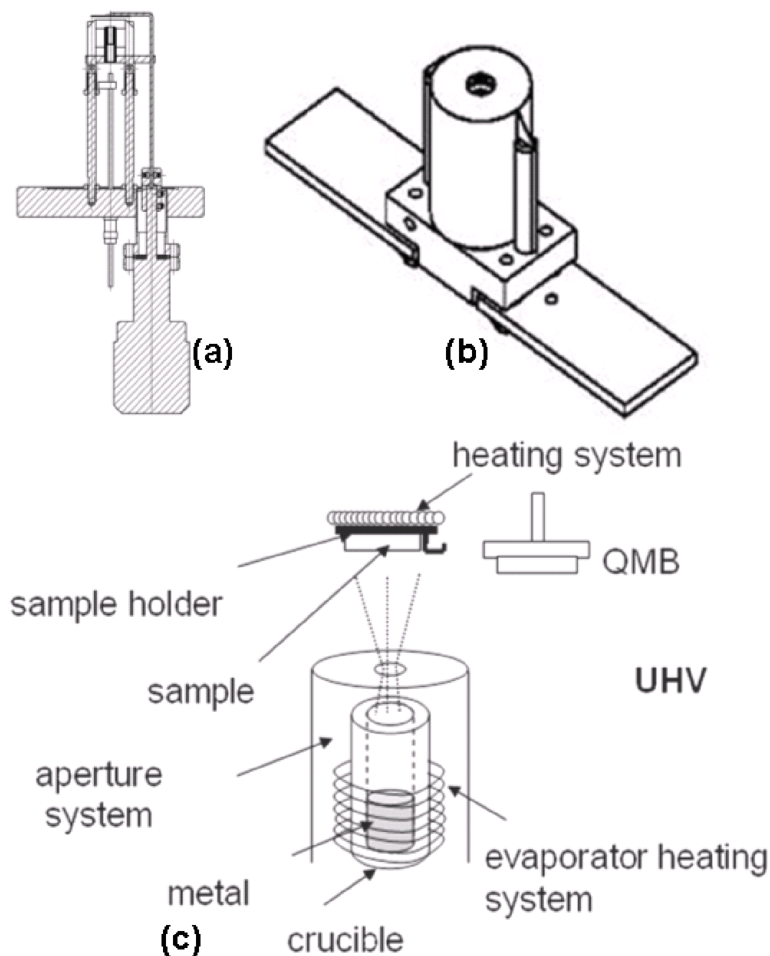

Figure 3.4: *The sketch showing the metal evaporator with a power feed through (a), and both the external (b) and the internal (c) part of the metal evaporator cell.*

Hertz, Knudsen and Langmuir. Based on their investigation (mainly by Hertz), the maximum evaporation rate is attained when the number of vapor molecules emitted corresponds to that required to exert the equilibrium vapor pressure while none return. These idea led to the basic equation for the rate of the evaporation from both liquid and solid surfaces, namely, [25]

$$\phi_e = \frac{\alpha_e N_A \left(P_e - P_h\right)}{\sqrt{2\pi MRT}} \tag{3.2}$$

where ϕ_e is the evaporation flux in number of atoms (or molecules) per unit area per unit time, and α_e is the coefficient of evaporation, which has a value between 0 and 1.

The main characteristic of evaporation is very poor step coverage, including shadow effects, as illustrated in Figure 3.5. Therefore, the deposition of the adhesion promoter on thin film cracks which have high aspect ratio was done under rotation to minimize the shadowing effect.

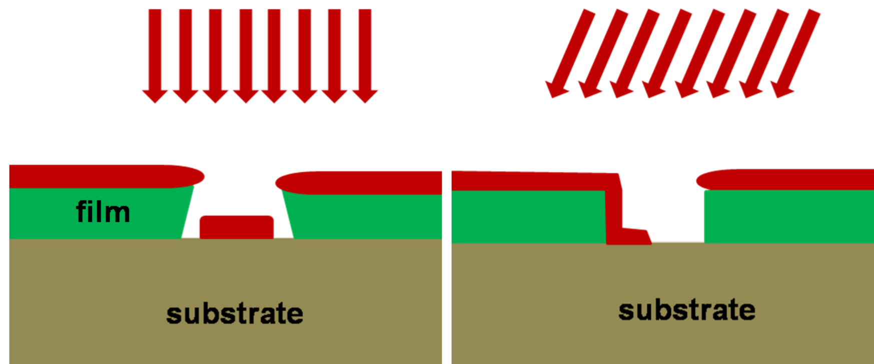

Figure 3.5: *Shadow effects observed in evaporated films. Arrows show the trajectory of the material atoms being deposited.*

3.2.2 Thin Film Deposition by Sputtering

Sputtering process can be divided into four categories: dc, RF, magnetron, and reactive. This sputter-erosion of solid materials by positive-ion bombardment is widely used as a source of vapor for thin film deposition because of the following unique combination of advantages over other techniques: any material can be

volatilized by sputtering, compounds are volatilized stoichiometrically, and the film deposition rate can be uniform over very large area. Here, the deposition of metals (such as gold, platinum, palladium etc. with 99.99% purity) was mainly done by magnetron sputtering and will only be discussed.
Magnetron sputtering is presently the most widely commercially practiced sputtering method due to its high deposition rates. These are typically order of magnitude higher rates than attained by conventional sputtering techniques. It incorporates a crosswise magnetic field over the cathode which prolongs the electrons residence time in the plasma and thus enhances the probability of ion collision. The electron within the dual field (i.e. both magnetic- and electric fields) experience the well known Lorenz force in addition to an electric field force:

$$\mathbf{F} = \frac{mdv}{dt} = -q\left(\mathbf{E} + \mathbf{v} \times \mathbf{B}\right) \tag{3.3}$$

where q, m and v are the electron charge, mass and velocity, respectively. This leads to the larger discharge current and increased sputter deposition rate, in other words this magnetic field greatly increases their mean free path length before they finally escape to the anode by scattering. Because the travel path of electrons is now much longer than the electrode gap, the minimum pressure to sustain the plasma is much lower for the magnetron than for the planar diode. The sputtered atoms retain most of their kinetic energy on reaching the substrate. Besides, the deposition rate is increased because of reduced scattering and redeposition of sputtered atoms on the cathode. Figure 3.6 presents the cathode shape and configuration of magnetic field in a typical sputtering system [26].

3.2.3 *In-Situ* Film Thickness Monitoring

The thickness of the film during evaporation and sputtering was controlled by a conventional STM-100/MF quartz crystal microbalance (QCM) monitoring system which is one of the most widely diagnostic instruments in thin film technology. The QCM consists of a thin quartz crystal sandwiched between two metal electrodes as shown in Figure 3.7. Thus, an alternating electric field is applied across the crystal, causing vibrational motion of the crystal at its resonant frequency.

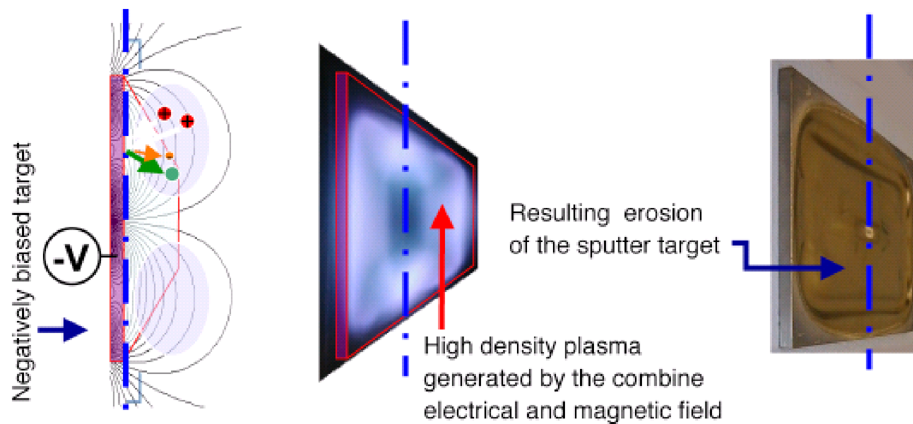

Figure 3.6: *Sketch showing the principle of magnetron sputtering.*

The basic working principle of the QCM is the converse piezoelectric effect in

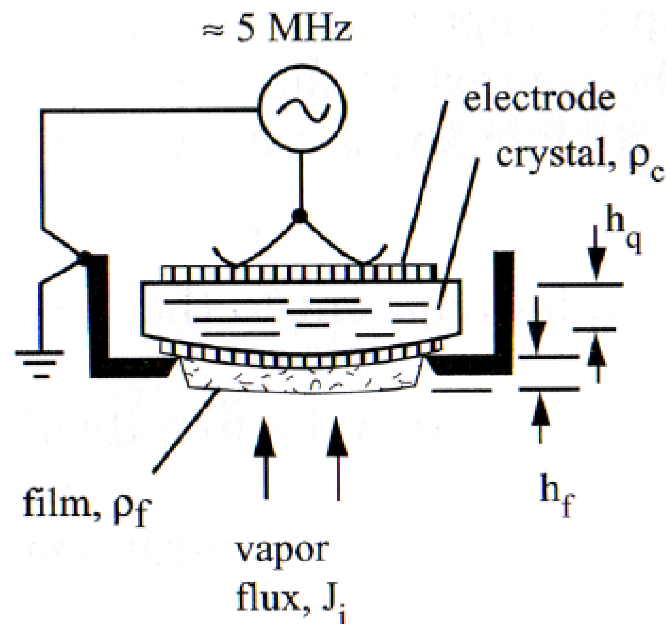

Figure 3.7: *Quartz-crystal deposition monitor in crossection.*

which the application of a voltage across the crystal results in a corresponding mechanical strain. The crystal symmetry dictates that the strain induced in a piezoelectric material by an applied potential of one polarity will be equal and opposite in the direction to that resulting from the opposite polarity. Applica-

tion of an electric field across the crystal produces a shear strain proportional to applied potential . Therefore, an alternating potential across the crystal causes vibrational motion in the quartz crystal with amplitude parallel to the surface of the crystal.
The extremely sensitive nature of the piezoelectric devices toward mass changes was first demonstrate by Sauerbey [27]. According to Sauerbeyѓs equation, the mass changes Δm at the surface of the QCM electrode surface causes a change in the oscillation frequency Δf of the crystal:

$$\Delta f = -C_f \Delta m \tag{3.4}$$

where C_f the sensitivity factor of the crystal used. Equation 3.4 relies on a linear sensitivity factor which is the fundamental property of the QCM crystal. In this case, the incremental change in mass due to the additional deposition is treated as though it was really increasing the thickness of the underlying quartz. The deposited film is considered to be rigid and so thin that it does not experience any shear forces during vibration.
The thickness of the film can be calculated by:

$$d_f = \frac{\Delta m}{\rho_f} \tag{3.5}$$

where d_f and ρ_f are the thickness and the bulk density of the deposited film, respectively. respectively. However, vacuum and gas phase thin film depositions exhibit more complicated frequency-mass correlations as shown in equation:

$$d_f = \frac{N_q \rho_q}{\pi \rho_f Z f_1} tan^{-1} \left[Ztan \left(\frac{\pi \left(f_u f_1 \right)}{f_u} \right) \right] \tag{3.6}$$

where N_q is the frequency constant of a quartz crystal, ρ_q is the density of the quartz (2.684 g/cm^3), f_1 and f_u are frequencies of loaded and unloaded crystals, respectively, and Z is the Z-factor of the film material.

3.2.4 Atomistic Film Growth

Growth of thin films, as all phase transformation, involves the processes of nucleation and growth on the substrate or growth surfaces. The nucleation process plays a very important role in determining the crystallinity and microstructure of the resultant films. For the deposition of thin films with thickness in the nanometer region, the initial nucleation process is even more important. The size and the shape of the initial nuclei are assumed to be solely dependent on the change of volume of Gibbs free energy, due to supersaturation, and the combined effect of surface and interface energies governed by Young's equation. No other interactions between the film or nuclei and the substrate were taken into consideration. In practice, the interaction between film and substrate plays a very important role in determining the initial nucleation and the film growth. The many observation of film formation have pointed three basic growth modes: island (Volmer-Weber), layer (Frank-van der Merwe), and Stranski-Krastanov. Figure 3.8 illustrates these three basic modes of initial nucleation in the film growth. Island growth occurs when the growth species are more strongly bonded to each other than to the substrate. Many systems of metals on insulator substrates, alkali halides, graphite and mica substrates display this type of nucleation during the initial film deposition. Subsequent growth results in the islands to coalesce to form a continuous film. The layer growth is the opposite of the island growth, where growth species are equally bound more strongly to the substrate than to each other. First complete monolayer is formed, before the deposition of second layer occurs. The most important examples of layer growth mode are the epitaxial growth of single crystal films. The island-layer growth is an intermediate combination of layer growth and island growth. Such a growth mode typically involves the stress, which is developed during the formation of the nuclei or films.

The free energy change accompanying the formation of an aggregate of mean dimension r is given by

$$\Delta G = a_3 r^3 \Delta G_V + a_1 r^2 \gamma_{vf} + a_2 r^2 \gamma_{fs} - a_2 r^2 \gamma_{sv} \tag{3.7}$$

The chemical free-energy change per unit volume, ΔG_v, drives the condensation reaction. There are several interfacial tensions, γ and these are identified by the subscript f, s, and v representing film, substrate and vapor, respectively. The

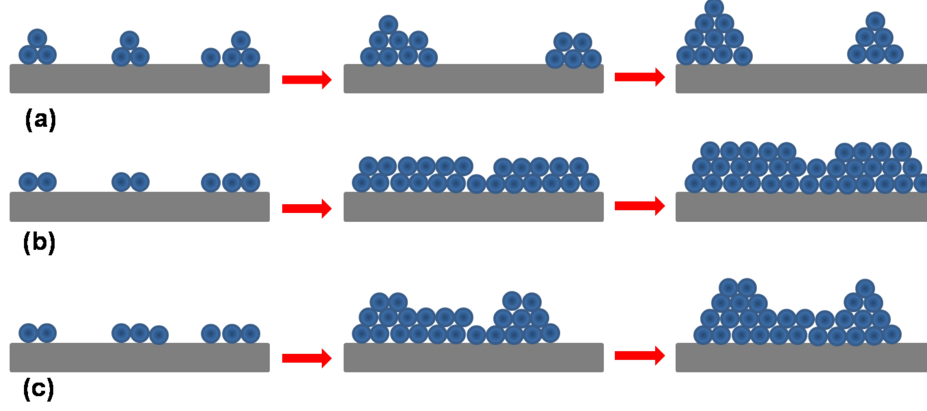

Figure 3.8: *Schematic illustrating three basic modes of initial nucleation in film growth: Island (Volmer-Weber) growth (a), layer (Frank-van der Merwe) growth (b) and Island-layer (Stranski-Krastonov)growth (c) .*

formation of new phases results a reduction of Gibbs free energy, but an increase in the total surface energy. The nucleation is stable only when its size is larger than the critical size, r^*:

$$r^* = \frac{-2\left(a_1\gamma_{vf} + a_2\gamma_{fs} - a_2\gamma_{sv}\right)}{3a_3\Delta G_v} \tag{3.8}$$

Correspondingly, ΔG_v evaluated at $r = r^*$ is

$$\Delta G^* = \frac{4\left(a_1\gamma_{vf} + a_2\gamma_{fs} - a_2\gamma_{sv}\right)^3}{27a_3^2\Delta G_v^2} \tag{3.9}$$

For island growth, the contact angle must be larger than zero. Therefore according to Young's equation the relation among the interface energies will be as described in equation 3.10

$$\gamma_{sv} < \gamma_{fs} + \gamma_{vf} \tag{3.10}$$

If the deposit does not wet the substrate at all, the nucleation is a homogeneous nucleation. For layer growth, the deposit wets the substrate completely and the contact angle equals zero; the corresponding Young's equation becomes:

$$\gamma_{sv} = \gamma_{fs} + \gamma_{vf} \tag{3.11}$$

Island-layer growth is a little more complicated and involves *in situ* developed stress. Initially the deposition would proceed following the mode of layer growth. When the deposit is elastically strained due to, for example, lattice mismatch between the deposit and the substrate, strain energy would be developed. As each layer of deposit is added, more stress is developed and so is the strain energy. Such strain energy is proportional to the volume of the deposit, assuming there is no plastic relaxation. When the stress exceeds a critical point and cannot be released, the strain energy per unit area of deposit is large with respect to γ_{vf}, permitting nuclei to form above the initial layered deposit. In this case, the surface energy of the substrate exceeds the combination of both surface energy of the deposit and the interfacial energy between the substrate and the deposit:

$$\gamma_{sv} > \gamma_{fs} + \gamma_{vf} \tag{3.12}$$

4 Characterization Techniques

This chapter presents the basics of the characterization techniques used for the analysis of structural, chemical as well as physical properties of the synthesized horizontal- and vertical nanowires (nanosails and nanoseaurchins). These characterization techniques include light optical microscopy, atomic force microscopy (AFM), scanning electron microscopy (SEM), transmission electron microscopy (TEM), high resolution transmission electron microscopy (HRTEM) and *x*-ray photoelectron spectroscopy (XPS). Moreover, the custom made device used for electrical characterization of the synthesized nanostructures will also be discussed briefly.

4.1 Light Microscopy

A light microscope has been used for about 300 years. It is a deceptively simple instrument, being essentially an extension of human eyes which magnifies images of small objects, enabling to directly view structures that are below its resolving power (0.1 mm). Further more, it offers a first look at most samples and could be used to routinely document the progress of an investigation.
The direct visual advantage of a light microscope enabled quick investigation of the features of thin film cracks and a deposited metal film for fractured based nanowire and ZnO nanosail synthesis, respectively. The characterization of crack's morphology, particularly, was often done at different magnification ranging from 25 $\times$ to 1000 $\times$ right after crack formations. This helps to check the features of the cracks prior to material (such as gold, silver etc.) filling. Figure 4.1 shows the schematic representation of the possible reflection of the light on a delaminated area near/around the cracks as observed by the microscope. The incoming light will be reflected on the surface of the delaminated thin film,

thus the surrounding cracks appear darker as shown in many of optical images in chapter 5. The resolving power of a microscope is taken as the ability of the mi-

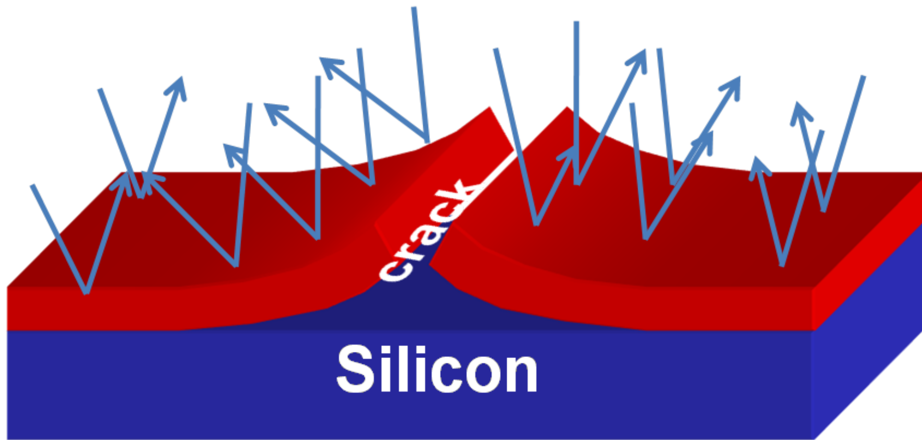

Figure 4.1: *Schematic illustration of reflection of light from the delaminated thin film. As the result the crack appears darker when it is observed by optical microscope.*

croscope to reveal adjacent structural detail as distinct and separate. It is these impacts of diffraction that limit the ability to resolve fine details. The extent of and magnitude of the diffraction patterns are affected by both the wavelength of light (λ), the refractive materials used to manufacture the objective lens and the numerical aperture (NA) of the objective lens. There is therefore a finite limit beyond which it is impossible to resolve separate points in the objective field, known as the diffraction limit. Assuming that optical aberrations in the whole optical set-up are negligible, the resolution d, is given by:

$$d = \frac{\lambda}{2NA} \tag{4.1}$$

4.2 Atomic force microscopy

Atomic force microscopy (AFM) was introduced about 20 years ago [28]. Since this time these technique has been revolutionized surface analysis by providing high-resolution visualization of structures at the atomic- and nanometer-scales. The remarkable feature of AFM instruments is its ability to examine samples at

ambient conditions and even in liquids. Moreover, it can be applied for characterization of materials of any kind. This functionality is inherent to AFM, which is based on detection of more universal tip-sample mechanical forces. The scope of AFM applications includes high-resolution examination of surface topography, compositional mapping of heterogeneous samples and studies of local mechanical, electric, magnetic and thermal properties. These measurements can be performed on scales from hundreds of microns down to nanometers, and the importance of AFM, as characterization technique, is further increasing with recent developments in nanoscience and nanotechnology.
AFM employs a sharp tip (typically made from Si_3N_4 or Si) to probe the surface under investigation. The tip is placed at the end of a long cantilever with a low spring constant ($\sim 1\ Nm^{-2}$) and brought into physical contact with the surface as shown in Figure 4.2 (a). The force on the tip is determined by a laser probe. AFM head employs an optical detection system in which the tip is attached to the underside of a reflective cantilever. Typically, a diode laser is focused onto the back of a reflective cantilever. As the tip scans the surface of the sample, moving up and down with the contour of the surface, the laser beam is deflected off the attached cantilever into a dual element photodiode. The resolution limit of AFM is highly influenced by the size of the tip. The sharper the tip, the better the resolution as shown in Figure 4.2 (b).

When the probe-surface spacing is relatively large ($\approx$ 1 nm or greater), the interactions are dominated by long-range van der Waals forces (Figure 4.2 (c)). These attractive forces depend exponentially on distance and are extremely sensitive to probe-tip shape. Other attractive forces include metallic adhesion forces and charge accumulation between the probe tip and the nearest surface atom. At small spatial separations ($\approx$ 0.1 nm or less), the wave function of the probe-surface overlap and short-range quantum-mechanical exchange-correlation forces dominate due to the Pauli exclusion principle. These forces decay exponentially with increasing distance:

$$F = -\gamma \Delta E_C \chi \left[\sigma \frac{H}{e^2}\right]^{\frac{1}{2}} \tag{4.2}$$

where ΔE_C is the width of the conduction band, γ is a dimensionless factor approximately equal to one, χ is the decay rate of the force, and σ is the conduc-

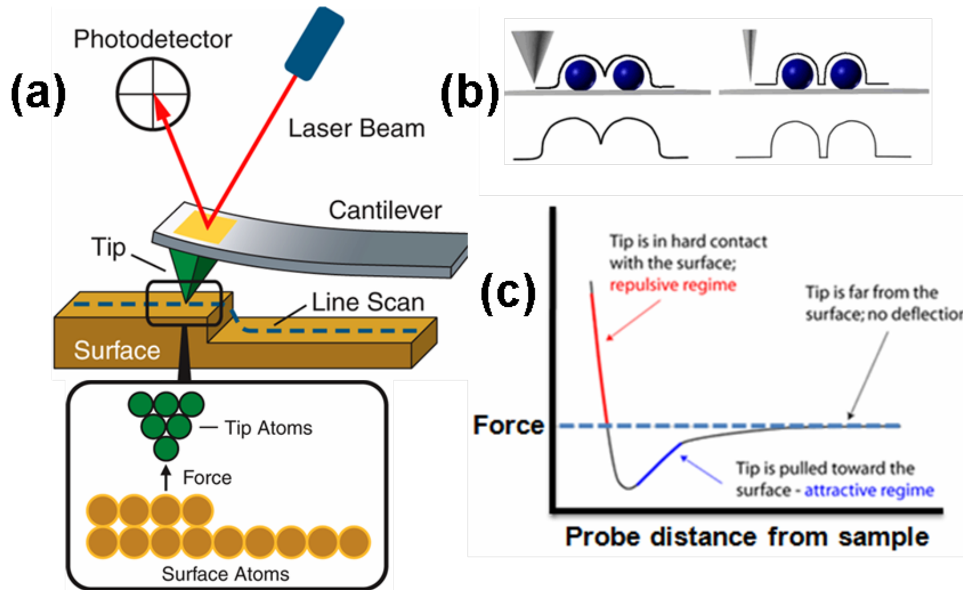

Figure 4.2: *Schematic representation of an atomic force microscope (a). The inset shows the close view of the tip-surface interaction. The tip-effect (b) and the force-displacement curve (c) are also shown.*

tance [29].

4.2.1 Probe-Sample Interaction

The way in which image contrast is obtained can be achieved in many ways. The three main classes of interaction are contact mode, tapping mode, and noncontact mode. Here, the contact mode was used for topography analysis of different nanowires. Hence, the contact and noncontact modes are selectively discussed.

4.2.1.1 Contact Mode

Contact mode is the most common method of operation of the AFM. As the name suggests, the tip and sample remain in close contact as the scanning proceeds and it is in the repulsive regime of the inter-molecular force curve (see Figure 4.2). In this mode, the tip never leaves the surface (as shown in Figure 4.3 (a)), so this mode can be used for very high resolution imaging. The maximum vertical force

is also controlled, so the compression of the sample can be limited. The lateral forces, as the tip moves over the surface, can be a problem in some situations, but can actually be an advantage in other situations. The lateral deflection can give information about the friction between the tip and the sample, and can show areas that may have the same height, but different chemical properties. In contact mode, the set point value is the deflection of the cantilever, so a lower value of the set point gives a lower imaging force.

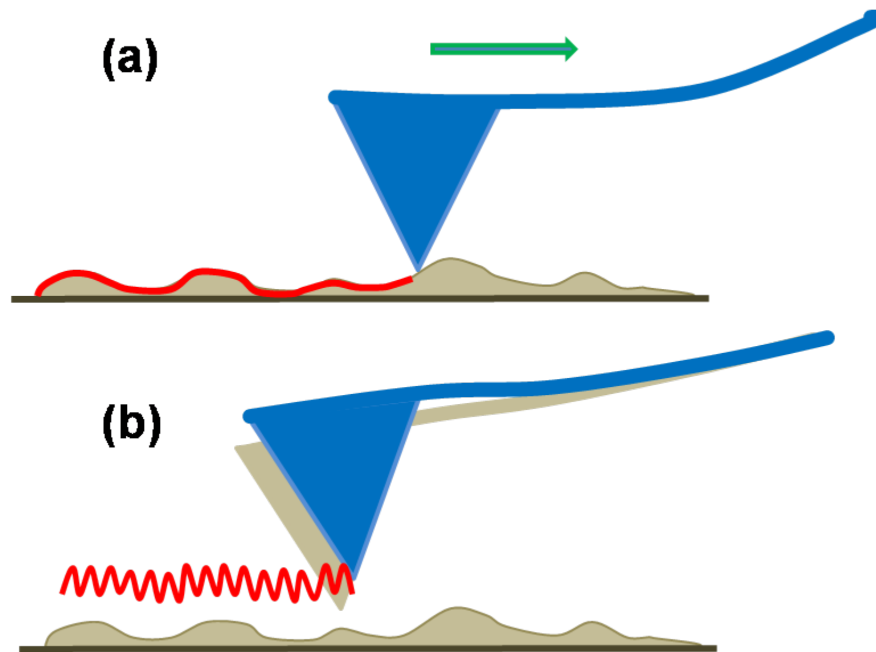

Figure 4.3: *Sketch depicting contact mode (a) and noncontact mode (b) of AFM.*

4.2.1.2 Noncontact Mode

Non-contact operation is another method which may be employed when imaging by AFM. The cantilever must be oscillated above the surface of the sample at such a distance that it is no longer in the repulsive regime of the inter-molecular force curve. This is a very difficult mode to operate in ambient conditions with the AFM. The thin layer of water contamination which exists on the surface on the sample will invariably form a small capillary bridge between the tip and the

sample and cause the tip to "jump-to-contact". Even under liquids and in vacuum, jump-to-contact is extremely likely, and imaging is most probably occurring using unintentionally tapping mode, in which the periodic contact to the sample surface occurs.
The AFM (Park scientific instrument, Auto probe CP) was used for the topographical investigation of the synthesized nanowires (see chapter 5. Figure 4.4 shows the observed grainy nature of the as-synthesized nanowires. However, due to tip effect the resolution of individual grains was not possible.

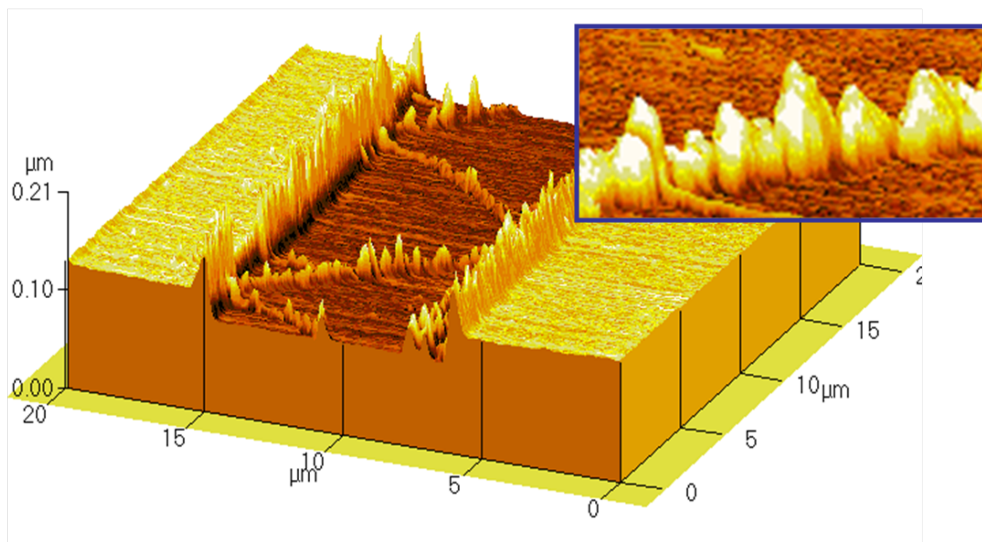

Figure 4.4: *The AFM image of the nanowires synthesized by using thin film fracture approach (see chapter 5). The inset shows the roughness of the nanowires.*

4.3 Scanning Electron Microscopy

The scanning electron microscope (SEM) is one of the most widely used instruments in materials research laboratories. It is central to microstructural analysis and therefore important to any investigation relating to the processing, properties, and behavior of materials that involves their microstructure. The SEM is used for imaging the surface of the materials (e.g., topographical features) with the aid of signals derived from the interaction between the probe electrons and

the specimen. The strength of the SEM lies in its inherent versatility due to the multiple signals generated, simple image formation process, wide magnification range, and excellent depth of field.
Here, the SEM (Philips X L 30) was used for thorough topological investigations of various nanostructures including nanowires, nanoseaurchins and nanosails. The feature of the thin film cracks was also studied prior to the nanowire formations (see images in section 5). The topography analysis of the cracks on the resist was done after depositing a conductive layer (e.g. gold, platinum etc.) Moreover, the elemental composition analysis (discussed in section 4.4) of the nanostructures was also done.

4.3.1 Principle of Operation

Figure 4.5 shows a schematic diagram of an electron optical column for a two lens of SEM. A source of electron is focused (in vacuum) into a fine probe that is scanned over the surface of the specimen. As the electrons penetrate the surface, a number of interactions occur that can result in the emission of electrons or photons from (or through the surface). The electron gun operates typically over a range 0-30 keV sometimes extending up to 60 keV depending upon the type of instrument and application where the specimen is maintained at earth potential. The microscope is a probe forming system where each lens condenses and demagnifies the electron source to a focus spot at the specimen surface. Figure 4.5 (b) shows the corresponding ray diagram for a complete microscope. Apertures that are included at various positions to limit divergence of the electron beam. To achieve the smallest diameter electron probes incident on the specimen the final condenser lens must have low aberrations; however, the resolution of the final image cannot be less than the diameter of the scanning electron beam. Small electron beam is, therefore, high resolutions are obtained if the lens apertures is adjusted to an optimum size $\approx$ 150 μm diameter. A large depth of focus is achieved for these instruments because the electron beam is focused from the aperture on to the specimen surface over a distance of typically $\approx$ 15 mm, if the beam divergence is low ($\alpha = 3.3x10^{-3}$ rad) this gives the depth focus of several millimeters. It is the combination of the high resolution with the large depth of focus which makes SEM well suited to examine topography of the materials such

as fracture surface.

Three types of electron guns are in common use today: tungsten (W) and

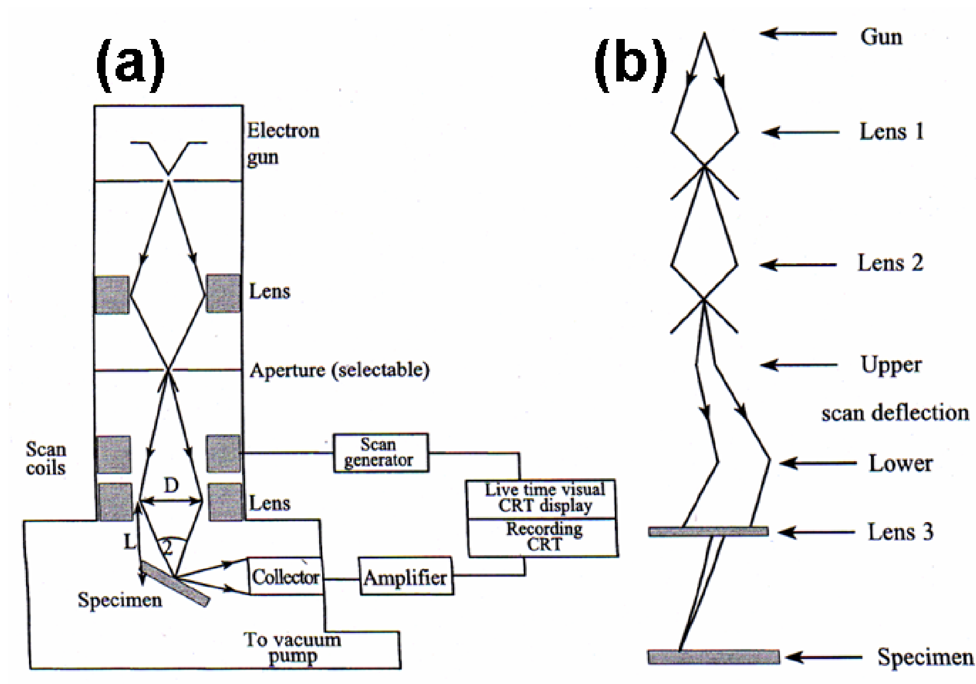

Figure 4.5: *Schematic diagram of a scanning electron microscope (a), and ray paths in SEM; standard arrangement for image formation (b).*

lanthanum hexaboride (LaB_6) thermionic electron guns, and the field emission gun. Tungsten and lanthanum hexaboride are used as filaments in thermionic electron guns, in which the filament (cathode) is heated by applying a current. Emission of electrons occurs at high temperatures and requires that the gun be operated in a high vacuum to avoid oxidation. The emitted electrons are accelerated to high energy by the application of a negative voltage to the cathode and a bias voltage to the grid cap with the anode grounded. This triode system accelerates the electrons and provides an initial focusing into a probe. Tungsten is popular for its low cost, ease of replacement, and high current yield, while LaB_6 (used here) provides a brighter source (higher current density) useful for higher resolution. In the field emission gun, a fine tip is placed near a grid and electrons escape the surface due to the high extracting field strength created by the first grid. A second grid provides the accelerating voltage. Field emission requires ultrahigh vacuum and is more expensive, but it provides much higher

brightness with a resultant increase in resolution.

4.3.2 Electron-Sample Interactions

When an electron emitted from the source and hit the solid surface, it penetrates into the microstructure of the solid and interact with its atoms. During this process, two different interaction phenomena can occur: elastic and inelastic scatering. The electrons do not lose significant energy during elastic scattering instead they get deflected at the nucleus; it merely changes its direction. Where as, the collision between electrons with electrons of the atomic shell is accompanied by an energy transfer due to an equal masses of the colliding particles (inelastic scattering). As the result, the incident electron does not only change its direction, but it also slows down. These two processes operates side by side and simultaneously. As a consequence of these different scattering events, an electron probe which originally was sharply focused in vacuum spreads over a greater volume after penetrating the solid (see Figure 4.6). The shape and the size of this scattering volume depends upon the material as well as on the energy and angle of incidence of the probe electrons. The most accurate theoretical values for extension and shape of the scattering volume are obtained with the aid of Monte Carlo calculations [30, 31].

The principal images produced in the SEM are of three types: secondary electrons (SE) images, backscattered electrons (BSE) images and elemental x ray maps. The elemental x ray maps is discussed in the coming section. Secondary and backscattered electrons are conventional separated according to their energies. The primary beam current i_0, the BSE current i_{BSE}, the SE current i_{SE}, and the sample current transmitted through the specimen to the ground i_{SC} is defined as (according to Kirchoff current law) [32]:

$$i_0 = i_{BSE} + i_{SE} + i_{SC} \tag{4.3}$$

These signal can be used to form complementary images. As the beam current is increased, each of these current will also increase. The corresponding yields of the BSE η and SE δ, which refer to the number of BSE and SE emitted per

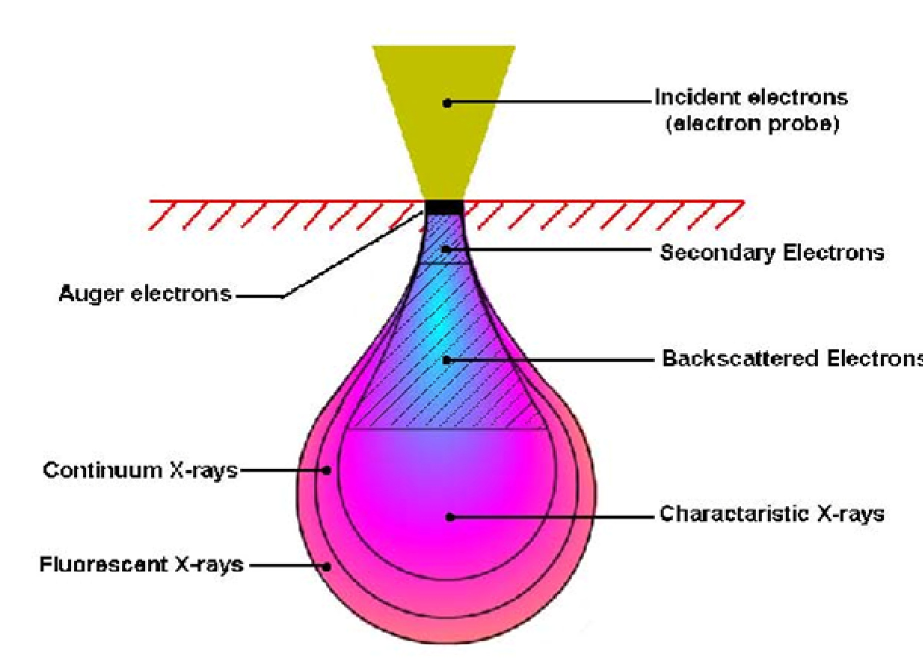

Figure 4.6: *Schematic diagram illustrating the volume of material that is probed by an incident electron beam together with the volumes from which x-rays and backscattered, Auger and secondary electrons emanates.*

incident electron, respectively, are defined by:

$$\eta = \frac{i_{BSE}}{i_0} \tag{4.4}$$

$$\delta = \frac{i_{SE}}{i_0} \tag{4.5}$$

Both SE and BSE yields increase with decreasing glancing angle of incidence because more scattering occurs closer to the surface. This is one of the major reason why SEM provides excellent topography contrast in SE mode; as the surface changes its slope, the number of SE produced changes as well.

4.4 Energy Dispersive X-Ray Analysis

An Energy Dispersive X-ray Spectrometer (EDX) mounted in a scanning electron microscope (SEM) (Philips X L30) was used to identify and determine the local content of zinc oxide (ZnO) nanosails as shown in Figure 4.7.

The transfer of energy from the primary electrons to the solid, *i.e.*, the inelastic

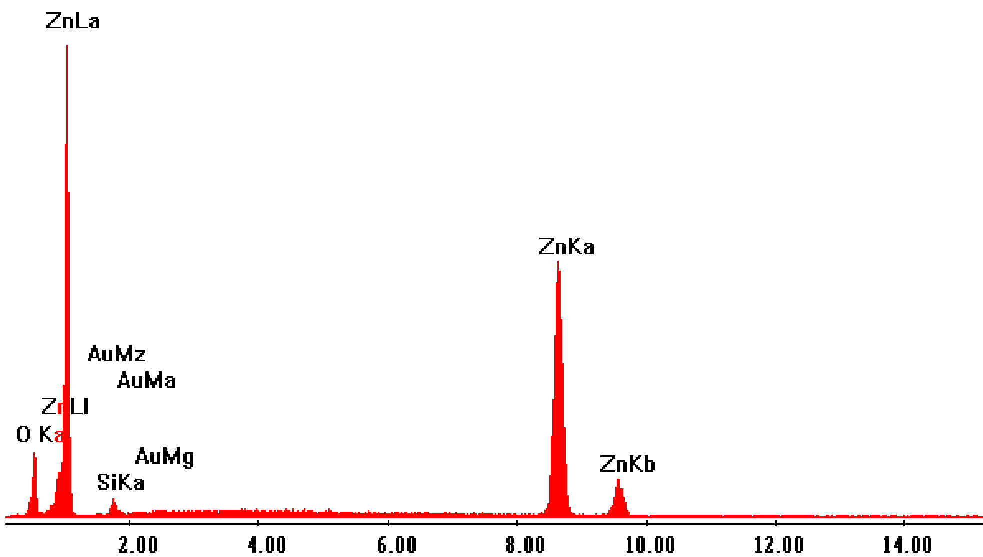

Figure 4.7: *EDX spectra of the as-synthesized ZnO nansails which confirms the presence of Zinc as well as oxygen.*

interaction, leads to various secondary process such as secondary electron (SE) emission, x-ray emission, Auger electron (AE) emission etc., as shown in Figure 4.8. A primary electron incident with sufficiently high energy initially detaches an electron from an inner shell, for instance the K shell, and removes it from the atom. As a result, the atom attains a higher energy state. When the atom returns to its ground state, an electron from an outer shell (e.g. L shell) fills the vacancy in the K shell. The energy released in this process leads to the either photon (x-ray) or another electron (Auger electron, e.g. from the L shell). The vacancy now left in the L shell is filled by a further transition of an electron from an outer shell, with the associated emission of the another x-ray or AE. This process will be repeated in a similar sequence until the atom finally has returned to its neutral ground state.

The basis of practical quantitative electron probe microanalysis is Castaing's

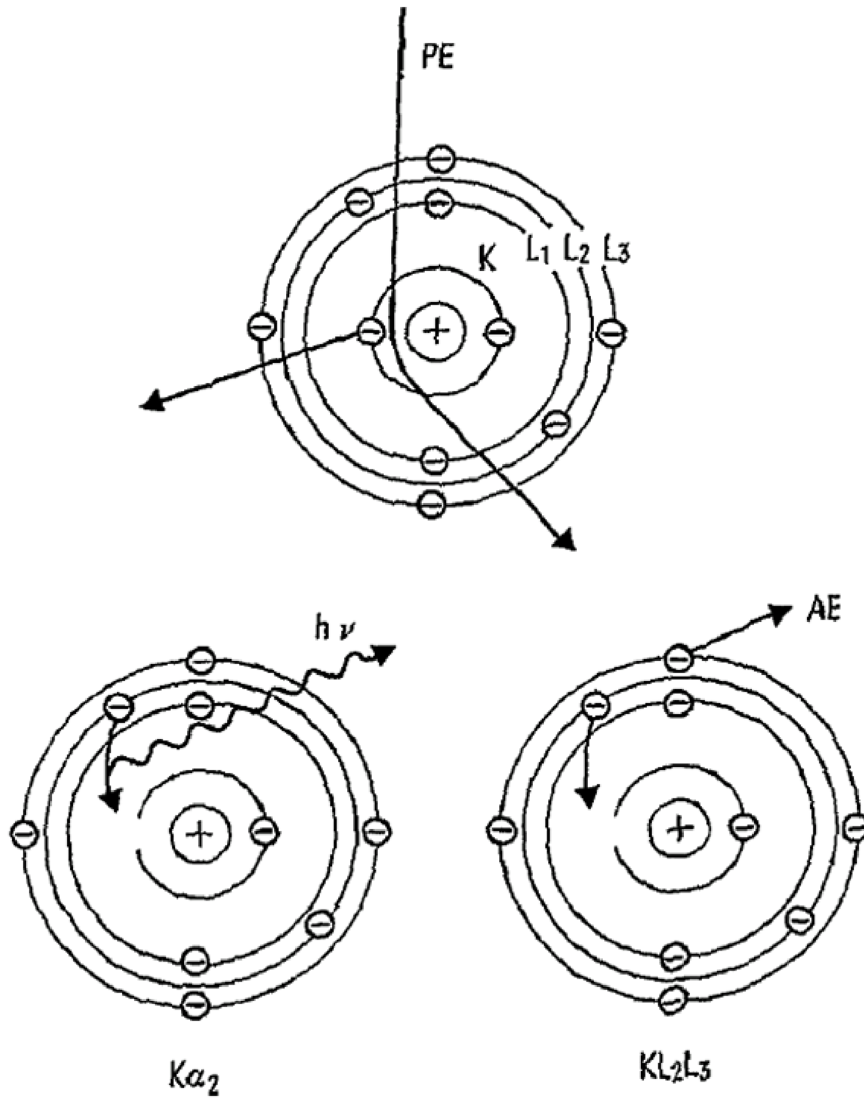

Figure 4.8: *Sketch showing how the x-ray and auger electrons are emitted as the result of the energy release by the electron from the highre states returns to its ground state [33].*

first approximation, which relates the concentration with for a constituent in the unknown to the concentration in a standard in terms of the ratio of x-ray intensities generated in the target:

$$\frac{C_i}{C_{i^*}} \approx \frac{I_i^G}{I_{i^*}^G} \tag{4.6}$$

where C is the mass concentration, I^G is generated characteristic peak intensity , i denotes a specific constituent, and $*$ demotes the standard, such as pure element. The actual measured value is the ratio of emitted intensities $I_i^E/I_{i^*}^E$, so called k value. The emitted x-ray intensity ratio deviates from the generated intensity ratio in equation 4.6 because of interelement or matrix effect.
Quantitative analysis procedure so called ZAF method which is based upon a combination of theory and empiricism have been used to calculate separate correction factors for each of the matrix effects. Using the matrix effect the most common form of the correction equation is

$$\frac{C_i}{C_{i^*}} = ZAF\left[\frac{I_i^G}{I_{i^*}^G}\right] \tag{4.7}$$

The term ZAF in equation 4.7 refers to the correction due to effect of atomic number (Z), X-ray absorption effect (A) and X-ray fluorescence. Since the composition of the unknown appears in each of the correction factors, its necessary to an initial estimate of the composition. The advantage of this procedure is first, there is no need to know the spectrometer's efficiency. Second, an exact knowledge of the inner shell ionization cross section or fluorescence yields is not needed, since they also cancel in the ratio.

4.5 Transmission Electron Microscopy

A transmission electron microscope (TEM) is one of the most powerful instruments for investigating the microstructure of materials. This instrument enables the fine-scale microstructure to the nanoscale to be examined in specimens sufficiently thin (less than 200 nm) to facilitate transmission of a beam of electrons without a great loss of intensity. It has high lateral spatial resolution (better than 0.2 nm) and is capable to provide both image and diffraction information from a single sample.
Figure 4.9 illustrates the lay out of a TEM in the form of a ray diagram. The electrons emitted from the electron gun are accelerated to an energy of between 100 keV- 3 MeV. The condenser lens then shapes them at an approximately parallel beam which illuminates the specimen uniformly. The objective lens produces the first image, which is then magnified by the intermediate and projector lens

and finally projected onto the fluorescent screen (see Figure 4.9 (a)). TEM offers

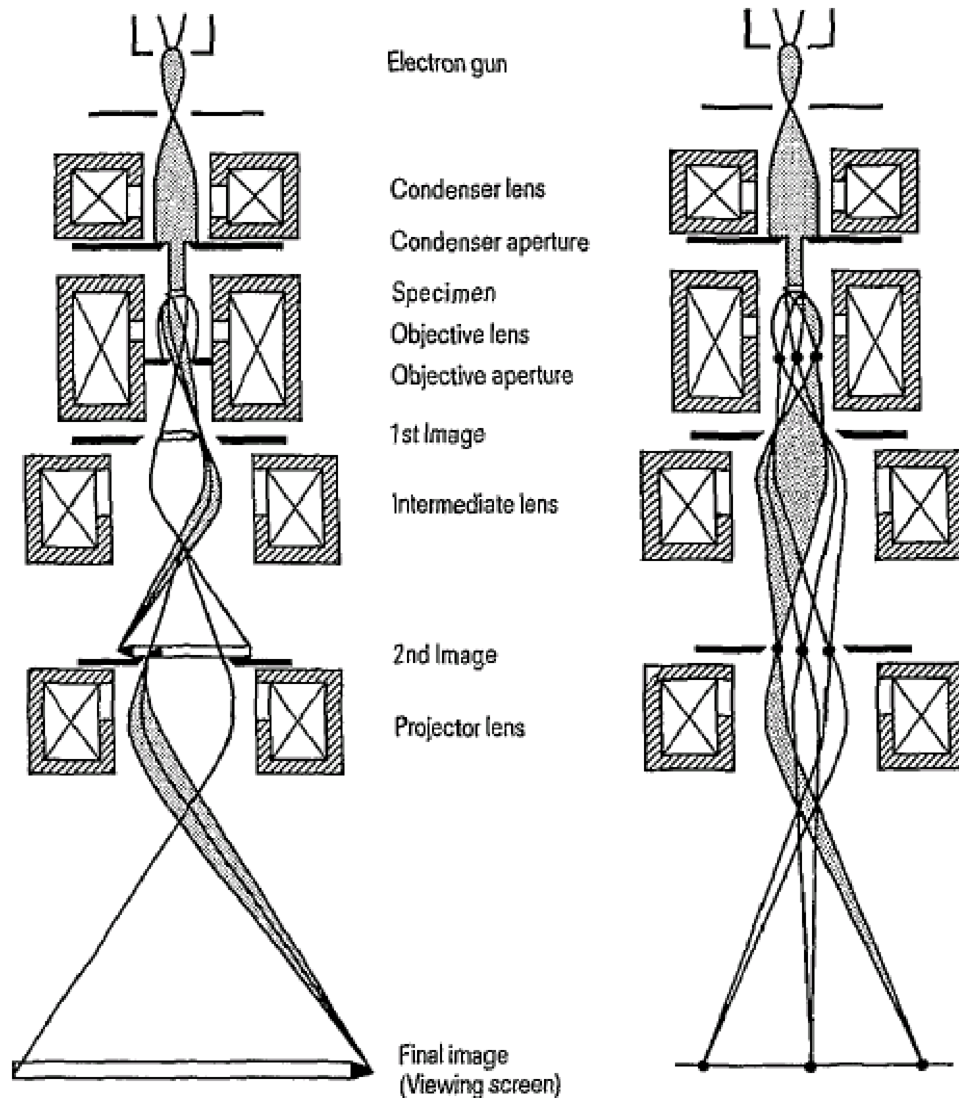

Figure 4.9: *Schematic layout and ray diagrams of a transmission electron microscope. Ray diagram for bright field imaging: the aperture angle of the bundle of rays leaving each object point is limited to approx.* 1 *mrad by the objective aperture (a), and ray diagram for selected area of diffraction (SAD).*

mainly two methods of specimen observation; diffraction mode and image mode. In the diffraction mode, an electron diffraction pattern is obtained on the fluorescent screen, originating from the the sample area illuminated by the electron beam. Whereas the image mode produces an image of the illuminated sample

area. The image can contain contrast brought about by several mechanisms: mass contrast, due to spatial separations between distinct atomic constituents; thickness contrast, due to non uniformity in sample thickness; diffraction contrast, which in the case of crystalline materials results from scattering of the incident electron wave by structure defects etc..
Different parts of unscattered and/or scattered electrons contribute to the formation of an image. Figure 4.10 (a) shows the ray layout of the bright field (BF) imaging ray. The electrons scattered by or diffracted at the specimen by angle larger than Θ_0 are intercepted by the objective aperture and cannot contribute to the image. In dark field (DF) images (shown in Figure 4.10 (b)), the image is generated not by the direct beam but by the intensity of diffracted or scattered electrons and achieved by displacing the objective aperture *i.e.* the TEM is switched to SAD mode. The degrading of spherical aberration as a result of displacing the aperture can be avoided by tilting the incident film so that the diffracted electrons pass through the centered aperture as shown in Figure 4.10 (c). To obtain image contrast in a very thin and weakly scattering specimen , both the electron in the direct beam and scattered electrons must be included in image production as shown in Figure 4.10 (d). A phase contrast is then created by allowing the scattered or diffracted electron to interfere with the direct beam.

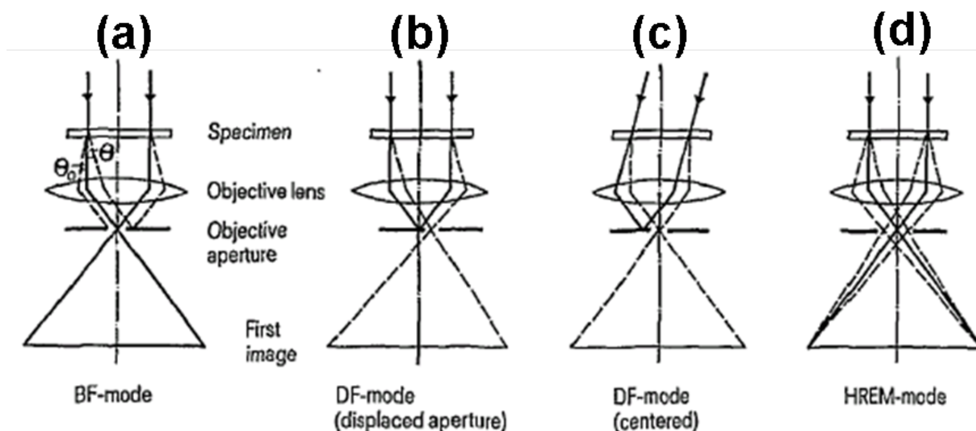

Figure 4.10: *Imaging mode: bright field (BF) mode (a), dark field (DF) mode (displaced aperture), dark field mode (centered) and high resolution mode.*

The microstructural analysis of various synthesized nanostructures such ZnO nanoseaurchins and nanosails were investigated by using high resolution TEM Philips CM 30ST microscope (LaB_6 cathode, 300 kV, C_S = 1.15 mm). SAED (selected area electron diffraction) and PED (precession electron diffraction) were also done using a diaphragm which limited the diffraction to a circular area of 2500 in diameter.

4.6 X-ray Photoelectron Spectroscopy

X-ray photoelectron Spectroscopy is a surface sensitive spectroscopy technique that allows chemical identification of the elements in the top atomic layers of a sample by recording the binding energies of the electrons associated with these atoms. Furthermore, because the binding energies differ not only from chemical species to species, but also vary with the bonding conditions in which the element is found, this technique also provides information on the actual compounds present on the surface. In essence, it probes the electronic structure of the surface. When used in combination with sputter depth profiling, in which ions are used to remove surface layers from a sample, XPS provides information about the depth profile of a sample.
The basic process of photoelectron emission is shown in Figure 4.11. A photon of sufficiently short wavelength (i.e. high energy) can ionize an atom, producing an ejected free electron. The kinetic energy E_k of the electron (the photoelectron) depends on the energy of the photon expressed by Einstein photoelectric law:

$$E_k = hv - E_B \tag{4.8}$$

where E_k is the photoelectron kinetic energy, hv the exciting photon energy and E_B the binging energy of the electron in the solid. Since h is known, measuring of E_k will enable ot determine E_B. The usefulness of determining E_B for material analysis is obvious since E_B for different atoms is distinct. Or the energy levels (or eigenvalues ϵ) of each orbital are different for the same orbital in different atoms, because the electrostatic attraction for different nuclei is different. To a first approximation the binding energy of an electron is equal to the ϵ value. So by experimentally determining an ϵ value, which is specific to the atom concerned,

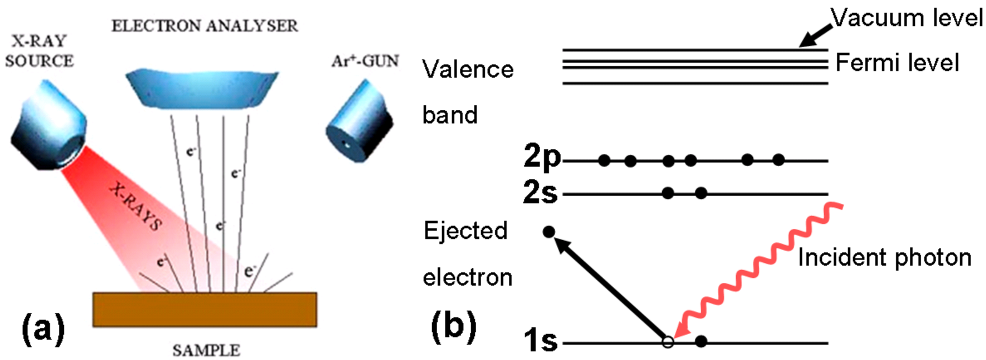

Figure 4.11: *A sketch showing the basic process of photoelectron emissions (a)and (b).*

it is therefore possible to identify the atom. The samples in such experiments are electrically connected to the spectrometer to balance the charge of the emitted electrons and to adjust the two Fermi levels. Therefore the binding energies are usually referenced to Fermi level and the above equation is rewritten as:

$$E_k = hv - E_B^F - \psi \tag{4.9}$$

where ψ is the work function of the spectrometer.
The source X-rays are in short generated by bombarding a water cooled anode with 10-15 keV electrons. Typical anode materials are magnesium or sodium or aluminum, because the energy width of the characteristic x-ray lines are small for light elements.
The XPS technique is highly surface specific due to the short range of the photoelectrons that are excited from the solid. The energy of the photoelectrons leaving the sample are determined and will give a spectrum with a series of photoelectron peaks. The peak areas can be used to determine the composition of the materials surface. The shape of each peak and the binding energy can be slightly altered by the chemical state of the emitting atoms.
In this work, the X-ray spectrometer (VG Sceintific limited, VGS 5000 ESCA) was mainly used for determination of the ZnO formation in the synthesized nanoseaurchins. The intensity vs. binding energy plot obtained clearly shows that the nanoseaurchins are composed of ZnO.

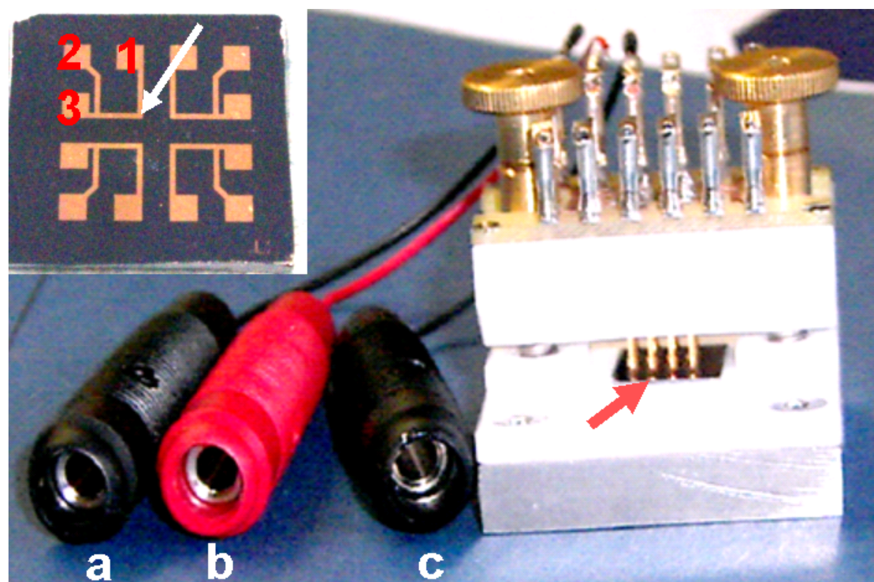

Figure 4.12: *Photo of the microchip holder device which was used to measure the electrical properties of various nanowires. The inset (top-left) shows the microchip consists of horizontal nanowires at each of the contact junctions, and the number refers to the contact points.*

4.7 Electrical Measurement Device

Electrical and electronic measurements of materials are among the most powerful techniques available for materials characterization. These measurements can reveal information that completely characterizes the electrical transport properties of a material. The electrical measurement of the synthesized nanowires was done by using a Keithley Picoammeter 6485, computer controlled power supply (Redlab 4301, from MeilHaus Electronic GmbH) and chip holder device. The Keithley picoameter enables to measure very small current values in micro- as well as nanoampere scale. Figure 4.12 shows a custom made chip-holder device which was used for a direct current (DC) conductance measurement of both horizontal and vertical (e.g., nanoseaurchins and nanosails) nanowires. It consists of 12 easily adjustable gold pins and is designed to fit each chips (inset in Figure 4.12) so as to avoid contact instability. The numbers (1, 2 and 3) on the chip represent one of the possible electrical contacts, where usually 3 was used as a reference. For instance, in the case of horizontal nanowires synthesis each contact junctions (shown in the white arrow in the inset) consists of nanowires. The

nanowire integrated microchip is then mounted into the device as shown by the red arrow where it is further connected to a Keithley Picoammeter and a power supply. Thus, the conductance measurement of the wires can be carried out by using either contact 1 or 2 in reference to 3.

5 Synthesis and Characterization of Horizontal Nanowires

Nanowires with the transverse direction well below 100 nm are one of the best candidates for further technological miniaturization. They have been proposed as being potentially important in the development of interconnects and active components in future nanoscale electronic, magnetic and photonic devices. The presence of two confined directions in nanowires enable them to exhibit different electronic properties unlike their bulk counterparts, which includes enhanced surface scattering effect, change in screening length etc. Moreover, the high aspect ratio (length/diameter) of nanowires give them an advantage among nanostructures for biological and chemical sensing applications. Due to their unique properties, they have drawn huge interest in various research area of physics, materials science, and chemistry.

Several techniques have been developed for the fabrication of one dimensional structures by various researchers. However, extended investigation was given for few of these techniques due to various reasons (*e.g.*, cost, versatility, reproducibility etc.). The nanowire fabrication method falls into three broad categories: lithographic technique (*e.g.* photo- and e-beam lithography), template-assisted synthesis (*e.g.* electroplating and electrophoretic deposition), chemical synthesis and self assembly.

The present chapter includes a detailed description of nanowire fabrication from various metallic and semi-conducting materials, different characterization techniques used for structure and morphology analysis of the synthesized nanowires and study of their electrical properties under various conditions.

The chapter is further subdivided into different sections and subsections. The first section explains detailed experimental procedures, which begins with discussing about the observed phenomena during resist film cracking. The crack

formation on a thin film is a primary step for the horizontally aligned nanowire formation. The second section mainly focuses on the electrical properties of the already synthesized nanowires under different conditions. Moreover, discussions regarding the sensoric properties of the various nanowires and different methods of nanowire anodization and their corresponding electrical properties are also included.
The nanowire synthesis approaches used in this thesis, basically combines both the bottom-up (nanowire formation) and top-down (resist microstructuring) techniques. It is mainly based on a relatively controlled thin film fracture, which was then used as a template. It presents a simple way of device fabrication based on integrating the synthesized nanowires into silicon micro-chips.

5.1 Experimental Details

5.1.1 Nanowire Fabrication

The fabrication of nanostructures such as nanowires in a rapid and cost effective method has still been a challenge in nanotechnology over the past several years. Precise techniques for structuring on the nanoscale exist, but in most cases the techniques used are either relatively slow, expensive (e.g. electron-beam [34] or dip-pen lithography [35]) or material specific, and are often limited to distinct deposition techniques. On the other hand, the cost effective self-organized techniques often suffer from a lack of controllability; leading to problems to connect nanowires in a desired way and integrate them into standard processes.
One alternative and relatively simple technique is based on thin film fracture [36–39] which involves the usage of cracks as a template for a nanowire synthesis. The detailed mechanisms and general behavior of thin-film cracks have been thoroughly investigated in the past decades [40–44], and even the crack generation as well as propagation under different circumstances were also studied. Cracks are associated with the mechanical failure of a material and can be observed on different objects at different scales such as drying muds, spin-coated organic-inorganic coatings at higher temperature [45], low K-dielectric thin films [46] etc. As a consequence, they are often seen as a problem and undesirable, therefore researchers focus on finding ways of prevention.

The formation of the desirable cracks in the thin film can be done in two ways: by bending of flexible substrates covered with brittle thin films or by exposing the film/substrate system to a drastic temperature change which induces high thermal stress in the film attached to a rigid substrate. The latter means of crack generation is due to difference in thermal expansion coefficient between the substrate and a fragile film. Moreover, this crack generation can also be "guided" by introducing pre-defined weak sites [37, 39] which will be discussed in the next subsection. The mesoscopic or nanoscopic cracks which are intentionally produced by these techniques can be used as templates for the fabrication of nanoscale wires; even both controlling the wire dimension and fabrication of two different nanowires were also possible by using those templates as shadow masks [38]. Using shadow masks for the fabrication of nanostructures have been also reported elsewhere [47, 48]. However, the challenge so far in this thin film fracture approach is on the fabrication of these cracks in a well controlled, designed, and reproducible way in an integrated surrounding, particularly the formation of defined contacts as interface to the macro-world, e.g. on a silicon microchip.
The synthesis of nanowires based on a controlled crack formation at a predefined site requires proper selection of a brittle thin film which can be easily prepared and fractured with good reproducibility. Among the easily fractureable materials, Shipley 1813 photoresist and polymethymethacrylate (PMMA) showed reliable mechanical properties. The basis of this particular fabrication and integration technique of the nanowires into microchips is based on the possibility of synthesizing different types of nanowires integrated into a chip in a relatively simple approach as compared to other scientifically suggested techniques. In general, the fabrication procedure contains five main steps as illustrated briefly in Figure 5.1 (a) - (f). The first and the primary step of the process was deposition of a photoresist (or PMMA in the case of e-beam lithography (discussed in section 5.1.1.2) with various thicknesses on thermally oxidized silicon samples (SiO_2 thickness of 100 nm) by spin-coating on p-doped silicon substrate (76 mm diameter, p-doped, 1-10 Ωcm resistivity, 380 mm thick, $\langle 100 \rangle$ oriented. Second, photo-lithography and e-beam lithography were used to microstructure the photoresist and the PMMA, respectively. This microstructuring of these thin films on a silicon substrate helps to:

- Prepare micro-scale electrical contacts while synthesizing the nanowire simultaneously, and
- Create and analyze different geometries of thin films in order to form desired pattern of cracks after thermal cycling by creating weak sites on the film.

This process enables to form a predefined site where, , most likely, the failure of the film is to occur as the stress field is expected to concentrate on the weakest site. Figure 5.2 (a) and (b) shows one of the microstructured resist thin films on a silicon wafer and a microchip, respectively. The microstructured resist/silicon wafer consists of 20 microchips with 4 additional different microstructure designs. The crack generation on the resist (third step) was done by baking the microchips at a temperature of 360 K for about half an hour. The already baked sample was then exposed to thermal cycling down to cryogenic temperature mainly by using liquid nitrogen (temperature about 77 K) for few seconds (between 3 to 5 seconds). This process can be carried out either by a direct dipping of the thin film coated sample into liquid nitrogen or by exposing it to a liquid nitrogen steam. The baking temperature as well as the liquid nitrogen exposure time was optimized to get the desired cracks, as the fracture property of the film depends on the condition during film preparation. The drastic thermal change induces thermal stress in the resist film which leads to the formation of nanoscopic or macroscopic fracture patterns upon relieving the film stress. The fourth step (the vacuum deposition of the electrical contacts and the nanowire material as shown in Figure 5.1 (d)) and the final steps (mask lift-off) will be discussed at a later stage in the subsections to follow.

5.1.1.1 ”Controlling” or ”Tuning” Crack Patterns

The formation of cracks on bare thin films materials are often relatively uncontrolled, mostly random and can even cover the whole area of the thin film. This phenomenon is one of the difficulties of cracks to be used as part of functional templates for a nanostructure fabrication by filling them with a necessary material. Thus, the great challenge, so far, is the formation of ”controlled” micro- or nanoscale cracks in a desired pattern at a desired location. To solve these and other related problems, several methods have been developed on different types of thin-film/substrate system in the past years. One of these methods was

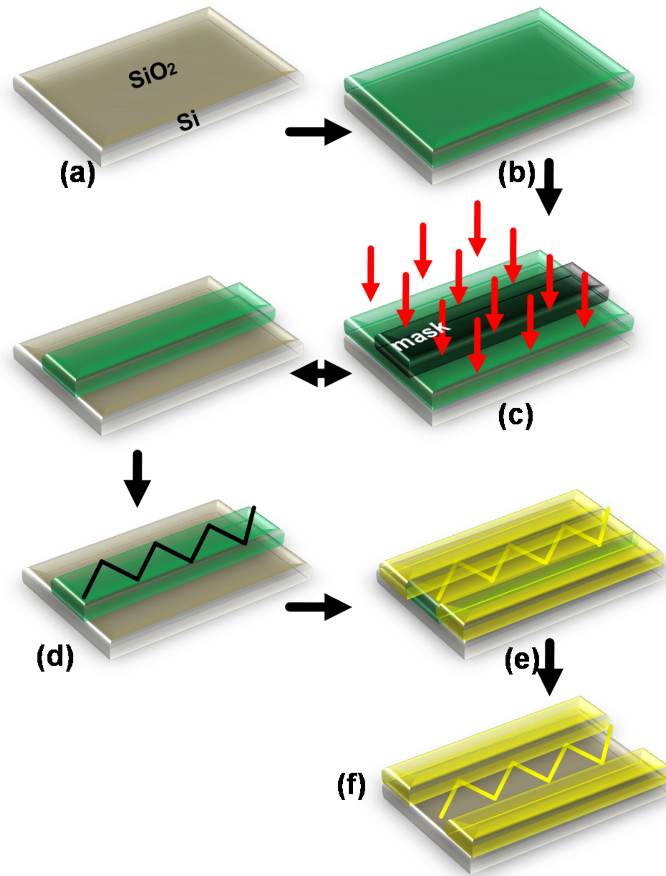

Figure 5.1: *General processing steps for nanowire fabrication based on thin film fracture. A well cleaned silicon substrate with* 100 *nm thick oxide is masked by a photoresist film by spin - coating (b). A microstructuring process by exposing the thin film with UV or e-beam lithography to create a suitable design (c) by using a mask yields a rectangular shape film after removing the UV exposed area (e.g. for positive resist). The cracks generation by thermal cycling (d) and finally the material deposition(e) and successive mask lift-off results formation of nanowires and electrical contacts (f).*

by creating a predefined site where the strain field is expected to concentrate and lead to fracture. This type of method was done by using a microstructured photoresist films on a silicon substrate as shown in Figure 5.2. The resist microstructuring was done by using conventional photo-lithography technique. The microstructured photoresist wafer consists of 20 (each 1 cm^2 area) microchips (Figure 5.2 (b)) and each chip has eight resist stripes with 6, 8 and 10 μm width

as shown by the arrow in Figure 5.2 (c) along 200 μm length. This gives in principle the possibility for mass production of cracks which are ready to be filled by materials needed. These microstructuring of the film enables the fabrication of a relatively well ”controlled” (patterned) crack formation at a predefined site. Similar ”controlled” alignment of cracks have also been observed on a stainless-steel foil substrate [38] where a simple application of the uniaxial bending can result cracks arranged in parallel. However, the fabrication of two parallel cracks, for example, on a rigid substrate is in principle difficult since the two strain fields associated with the cracks prefer (tends) to join each other. These types of phenomena (mechanism) of thin film fracture have been studied thoroughly [49]. The

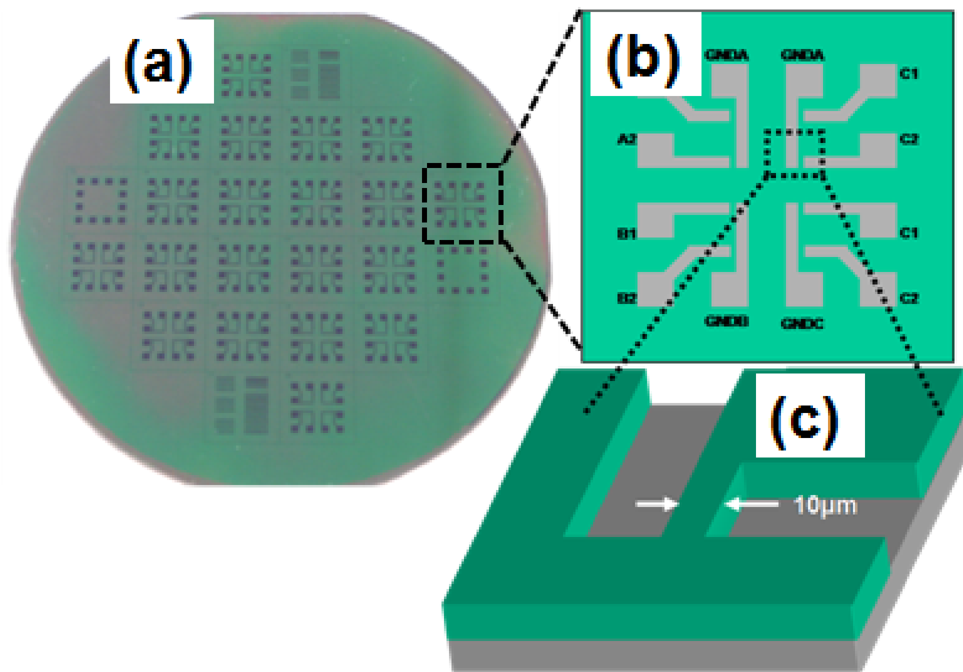

Figure 5.2: *Microstructured photoresist on Silicon substrate (a), the magnified image of one of the microchips (b) and the site where patterned cracks were observed (c).*

examination of several shapes of microstructure pattern reveal that simple rectangular stripes of photoresist are very effective to create a well ordered fracture patterns. This simple shape of the photoresist has shown high reproducibility of crack formation. The cracks formed in these stripes are well organized and follow a ”zig zag” pattern. However, this pattern was not observed for all widths

of stripes as shown in Figure 5.3 since the strip dimension plays an important role on the design of the pattern that the cracks follow. For a 10 μm strip width, for example, the cracks are very well defined and equidistantly distributed. They are about 20 which are aligned in 45^0 to each other across the 200 μm length and are the most reproducible. In contrast, 8 μm and 6 μm stripes appear to be more irregular as shown in Figure 5.3 (b) and (c), respectively. These patterns are believed to occur as the result of biaxial stress developed during temperature treatment of the film, however for a detailed understanding of the patterns observed for those different strip's dimensions further study needs to be done. The connection of the nanowires, obtained after material deposition and lift-off, is a further advantage of the setup as it guarantees a certain defect tolerance: if one single wire fails, the others still perform, changing the overall electrical performance in a tolerable way.

Different mechanisms were observed on the resist film when they are subjected to

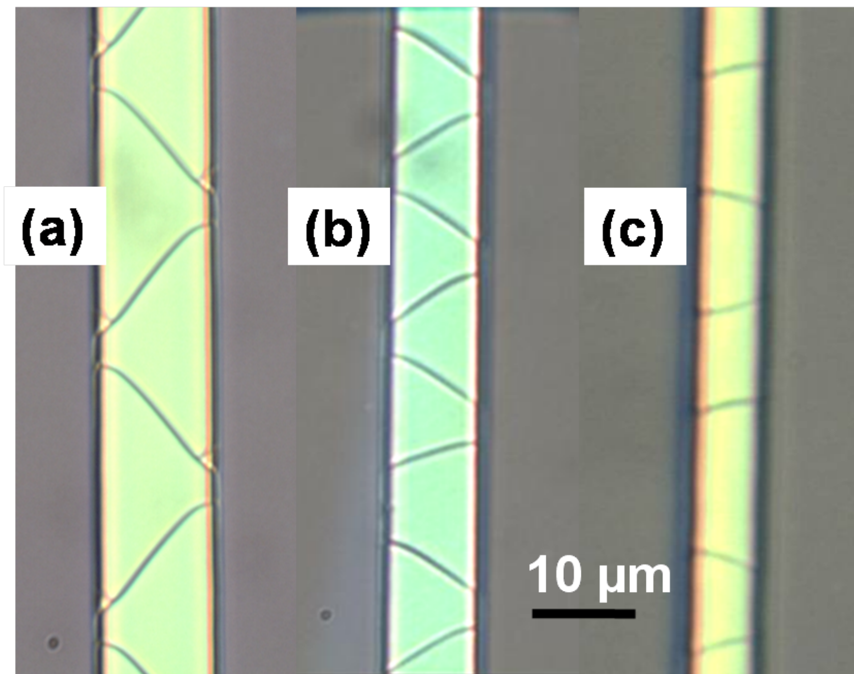

Figure 5.3: *Optical microscopy of different crack patterns on a* 10 μm *(a),* 8 μm *(b) and* 6 μm *(c) stripes.*

drastic temperature change by causing a thermal stress in the film. These include resist buckling, buckle-driven delamination [50, 51], worm-like (telephone cord)

patterns as shown in Figure 5.4, and some micro-scale branches with "Lambda" structure close to the contact was also observed (marked in square in Figure 5.4 (a)). Figure 5.4 (a) shows the buckle driven fracturing phenomena which was observed on 10 μm strip. This type of buckling (debonding) from the substrate and subsequent delaminating of films occur upon releasing compressive stress [52] and usually occurs when buckling stress exceeds film fracture stress. Figure 5.4 (b) and (c) show the partial film buckling and the sinusoidal type buckled features called telephone-cord on 8 and 6 μm strip dimensions, respectively. They occurred as a result of the biaxial compression which is induced by the thermal stress, and this type fracture pattern has been observed in several thin film systems [53, 54]. The sinusoidal crack patterns on bulk materials [55] usually shows dependence on the immersion velocity and the temperature gradient which also shows a little influence on the resist film during crack formation.
The compressive stress developed in an elastic rectangular shape strip is determined by different factors such as width of the strip (b), thickness of the film (h) etc. and can be described as equation 5.1 [56],

$$\sigma_E = \frac{E\pi^2}{12(1-\upsilon^2)}\left(\frac{h}{b}\right)^2 \tag{5.1}$$

where σ_E is the stress on the film, υ is Poisson's ratio and E is the elastic modulus.
The above equation clearly shows how a compressive stress depends on the strip dimension, which plays an important role on the formation of the three different film fracture mechanisms for the same resist thickness during cracking. Moreover, the film thickness dependence of the stress [41, 49] led to find the critical photoresist thickness, under which no cracks can be formed. Hence, the optimal thickness of the photoresist was identified by investigating the crack behaviors observed at various resist thicknesses. In doing so, a 560 nm-thick photoresist film was found to be optimal for the formation of the desired cracks. If the film was too thin (below 400 nm), the stress developed in the film seems not enough to induce the fracture in the third step, and yielded almost no cracks on the resist, whereas when the film was too thick (above 1000 nm), the risk of uncontrolled delamination of larger parts of the photoresist film was very high, and the cracks could not be guaranteed to reach down to the substrate.

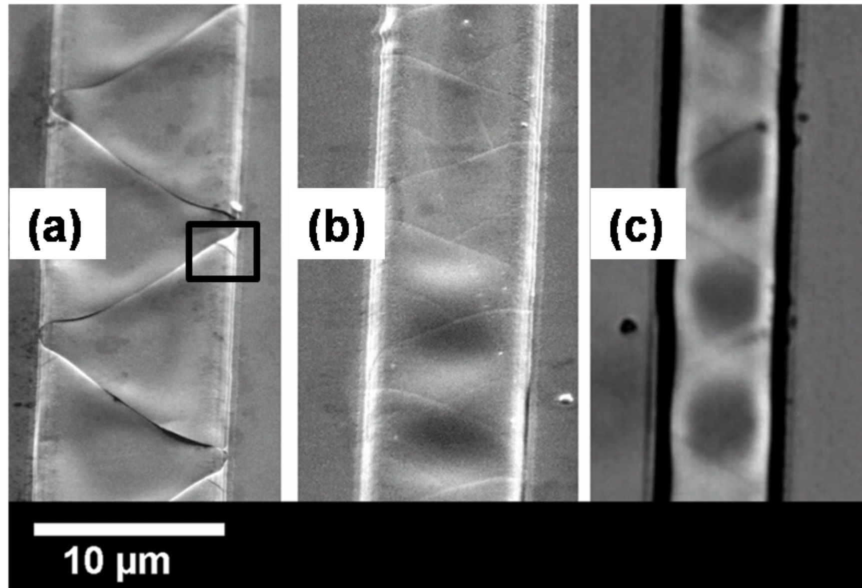

Figure 5.4: *The Scanning electron microscopy image of photoresist film upon thermal cycling. Buckling-driven delamination (a) buckled (b) and worm-like or telephone cord formation (c).*

5.1.1.2 Nanowire-Material Deposition

A choice of the metalization technique can strongly affect the final nanowire morphology and its physical properties. The material deposition technique (fourth step) used here, was based on physical vapor deposition (PVD) which often result polycrystallinity in the deposited film. The desired material for the nanowire formation was done selectively by magnetron sputter deposition under ultra high vacuum (UHV). The sticking properties of the metal on the substrate is crucial to form a uniform and continuous nano- or mesowire. Hence, before the desired metal could be deposited an adhesion promoter was used to ensure that the sputter deposited material sticks well to the substrate; this could be either evaporated chromium (Cr) or sputter-deposited titanium (Ti) both with 99.99 % purity from Goodfellow industry. One of these metals, with thickness about 3 nm, was deposited while the sample was kept under rotation. The rotation of the sample while depositing material increases the possibility of material covering of the crack opening area to reach down to the substrate. This minimizes the shadowing of the delaminated cracks which has a high aspect ratio (typically the

crack opening at the top is between 100 nm and 150 nm, while the film is 560 nm thick). The metal was deposited under a base pressure of 10^{-8} mbar for the adhesion promoters (particularly Cr) and under argon pressure of 3.4×10^{-3} mbar for the nanowire materials during sputtering. The metal deposition covered the whole area including the cracks, therefore an additional micromask was used to deposit exclusively on the cracked rectangular strip so as to avoid any short circuits. The novelty of this nanowire fabrication technique relies on the possibility of fabricating various types of nanowires, and has better advantage than other methods which are mostly material specific. The fabricated nanowires includes, for example, gold (Au), palladium (Pd), nickel (Ni), platinum (Pt), zinc oxide (ZnO) and Ti which were able to be sputter deposited at a thickness of about 50 nm, and at a rate of 0.5 Å/s, to form the corresponding metal nanowires. The substrate was kept at room temperature during the metal deposition process.
Since the deposition of the material by this method also covers areas outside the cracks, a further step is required. Therefore, to separate the nanowires (or material filled cracks), mask lift-off was done consecutively. This process was performed by first soaking the sample in acetone for about 1 min and then keeping it in an ultrasonic bath (BANDELIN, Sonorex, frequency - 35 Khz) for roughly 2 s. Keeping the sample in the ultrasonic bath for too long may destroy the nanowires. The subsequent depositing and removing of the superfluous materials resulted in the formation of 20 well-defined "zig-zag" metal nanowires across a 200 μm channel.
Furthermore, the angular deposition of the nanowire material on the delaminated cracks as a mask yielded either "zig" or "zag" wires as a result of an angle dependent shadowing effect. Based on this shadowing effect, the creation of two parallel or connected nanowires from different materials by a similar approach was also possible, as reported in previous work [38]. The "zig-zag" patterned nanowires are already connected to larger rectangular electrical contacts, which was done simultaneously during the nanowire material deposition. However, outside of the micro-scale channel, only random wires were observed (see Figure 5.5 (a)). For the integration of these nanowires into devices and thus to analyze their electrical properties, this random network formation was avoided by covering the sample with an additional mask during deposition process. The atomic force microscopy (AFM) image in Figure 5.5 (b) shows the as-synthesized nanowires after per-

forming the whole processing steps. It shows a granular structure with a rough surface area, which enables the fabricated nanowire to have a better functional advantage for sensor applications. The thickness variation of individual grains is seen in the AFM image in Figure 5.5 (c) which shows the change in the wire topography (roughness). However, due to the inherently limited resolution of

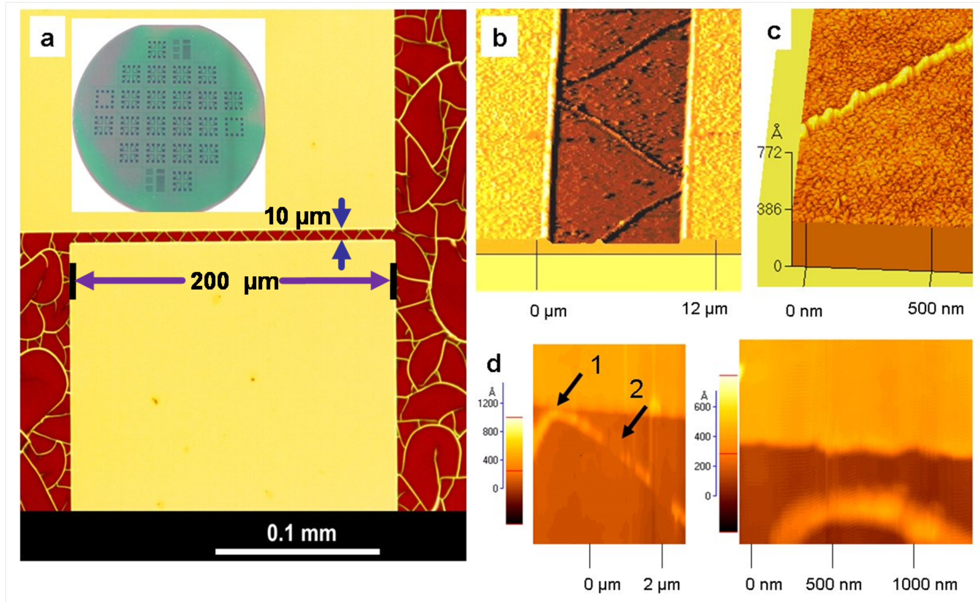

Figure 5.5: *Images of Au nanowires (NWs) integrated in a microchip. Optical microscopy image showing a well-organized "zig-zag" pattern of NWs between two electrical contacts (yellow areas) (a). In contrast, next to the contacts, an unorganized pattern of wires can be found. The photographs in the inset show the wafer (7.62 cm in diameter) consists of chips (each 1 cm^2); the position where the microscopy image was taken is marked with an arrow. AFM image of polycrystalline Au NWs (b). Magnification of (b) showing the typical thickness variation along the NW (c), indicating the granular nature of the wires, which is important for sensor applications. Typical fabrication problems (d). Arrow 1 points to a swing by of the NW caused by a thickness gradient in the step edge (magnified on the right), and arrow 2 shows a discontinuity.*

AFM determined by the shape of the tip, the gaps between the grains (clusters) could not be resolved.

Generally, the fabrication of the nanowires by using a thin film fracture approach can be highly influenced by many factors, which have to be considered. These

factors include: the ambient conditions during the microstructuring of the resist (e.g., humidity, pressure, etc.), the thickness of the film (as mentioned earlier), the temperature to which the film was baked during crack formation, and the degradation of the resist film over time (e.g., from light exposure). One of the important factor for the achievement of reproducible crack patterns is the uniformity of the resist thickness whereas a thickness variation could lead to a defect formation which could result; (i) cracks which were not connected to the electrical contacts (causing a ”swing by” of the nanowire) as shown in Figure 5.5 (d), (ii) in discontinuities or (iii) in mask peel-off resulting in total destruction of the nanowire mask. Usually, the latter case occurs if the photoresist is too thick. In thicker films, more strain could be built up and thus a larger force was acting on the interface, leading to delamination. In contrast, not enough strain was built up under a critical film thickness, which showed no cracks upon thermal stress was induced.
Figure 5.6 shows the other application of the microstructured thin film fracture approach for formation of a suspended nanowire at a specific location. The synthesis of this type of nanowires was done in the labs of TU-Illmenau by Dr. V. Cimalla (now Fraunhofer Institut für Angewandte Festkoerperphysik, Freiburg) by microstructuring the Poly(methyl methacrylate) (PMMA) film using e-beam lithography technique. Following a similar procedure as illustrated in Figure 5.6 (a) (also similar to the basic processing steps outlined in Figure 5.1), which includes spin coating, film microstructuring, cracking, material depositing and lift-off process, a nanowire could be formed. The ”bow-tie” type pattern, as suggested elsewhere [57], was used to create a predetermined breaking point at the thinnest part of the photoresist film. As strain concentration occurs preferentially at notches, they act as a starting point for crack formation. Figure 5.6 (b) shows the result after all process steps were completed and a further substrate etching step was performed: a free-standing bridge composed of suspended Ni nanowire between two electrodes was created. In principle, these types of structures can be used as mechanical resonators [58, 59]. The ”bow-tie” structures are also very useful for basic research [60] and are an example of the broad application of the nanowire synthesis approach, being discussed here. But in terms of reproducible fabrication, it turned out that the ”zig-zag” type of nanowire formation was much more reliable.

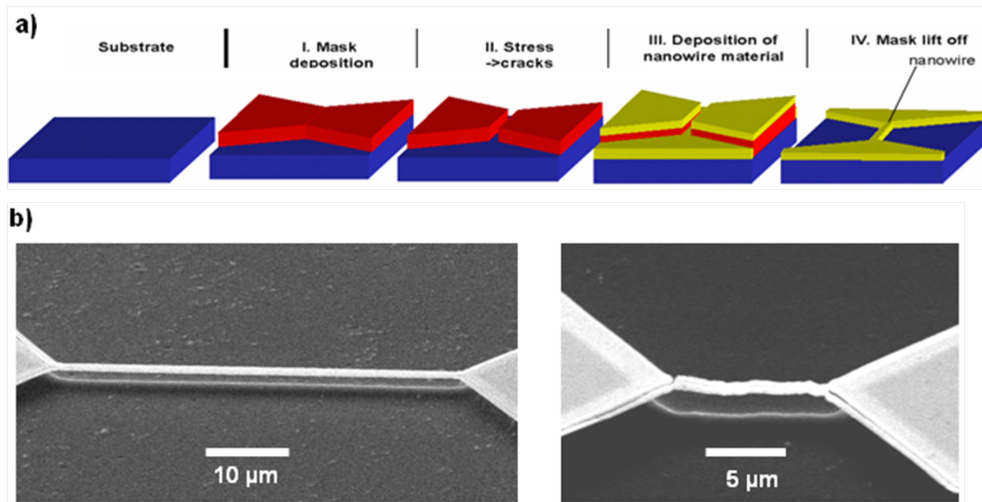

Figure 5.6: *Sketch of the NW formation steps for the bow-tie-type microstructure pattern (a) and SEM image of the contacted NWs after cracking of the resist film, metal deposition, and mask lift-off (b). A further etching step converts the wires into a free-standing bridge.*

5.2 Results and Discussion

5.2.1 Electrical Characterization of Nanowires

The integration of nanowires into devices is the vital step for building functional electronic devices. Unlike other nanowire synthesis methods which require the manipulation of nanowires for integration, the synthesis approach, used here, enables easy fabrication and gives an opportunity to analyze them further. A primary and fundamental attribute of such a two terminal nanowire- based device is electrical continuity, *i.e* the ability to transport charge carriers along its length under a longitudinal potential bias. The electrically continuous nanowires then can be further investigated by carrying out several tests. The following subsections discuss different properties including the electrical characterization at different temperature regimes, and study of the oxidation properties of the polycrystalline nanowires. The first test of sensoric properties of the synthesized polycrystalline wires are also presented.

5.2.1.1 Room Temperature Current - Voltage Characteristics

The room-temperature electrical measurements were performed under ambient conditions using Au contact pins connected to the fabricated nanowire circuits. The current through the nanowire circuit was measured by using a Keithley 6485 picoamperemeter (which is optimized for measuring the extremely small electrical signal) while increasing the voltage from 0 to 2 V. The resistance of each nanowire was extracted from the slope of the current-voltage (I-V) curve below 0.5 V. Figure 5.7 (a)-(d) shows a set of I-V curves for Au and Ti nanowires. A correlation of the I-V curve with nanowire thickness (diameter) is not obvious since the wires are a polycrystalline, and it is not possible to resolve each grain in the $\approx$ 14 μm long wires. However, a correlation between the nominal thickness deposited and the resistance was observed. The electrical property of these nanowires will mainly be influenced by the ”largest” gap between the grains. Higher electrical resistance values were recorded from the I-V curve of these nanowires (shown in Figure 5.7) as compared to their corresponding bulk counterparts. This properties of the nanowires is due to strong confinement, which enhances surface- and grain-boundary scattering [61]. The scattering phenomena decreases the mean free path (λ) of the conduction electrons which therefore decreases the electrical conductance of the wire. The curves show an almost linear characteristic up to a certain bias voltage (around 500 mV) in almost all nanowires. However, at higher voltages, current fluctuations were observed, mainly, in the Au nanowires (see Figure 5.7 (a) and (b). However these were not often observed on the Ti nanowires 5.7 (c) and (d). The current fluctuations at higher voltage are very likely due to high fields and high electric current density which is known to enhance cluster (grain) fusing [62] and electromigration [63, 64], respectively. The cluster-fusing effect is illustrated by the sketches in Figure 5.8 (c) and (d). Upon increasing the voltage (i.e., enhancing the induced field between the grains), the gaps with high voltage drops will tend to decrease by changing the shape of the metal grains. As a result, the potential barriers between the grains will reduce which then allows the electron transport from one grain to another and enhance the electrical conductance of the wire. While Figure 5.7 (a) and (b) shows only small variations around 500 mV, appearing as small noise, the changes in the I-V characteristics of the Au nanowire in Figure 5.8 (a) are more pronounced. These wires have 10 times less resistance due to smaller dimensions and/or larger

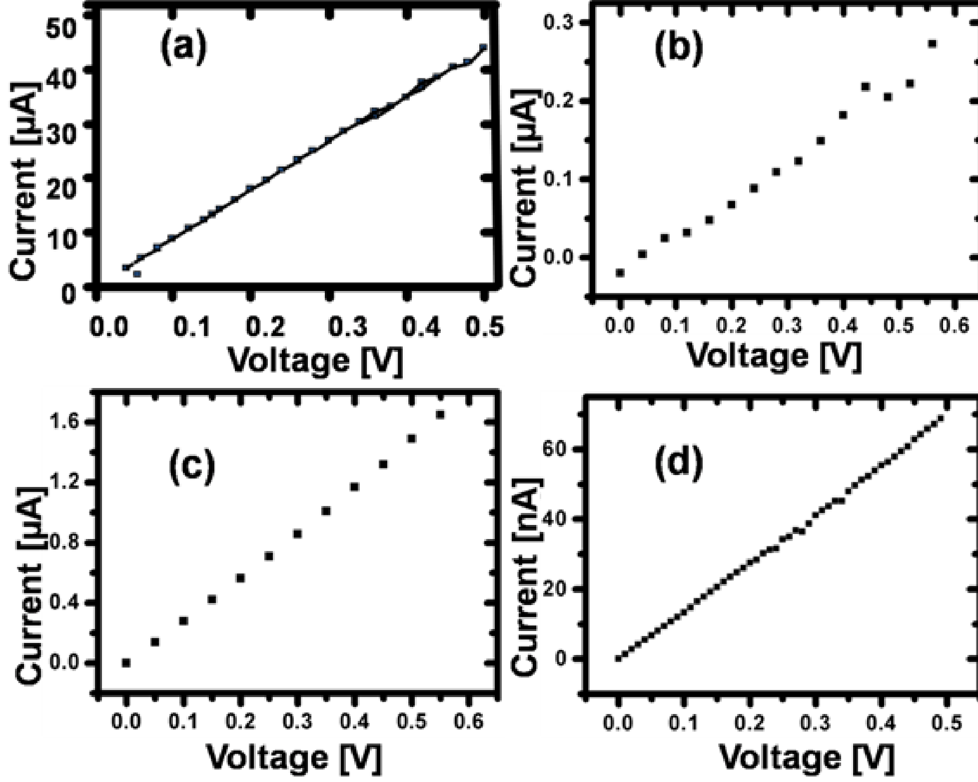

Figure 5.7: *The I-V characteristics of both Au nanowires with resistances of* 10 $k\Omega$ *(a), and* 2.6 $M\Omega$ *(b), and Ti nanowires with resistance* 4 $M\Omega$ *(c) and* 0.01 $M\Omega$ *(d). Current fluctuation at higher voltage was observed in Au nanowires.*

gaps between the grains. Around 500 mV an increase in conductance could be observed, and further decreasing the voltage caused a continued increase in conductance (loop one). Ramping to higher voltages in a second loop caused an even more pronounced increase in the current, further confirming the change in grains to a certain extent. The long delay time of the phenomenon is particularly interesting. The ramping down of the voltage occurs in a matter of seconds; even at lower voltages an increase in conductance can be observed. Obviously, there is some threshold or barrier value that has to be overcome to induce reorganization. If the largest gap closes, the voltage drop at the second-largest gap will be increased, leading to a cascade down through the smaller gaps. Increasing the voltage can, in contrast, also initiate electromigration as a result of the high current density ($\sim 10^{11}$ A/m^2) through the wire. This increases the resistance of

the wire, as shown in Figure 5.8 (b), region I, where a wire with an even lower conductance is used. Eventually, the permanent destruction of the nanowire occurs when the current is further increased. The fluctuation phenomena depend strongly on the size of the nanowires as well as on their material composition. In general, precious metals fluctuate at significantly lower current than other transition metals, such as Ni or Ti, under ambient conditions. The integrated nanowires fabricated here allow, in principle, detailed studies of this behavior, as vacuum deposition techniques allow a variation of crystallinity, grain size, composition, and in this case the height and width of the nanowires [38].

From the room temperature I-V behavior of these nanowires, it can be concluded

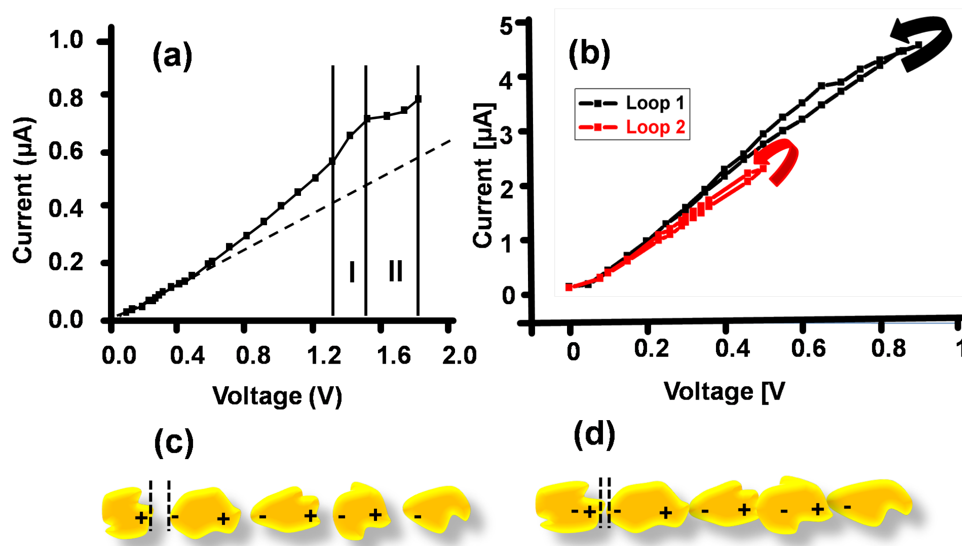

Figure 5.8: *The I-V characteristics of Au nanowires with resistances of* 3 *MΩ (a),and* 0.25 *MΩ (b). Sketch indicating the polarization by the high electrical field between grains (c), and grain fusing leading to the formation of a path of enhanced conductivity (d).*

that the driving voltage for these nanowires devices should stay below 500 mV.

5.2.1.2 Variable Temperature Electrical Characterization

The presence of gaps between the grains in the nanowires very likely favors a hopping conductivity mechanism [65]. To study this electrical transport properties, various variable-temperature measurements were performed under ambient

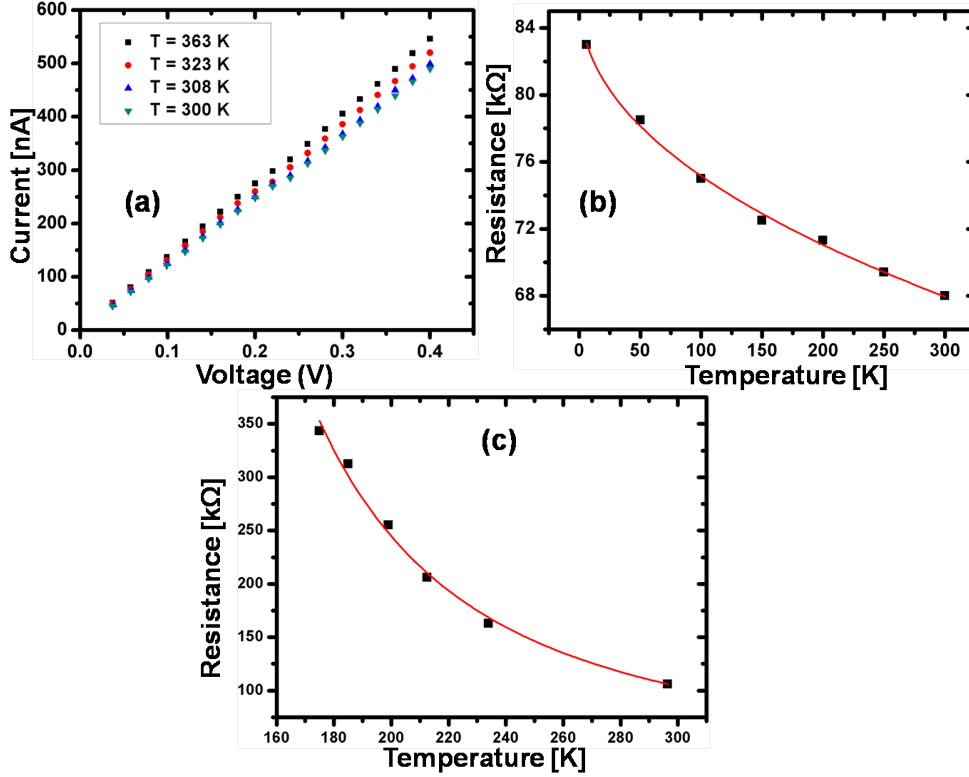

Figure 5.9: *Temperature dependence of nanowire resistance: I-V characteristics of Ti NWs upon heating from room temperature to* 363 *K (a). Resistance versus temperature at* 100 *mV for Au (b) where the red solid line represents the power-law fit to the data ($R \sim T^{-\alpha}$), and the fit for Ni NWs shows a* 1*D variable-range hopping (VRH) ($R \sim exp(T_0/T)^{0.5}$ (c).*

condition. Figure 5.9 (a) shows the I-V characteristics of Ti nanowires under different temperatures. Unlike the bulk counterpart, the measurements show an increase in the conductance of the nanowires upon increasing the temperature. It was conducted by heating the Ti nanowires to a fixed temperature in the small temperature range $(300 - 363)$ K. Measurements of the corresponding I-V characteristics was carried out below 500 mV in order to avoid fluctuations. The decrease in the electrical resistance upon heating could be as a result of an increase in thermal energy absorbed by the localized electrons in the grains. This enables more electrons to hop by overcoming the energy barrier between the grain of nanowires as temperature increases.

The variable-temperature electrical characterization helps to gain an insight

into the possible contributions of the different scattering mechanisms within the nanowires. The electron transport mechanism in these polycrystalline nanowires is in the diffusive regime where the conduction is dominated by carrier scattering. Generally, the diffusive nature of electron transport can be attributed to phonon (lattice vibration), boundary scattering, lattice and other structural defects, and the presence of impurity atoms. For the thorough investigation and detailed analysis, it was necessary to go to a wider temperature range including cryogenic temperatures. Figure 5.9 (b) and (c) shows a plot of the resistance versus temperature for Au and Ni nanowires, respectively, which exhibits a nonmetallic behavior. The red solid line in Figure 5.9 (b) represents a fit to power-law hopping model (R $\sim T^{-\alpha}$). On the other hand, the low temperature dependence of the Ni nanowires was able to be fitted to one-dimensional (1D) variable-range hopping (VRH) model (R $\sim \exp(T_0/T)^{0.5}$). These mechanisms could be originated from the nanoscopic dimension of the wires and its polycrystalline nature where the random arrangement of the grains in the nanowires can be considered as a disordered system. A similar type of conduction behavior has also been observed in various disordered materials, where the resistance curves suggested a variable-range hopping mechanism [66–68]. In the other case, increasing the wire thickness led to a transition towards bulk behavior, as the hopping barriers become lower whereas the role of phonons becomes more important. This can be shown in the resistance versus temperature behavior of Ni mesowires (Figure 5.10), which have a nominal thickness of 150 nm. Unlike Ni nanowires, it showed almost constant resistance over a larger temperature range. This effect is most probably due to the combined effect of the two conductivity mechanisms, that is, power-law hopping-assisted conductivity (Figure 5.10 (b)) which is typically thermally activated and a bulk conductivity (Figure 5.10 (c)) at relatively lower and higher temperatures, respectively. This phenomenon is technologically applicable as the temperature stability of current is of great importance for devices such as sensors.

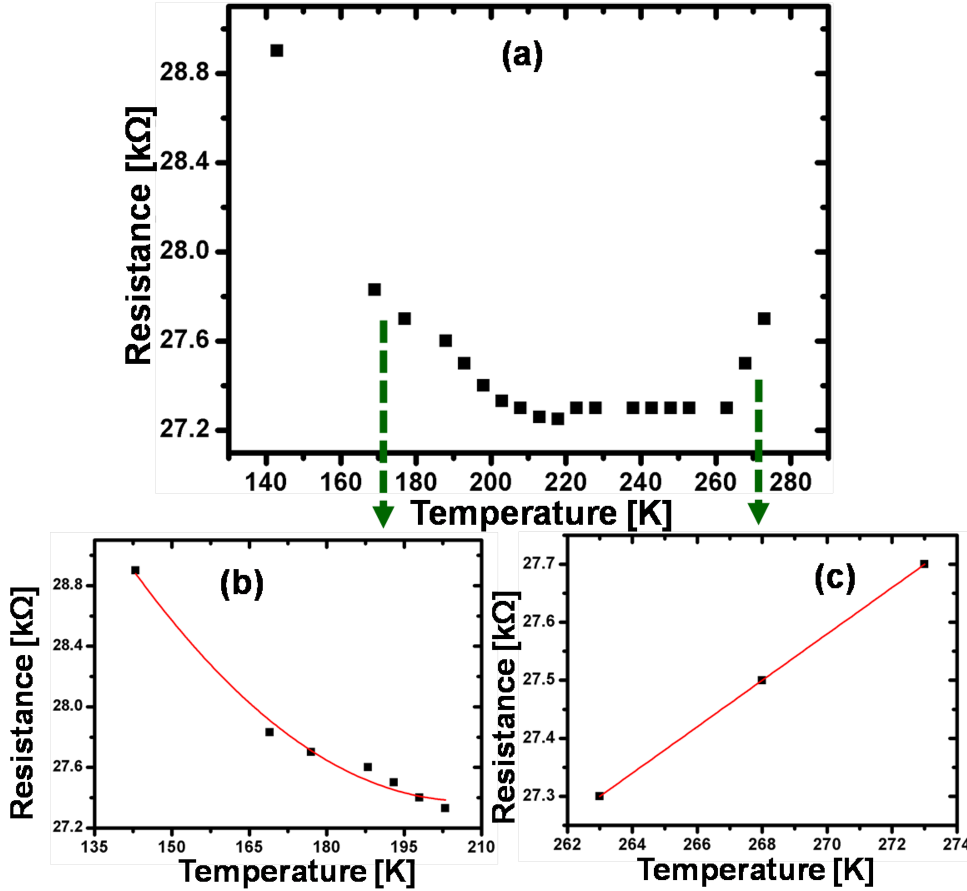

Figure 5.10: *Resistance versus temperature for a Ni mesowire. The resistance changes by only* 0.6 *k*Ω *in a temperature range of more than* 110 *K, representing an effective temperature coefficient of* 2×10^{-4}*, one order of magnitude smaller than the bulk value of* 3×10^{-3}*. The increase in resistance indicates two mechanisms: hopping-assisted transport at low temperatures (b) (the solid line is a power-law fit* $(R \sim T^{-\alpha})$*) to the data) and phonon scattering at relatively higher temperatures (c).*

5.2.1.3 Oxidation of Metal Nanowires

Many metals form compact oxide films when they are exposed to an open air. These oxide formations have been studied and two assumptions were proposed several years ago [69, 70]. The first assumption was based on the diffusion of the metal ions through the oxide film at considered temperature. At the surface between the oxide and air, the metal ions combine with oxygen to form new

layers of oxides, if electrons can get through the layer too from the metal to the free surface. Whereas, the second assumption was proposed on the basis of electron transport through the oxide layer. This electron transport can occur by two mechanisms; either by thermionic emission from the metal into the conduction band level of the oxide or by quantum tunneling. The thermionic induced transport is almost impossible to occur at room temperature if the corresponding work function is greater than 1 eV. Hence, the quantum mechanical effect is the more likely mechanism, but it is only if the thickness of the oxide is extremely small (e.g., < 2 nm).
The kinetics of the oxide film growth was analyzed and studied in detail by Wagner [71] and Cabera and Mott [69] for thick (thickness > 1 μm) and thin ($<$ 20 nm) films, respectively. The Wagner's theory of thick film growth provides a means by which the rate of film growth can be related to other measurable transport properties, such as diffusion coefficients. It had been observed that the film growth obeyed parabolic kinetics i.e. $X^2 = kt$ where X is the film thickness and k is the parabolic rate constant. The parabolic kinetics can be seen consistent with the rate of growth being controlled by transport down by a gradient of driving force, which becomes proportionally smaller as the film thickness increases as

$$\frac{dX}{dt} = \frac{k_p}{2X} \tag{5.2}$$

Thus, Wagner theory is based upon diffusion across the film being the slowest, and therefore the rate-limiting step in the overall sequence of reactions. However, the assumptions in this theory become poor as the film thickness gets sufficiently small. The quantitative as well as qualitative details of an oxide film growth for various materials has been reported elsewhere [72]. On the other hand, the Cabrera-Mott theory describes the oxidation of a thin film in atomistic rather than phenomenological terms. The bases of this theory is that the electron can freely pass from the metal to ionize the adsorbed oxygen atom or molecules at the oxide/gas interface so that the electron electrochemical potential is equal in the metal and the adsorbed layer. As a result, uniform electric field (zero space charge) will be induced in the film by positive surface charge on the metal and negative from excess oxygen ions in the oxide/gas interface. Figure 5.11 shows an energy band diagram which illustrates before and after the electron transfer from the metal to oxygen adsorbed on the surface according to the Cabrera-Mott

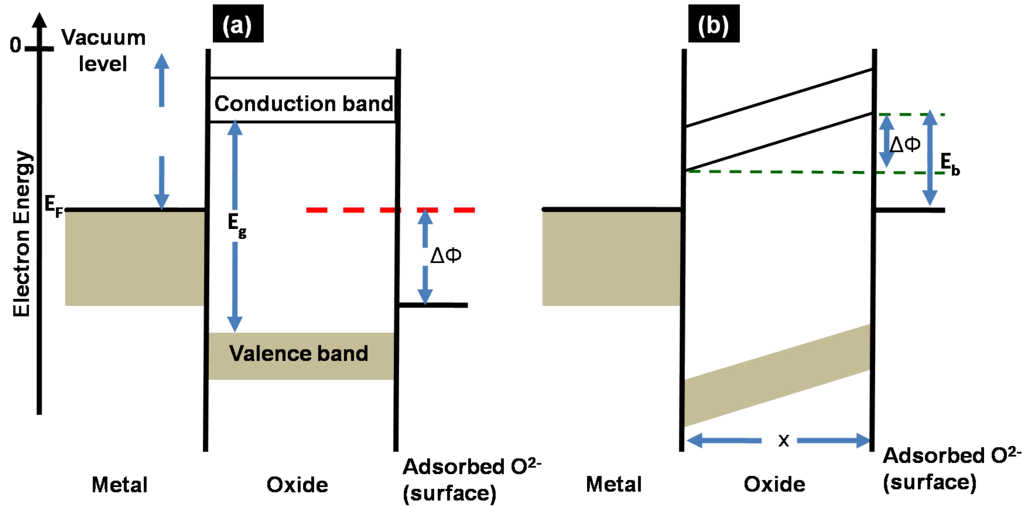

Figure 5.11: *Electron energy level diagrams, before (a) and after (b) electron equilibrium, illustrating how the transfer of the electrons from the metal to oxygen adsorbed on the surface of a thin, growing oxide film generates a uniform Electric field according to Cabrera-Mott theory.* E_b, $\Delta\phi$ *and* ϕ *represent the Mott potential, the voltage across the film and the work function of the metal, respectively.*

theory. In this mechanism of oxidation, the electric field drives the slow ionic transport across the film and causes it to thicken. The electron continues to cross the film readily to maintain zero current.

The local nanoscale oxidation of semiconductors and metals attracts a lot of interest from both scientific and technological point of view. This oxidation phenomena have been observed on three-, two- as well as one-dimensional nanostructures. However, among these, one-dimensional structures are more liable for oxidation due to their high aspect ratio. Therefore, the formation of oxides should be carefully studied since the overall performance of future nanostructure integrated devices could be affected. Nevertheless, a controlled oxide formation has been used for the fabrication of electronic devices. In the coming subsections, the native and controlled oxidation of different polycrystalline nanowires at room temperature will be discussed.

Oxidation of Nanowires at Room Temperature The oxidation of some metals occur if they are exposed in air or upon applying a certain bias voltage. The

rate of oxidation depends on the dimension of the material and expected to be significantly higher for the nanscopic material than their bulk counter part due to high surface-to-volume ratio.
The oxidation behavior of both Ni and Ti nanowires were investigated at room temperature. The experiment was carried out by setting two different conditions; one while constantly applying a bias voltage across the nanowire and the other without. This helps to investigate almost exclusively the effect of either air or field driven oxidation on nanowires. Oxidation plays a major role in changing the electrical properties of nanowires due to their confined scale, therefore it can be more enhanced and becomes a major problem for the persistence of the electrical conductivity and affect the stability of the device. The oxidation behavior of Ni wires can be analyzed by investigating the change in resistance with time under normal atmospheric conditions (native oxidation). The objective of the experiment is to study the "real-world" oxidation effect in the nanowires. For instance, the shelf life time of the device can be influenced by oxidation. Figure 5.12 (a) depicts the behavior of the native oxidation of a Ni nanowires. It shows a slow increase of the resistance over time. The resistance-time measurement was done while applying very low bias voltage in order to minimize the effect of field induced oxidation. In the case of native Ni oxidation, oxygen diffuses slowly at the surface. However, at grain boundaries the rate of oxygen diffusion is expected to be relatively fast. This diffusivity gets weaker due to the formation of thicker oxide width over time, which eventually follows a relatively slow process. As the result, the resistance exhibits a slow increase over time. However, the outcome of the experiment shows a roughly linear resistance behavior over the observed time scale. It can be concluded that the structure is smaller than the normal passive depth. Therefore, the oxidation reaction is not slowed down or stopped at a specific point over this short time scale. The resistance shows a linear-dependent characteristic in these conditions. Hence, it can be assumed that the resistance versus time relation under a normal oxidation is linear.
The other analysis of the oxidation of Ni was done by applying a constant voltage across the nanowires. This experiment gives a clue about the effect of electric field and is vital for electronic devices since the electric current often runs continuously. The influence of the electric field on facilitating the rate of oxide formations on metals [73–75] and particularly on nanowires [76] is widely studied. Figure 5.12

(b) shows the field-induced oxidation of a Ni nanowire while a 0.6 V bias voltage was applied. This bias voltage is capable of inducing very high field ($\sim 10^8$ V/m) since the intergrain separation is expected to be in nanometer range. This effect of field-induced oxidization was done on the already nanowire-integrated circuit. Unlike the unbiased (native) oxidation, the resistance versus time relation was not linear. The presence of the field is found to initially enhance the resistance of the nanowire dramatically from 3 MΩ to 85 MΩ in less than 5 minutes, however, this enhancement reduces upon thickening of the oxide layer, as this makes the migration of the metal cations or oxygen anions, and their diffusion through the oxide layer difficult. The overall process of oxidation could result the formation of the NiO-Ni core shell nanowires by forming a conductive core (Ni) and insulating shell (NiO). The outcome of this experiment can be used to study the device instability as a result of oxidization for nanowire integrated devices, and suggests the minimum current to be used to avoid further oxidation.

Generally, the polycrystalline nature of the nanowire can influence the oxide formation process. The grain boundaries, (i.e. the region of transition between crystals of different crystallographic orientation in contact with each other) act as fast diffusion paths, therefore the oxide is expected to be thicken and the growth rate is relatively fast as compared to the native oxide formation. It is worth to mention that the boundary diffusion properties of a given material depends upon a number of parameters characterizing the boundary and the diffusing species. The fast-diffusion character of grain and interphase boundaries results in many discontinuous solid-state reactions being boundary-diffusion controlled.

Electrochemical Oxidation of Nanowires The local oxidation of metals and semiconductors have been one of the scientific interest for many researchers. Therfore, various anodization techniques have been developed. Among these methods using a conducting atomic force microscope (AFM) [77–79] and scanning tunneling microscope(STM) [80, 81] tip induced oxidation were commonly applied. These controlled and local oxide formation had been used for the fabrication of nano-electronic devices [77, 80, 82].

In this work, before starting locally anodizing the nanowires, several test measurements were done on sputter deposited Ti films which have different thickness; 10 and 50 nm on 7 mm x 25 mm glass substrate. Figure 5.13 (a) shows

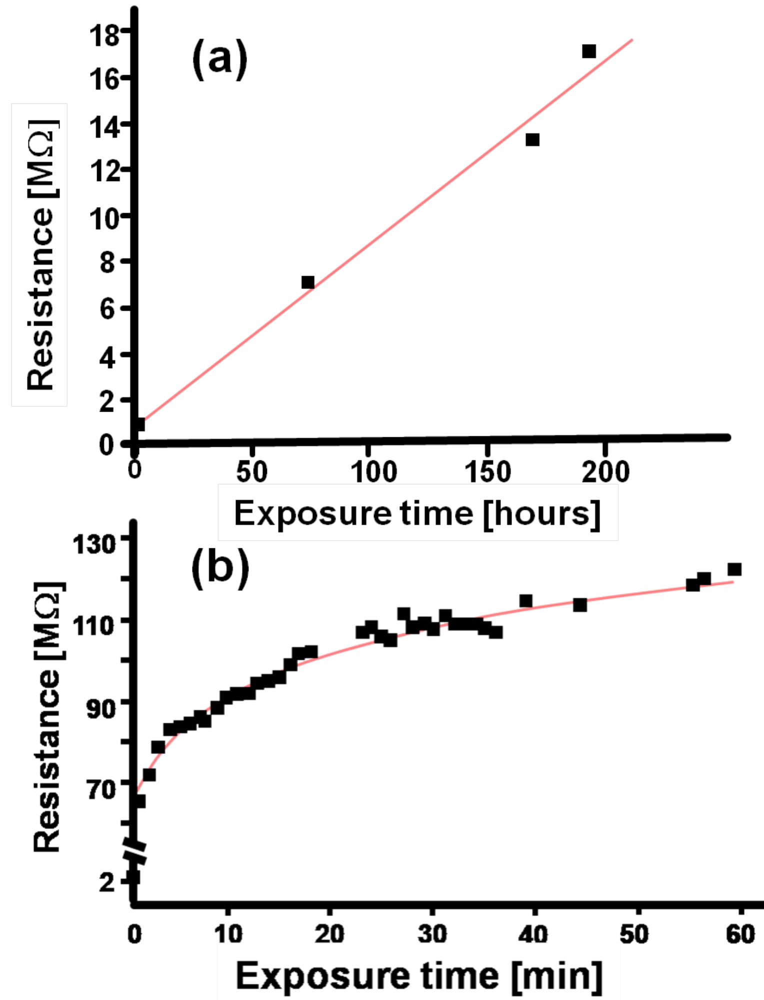

Figure 5.12: *The native oxidation (resistance versus time) (a) and the field-induced oxidation characteristic (b) of Ni nanowires as function of resistance and time.*

the schematic representation of the anodization process used for anodizing both films. Two positively biased (anode) Au rods were used and were kept in contact with the Ti surfaces through out the process. The other negatively biased Au electrode was connected through a water meniscus. The choice of a deionized water with the maximum purity as oxygen source reduces the possibility of residual contamination during anodization process. The use of water as oxygen source for anodization have been reported elsewhere [80, 81, 83]. When a positive bias is applied to surface (anode) relative to the other Au electrode (cathode), the water meniscus works as a small anodization chamber. The anodization and/or oxygen

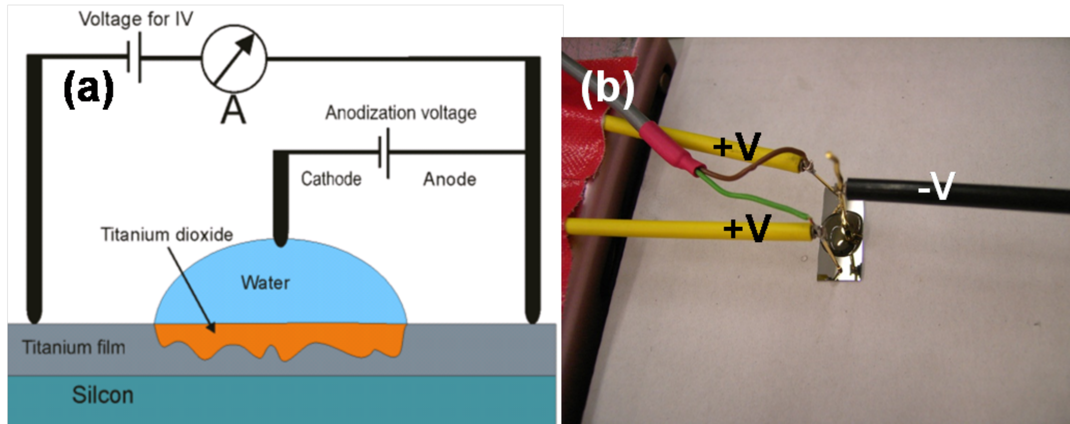

Figure 5.13: *Schematic representation of local anodization of nanowires (a) and the photo showing how the electrodes and the film are potentially biased (b).*

evolution proceed on the sample surface at the point beneath the Au electrode.

Figure 5.14 (a) shows the current measured during the anodization process for a 10 nm sputter deposited Ti films. The measurement was done at 10 anodization voltage *i.e.*, the voltage applied between the Au electrode which is immersed in water and the Ti surface. During the process, the current through the film was measured while applying constant 1 V between the two Au electrodes on the surface of the film. The current shows a decrease through time in both cases. However, high current rate decrease was observed in the 10 nm thick Ti film than the 50 nm thick film (Figure 5.14 (b)) for the same anodization voltage, and the current vanished after about 700 second. This fast current decrease in the thinner film could be attributed to the drastic increase in the thickness of the oxide which was enhanced by the relatively high induced field in the thin film. The post electrical conductivity measurement of the film also showed a decrease which could be due to either the increase in number of the electron trap site in the film as a result oxygen vacancies formation. Two different values of anodization voltage for two 50 nm thick Ti films was also used to investigate its influence on the oxidation process as shown in Figure 5.14 (b). The slight current difference before the start of anodization is due to contact instability which can affect the measured resistance of the film. The 15 V anodization voltage results roughly 45 % decrease in the current through the film, whereas for the 10 V anodization voltage about 25 % current reduction was observed in the same measuring time

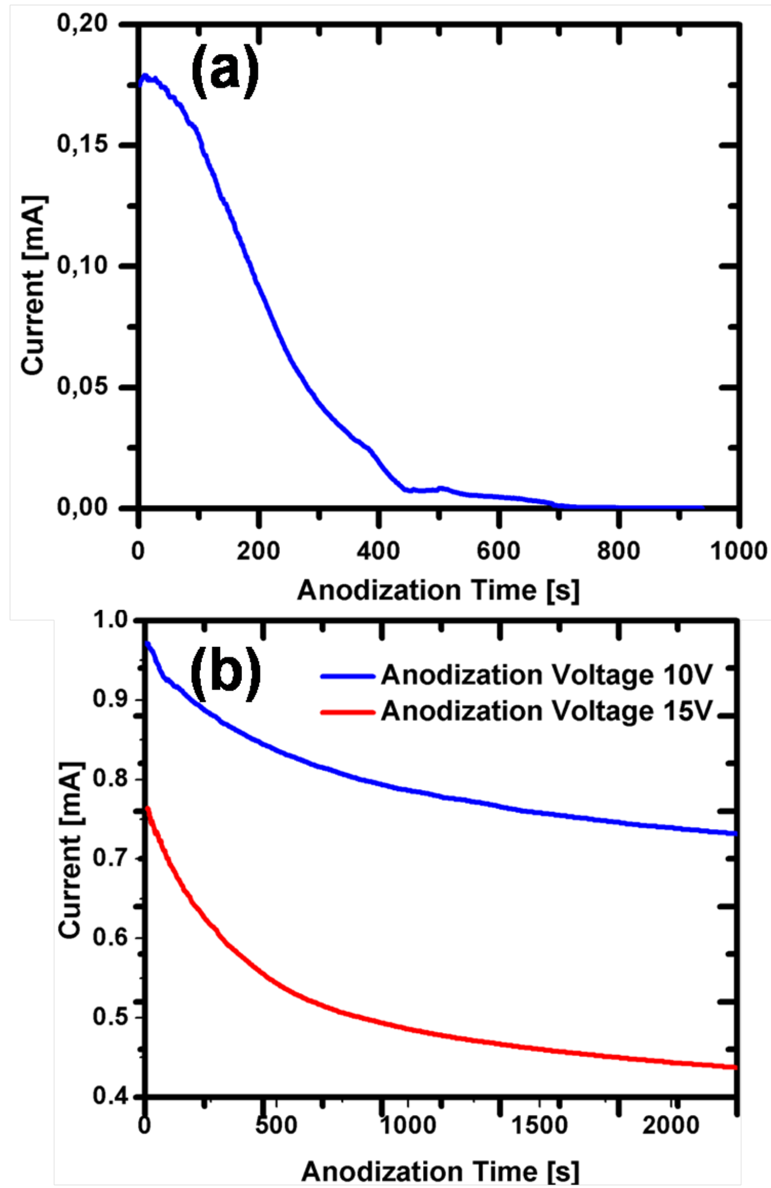

Figure 5.14: *The current versus anodization time of* 10 *nm (a) and* 50 *nm (b). The current was measured through the film during the anodization process.*

scale. This phenomena is attributed to the higher field induced oxidation of the 15 V which results thicker oxide film formation.

The surface (anode) reactions can be in general described as:

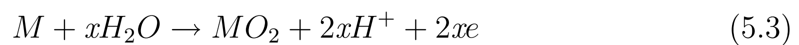

$$M + xH_2O \rightarrow MO_2 + 2xH^+ + 2xe \quad (5.3)$$

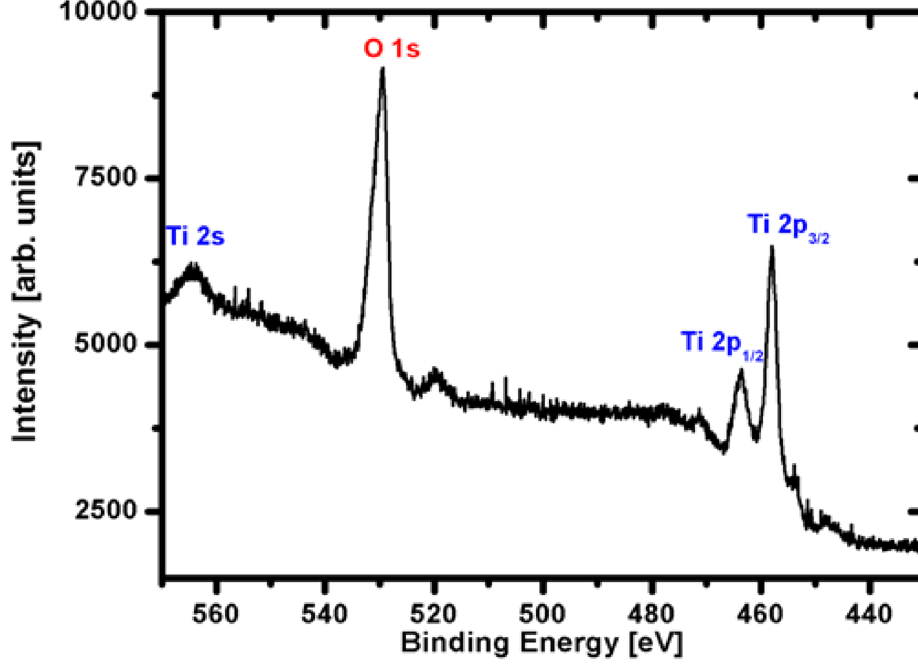

Figure 5.15: *x-ray photo spectroscopy (XPS) analysis of the* 50 *nm Ti film after anodization which reveals the formation of* TiO_2.

$$2H_2O \rightarrow O_2 + 4H^+ + 4e \tag{5.4}$$

where M is the surface material (e.g. Si, Ti etc.) and x is an oxidation number. For Ti surfaces, M is Ti and x is 2. Tip (cathode) reaction:

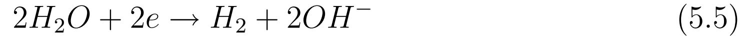

$$2H_2O + 2e \rightarrow H_2 + 2OH^- \tag{5.5}$$

To ensure the formation of TiO_2, film characterization was done. Figure 5.15 shows the analysis of the anodized film by x-ray photo spectroscopy (XPS). This was done on the 50 nm Ti film right after anodization process and it confirms the formation of the TiO_2.

Similar to the technique used for the Ti film, the anodization of polycrystalline nanowires of 70 nm thickness was done. To place the water droplet on the nanowire area of the sample, the contact angle measuring device integrated with CCD camera was used as shown in Figure 5.16 (a). Here, the contact angle needle was used for two purposes: to place the water droplet and as a cathode.

Figure 5.16 (b) shows the schematic representation of the anodization process.

As soon as the bias voltage was applied, a faradaic current expected to flow

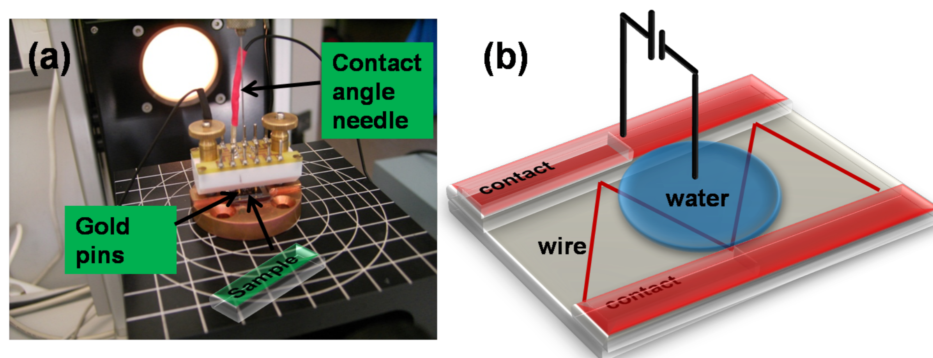

Figure 5.16: *Photo of the contact angle measuring device used for placing the water droplet(a), and the sketch featuring where the water droplet was placed (b).*

through the contact needle-nanowire junction as a result of the electrochemical reactions (see equations 5.3, 5.4 and 5.5). Since the nano-oxidation process utilizes a water meniscus, the process strongly depends on the amount of adsorbed water and, therefore, the atmospheric humidity. During the anodization process, two voltage sources were used: one for the anodization (referred as anodization voltage) and the second for current measurement through the wire during anodization process. The latter helps to find the optimal (desired) current. Hence, finding the "right" current value was done *in situ* by controlling the current measured through the nanowire during oxidation. This helps to avoid the complete anodization of the nanowire which was not the aim of the experiment. The higher the anodization voltage and the longer the anodization time, the thicker the oxide and the more insulating the wire will be due to its oxide shell. Figure 5.17 (a) shows the rapid decrease in current through the nanowire during the anodization process. A 10 V anodization voltage between the cathode (contact needle) and anode (nanowire), and a 0.5 V bias voltage at both ends of the nanowire were used. After certain anodization time, the current becomes constant. This phenomenon usually occurs when the oxide thickness reaches at critical value where further oxide growth is imminent. The oxide formation can affect the conductance of the nanowire in two ways either by narrowing conduction channel

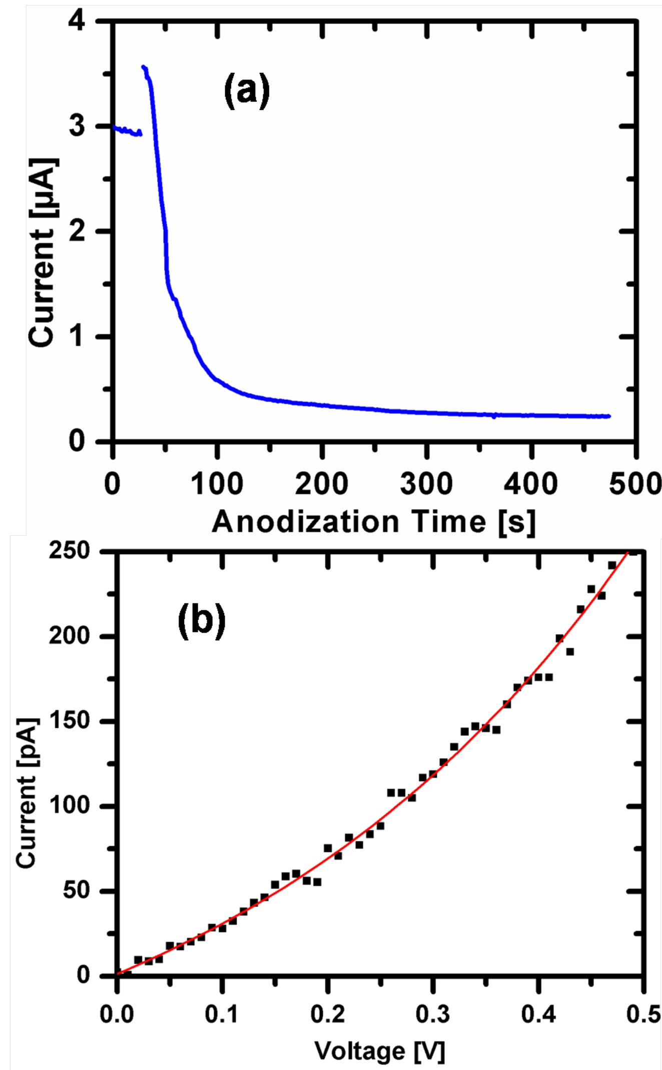

Figure 5.17: *The current measured through the Ti nanowire per time at* 10 *V anodization voltage (a) and the I-V characteristics of the Ti nanowire after anodizing with a voltage of* 10 *V for a period of* 5 *minutes (b).*

(minimizing the transverse grain size) or by forming oxide barrier between the grains which is accompanied by a resistance increase. Figure 5.17 (b) shows the I-V characteristics the Ti nanowire after anodizing for 5 minutes at anodization voltage of 10 V. Initially, the nanowire showed an ohmic behavior with resistance of 7.1 MΩ. However, after anodization the I-V curve shows a non-ohmic behavior.

Various current-voltage measurements were also taken and analyzed for different anodized samples. Figure 5.18 (a) shows the change in resistance of the Ti nanowire at different anodization voltage for the same anodization time (about 1 minute). The anodization voltage was increased in a 0.4 step up to 3 V. The resistance of the wire increases upon increasing the anodization voltage. Figure 5.18 (b) also shows the conductance change for the corresponding anodization voltage. The higher the anodization voltage the lesser the conductance of the wire for the same anodization time.

In macroscale anodization of metals, it is well-known that the thickness of the anodic oxide is determined by an applied sample bias vo1tage. Similar to the nanoscale oxidation observed here in both thin films and nanowires, the voltage plays a role in controlling the ultimate thickness of the oxide film. However, the determination of the absolute thickness of the anodic oxide formed in nanowires prepared by the method mentioned here was difficult to measure.

Further variable temperature measurement shows a non-ohmic behaviour of the anodized Ti-TiO_2 core shell nanowire. Figure 5.19 (a) shows the current measured through the nanowire upon increasing temperature. The nanowires have the nominal thickness of 50 nm and anodized at the voltage of 10 V for 5 minutes. The current measured shows a semiconducting nature of the nanowire. Figure 5.19 (b) shows the I-V characteristics at different temperatures. The conductance of the nanowire increases upon increasing the temperature which is unlike to its bulk counter parts where the conductance decreases due to phonon scattering.

For further electrical characterization of the anodized Ti nanowires at different temperature, 70 nm nominal thickness of Ti nanowires were prepared and then anodized at 10 V for 5 minutes. Figure 5.20 shows the non-linear I-V curves measured at different temperature: from room temperature up to 16 K. The conductance appears to decrease as the temperature decreases, which could be attributed to the confinement of the Ti-TiO_2 core shell nanowire and the electron localization due to disorder nature of the polycrystalline nanowires. Furthermore, these conductance changes were observed at a certain bias voltage (about $0.15V$) which shows a typical Coulomb blockade phenomenon. This phenomenon typically occurs due to small capacitance of the multiple metal-Insulator-metal (Ti-TiO_2-Ti) tunnel junctions which suppresses the electron tunneling and the quantized charge of electrons between the grains which can be observed at both

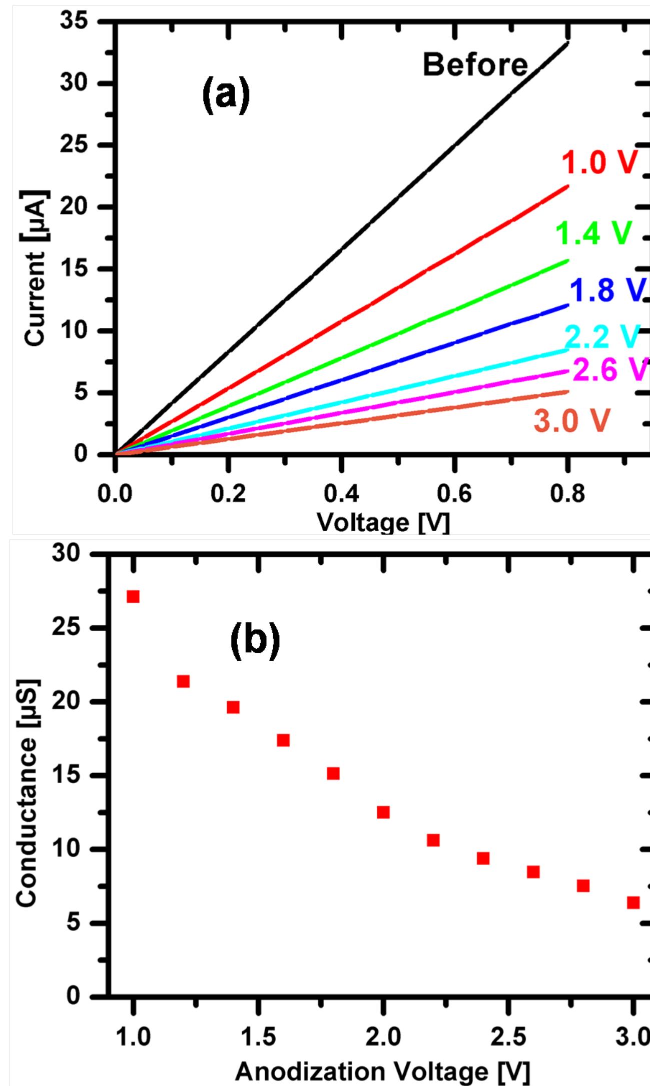

Figure 5.18: *The I-V characteristics of the Ti nanowire at different anodization voltage (a), and the change in conductance of the nanowire at various anodization voltage (b)*

room [84] and low temperatures [85]. When the charging energy associated with a transfer of one electron, $E_C = e^2/2C$ where C is a capacitance, is large compared with the available thermal energy, kT, the transport properties of the system become strongly influenced by the discrete nature of the electron charge. Single-electron devices, in which one-electron charging can be controlled by using Coulomb-blockade effect, have attracted much attention. Hence, its effect on memory devices [86] and transistors [87] at room temperature had been reported.

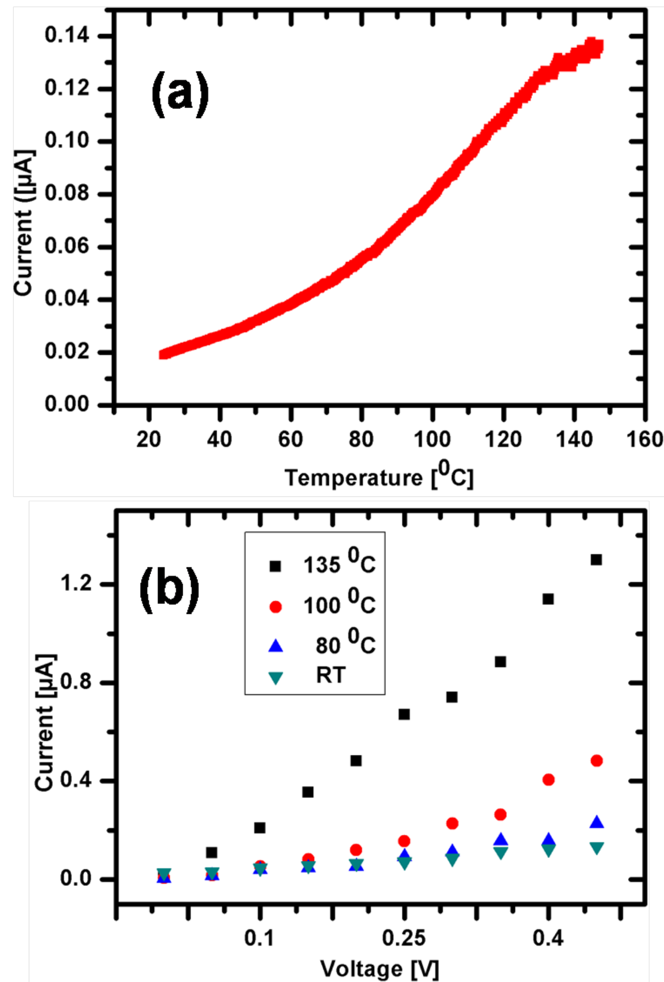

Figure 5.19: *The temperature dependence of the current measured through the Ti-TiO_2 core shell nanowire measured at constant 0.2 V (a), and the current-Voltage characteristics of the core shell nanowire at different temperatures(b)*

5.2.1.4 Nanowire-based Gas Sensors Device

Nanostructure based sensors are one of the great achievement of nanotechnology. These smallest dimensional structures play a key role on detecting biological and chemical species, and posses extremely high sensitivity, real-time detection abilities and low power consumption [88]. Because of their high surface-to-volume

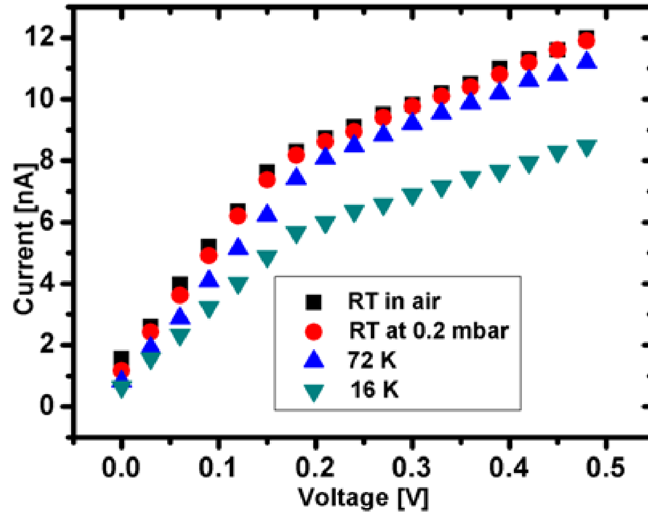

Figure 5.20: *The I-V measurement of the Ti-*TiO_2 *core shell nanowire at room and low temperatures.*

ratio and tunable electron transport (quantum confinement), their electrical properties can be affected by a small perturbation upon exposure to analyte molecules. Among these nanostructures, nanowires, one dimensional nanoscale materials, are one of the most promising materials for detection of various species in small concentration. Therefore, they have been used for the detection of various chemical and biological species such as ethanol [89], DNA [90], glucose [91], cholesterol [92] etc.

Pd nanostructures including nanowires [88, 93, 94], mesowires [95], nanotubes [96] and other one dimensional structures such as carbon nanotubes [97], titania nanotubes [98] etc. have been used for hydrogen gas sensors. The polycrystalline nature of the nanowires synthesized by the thin film fractured approach (discussed in section 5.1) consist of nanoscopic gaps. These enable them to have a better sensitivity for different chemical species upon exposure due to relatively high diffusion along the grain boundaries. During hydrogen exposure, two different resistance (conductance) response mechanisms were observed as shown in Figure 5.21 (a) and (b). Figure 5.21 (a) shows the first observed response of the nanowires while exposed to small concentration of hydrogen. This experiment was done under ambient condition and in an open beaker. The observed decrease in the resistance could be a result of Palladium hydrate formation upon hydrogen

adsorption. When the Pd nanowires are exposed to hydrogen molecules, the hydrogen molecules will be adsorbed on to the surface. The adsorbed molecules are then dissociated into the octahedral interstitial sites along the grain boundary [99], and react with the Pd atoms to form palladium hydride (PdH_x) [93–95] of α and β phases, which are dependent upon the hydrogen concentration [100]. These phenomenon decreases the intergrain distance in the nanowire, resulting the swelling of the Pd grains due to hydrogen absorption, therefore the nanowire resistance decreases accordingly (shown in Figure 5.21 (a)). On the other hand, the hydrogen adsorption process could also leads to an increase of resistivity because of the additional electron scattering on such impurities. Even though, the expansion of Pd lattice induces slight enlargement in the nanowire diameter which occurs due to the formation of PdH_x phase , the overall conductance tends to decrease. Figure 5.21 (b) shows this decrease in current (increase in resistance) upon exposure to a forming gas (10% hydrogen and 90% nitrogen). In both cases 50 nm nominal thickness of Pd nanowires were used. Its worth to mention that the Pd response (either increase or decrease in resistance) also depends on the concentration of the hydrogen. Therefore, the overall response of the nanowires upon hydrogen exposure is the resultant (superposition) of these mechanisms.

Bulk Au is well known to posses chemically inertness and low reactivity on its surface. This properties made Au the most valuable and desirable metal in modern history. However, Au nanostructures have shown strongly reactive nature. These remarkable properties could originate from strongly modified electronic structure of Au nanograins and nanostructures as their size and/or dimensionality are reduced [101, 102].

Figure 5.22 shows the observed decrement in resistance of the Au polycrystalline nanowire upon hydrogen exposure. The decrease in resistance could be attributed to the adsorption of the hydrogen molecule resulting in the formation of fractionally conducting bridges across the gaps between the grains in the nanowire [103]. This open beaker experiment test of the 50 nm nominal thickness nanowire was able to show that the hydrogen presence was able to be detected. However, for more deep understanding of the mechanisms, further experiments should be done. Regardless, the few-process step devices, fabricated in this work, show the potential of the fracture approach: nanowires could be integrated as functional parts in silicon-based microchips.

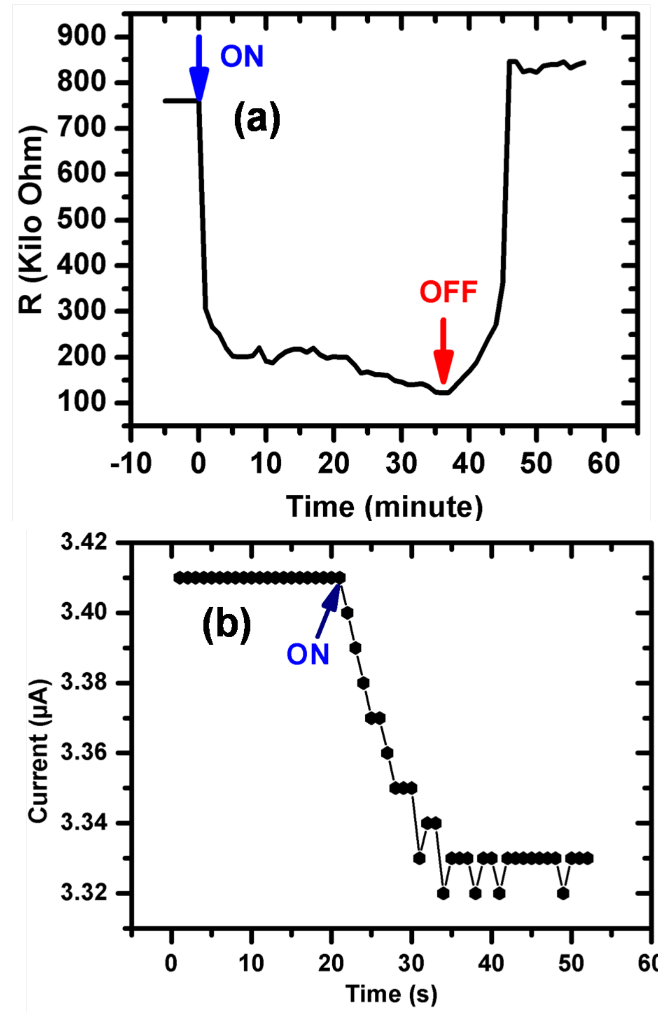

Figure 5.21: *The resistance change of Pd polycrystalline nanowires per time upon hydrogen exposure (a) and current vesus time plot for the same type of nanowires in* 10% *hydrogen gas (b).*

Furthermore, the 50 nm nominal thickness intrinsic ZnO nanowire prepared by sputter deposition of ZnO on thin film cracks and successive mask lift-off , was used for ozone sensing. This sensing test was done in collaboration with Dr. V. Cimalla (Fraunhofer Institut für Angewandte Festkörperphysik,Freiburg). Figure 5.23 shows the ozone sensitivity of the nanowires which exhibits a fast and a high switchability upon exposure. This ozone sensitivity test was done based on two mechanisms: ultraviolet (UV) (intensity = 4 mW/cm^2) photoreduction and subsequent ozone reoxidation of zinc oxide as a fully reversible process which can

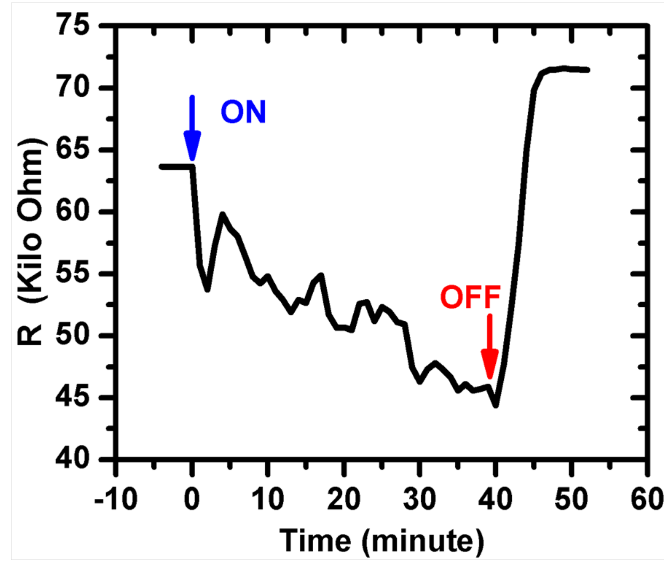

Figure 5.22: *Response of Au polycrystalline nanowires upon exposure to hydrogen gas.*

be repeated many times. The UV photoreduction results a decrease in resistance (shown by green arrow in Figure 5.23) which is attributed to the absorption of photons with energy higher than the energy band gap of the ZnO that lead to the generation of electron-hole pairs by light absorption [104]. Furthermore, oxygen is desorbed from the surface of the nanowire leading to creation of free electrons [105, 106]. The UV light irradiation whose associated energy is higher than the bonding energy between Zinc and oxygen leads to oxygen release from the nanowire in the gaseous form, leaving behind two valence electrons in the vacant site. If both electrons remain in the vacancy, the neutrality charge is preserved and the vacancy has 0 effective charges. If one or both of the localized electrons are excited and transferred away from the vacancy, the vacancy is left with an effective positive charge. The charged oxygen vacancy (singly or doubly ionized) becomes an electron- trapping site where one or two electrons can be made available for conduction. The formation of doubly charged oxygen vacancies can be described by the defect (equation 5.6 - 5.8) applied to ZnO when exposed to UV light [107].

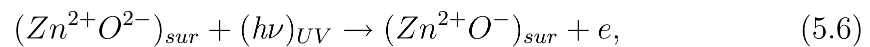

$$(Zn^{2+}O^{2-})_{sur} + (h\nu)_{UV} \rightarrow (Zn^{2+}O^{-})_{sur} + e, \tag{5.6}$$

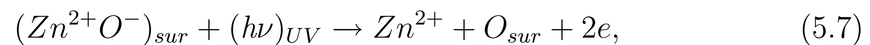

$$(Zn^{2+}O^{-})_{sur} + (h\nu)_{UV} \rightarrow Zn^{2+} + O_{sur} + 2e, \tag{5.7}$$

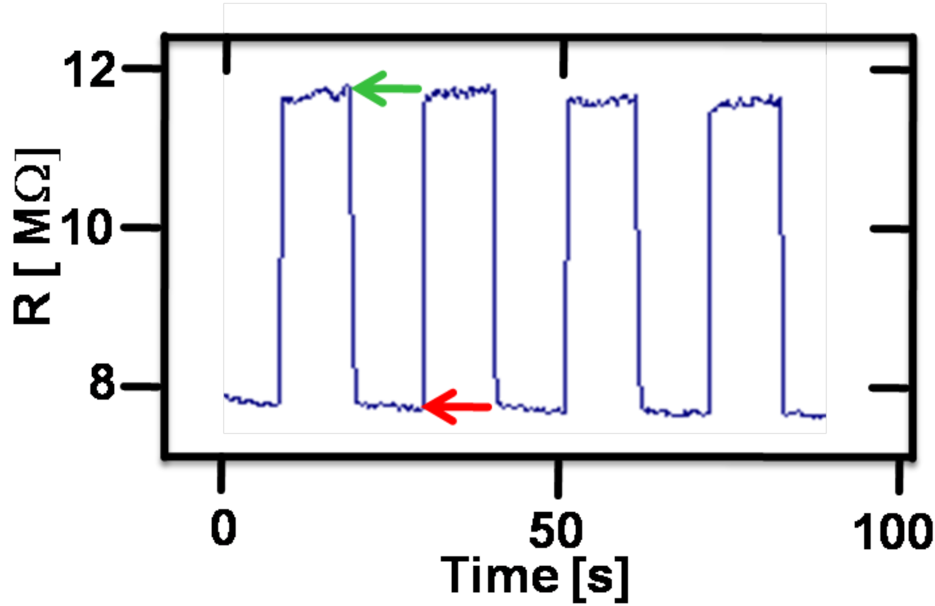

Figure 5.23: *The resistance response of ZnO nanowires upon ozone exposure. The green and red arrows represent the UV photoreduction and subsequent ozone reoxidation of zinc oxide nanowire, respectively.*

$$2O_{sur} \rightarrow O_2(g) \tag{5.8}$$

The subsequent oxidation in ozone (shown in red arrow in Figure 5.23) leads to annihilation of the charged oxygen vacancies by incorporation of oxygen into the nanowire by surface recombination as described in equation 5.9.

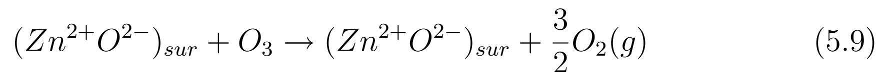

$$(Zn^{2+}O^{2-})_{sur} + O_3 \rightarrow (Zn^{2+}O^{2-})_{sur} + \frac{3}{2}O_2(g) \tag{5.9}$$

Thus, the charge carrier concentration decreases drastically which is accompanied by a drastic increase in resistance as shown in Figure 5.23. The ozone sensitivity depends on the size of the grains [106]. When the grain size decreases, the area of grain boundaries will increase. Therefore, the absorption and desorption of atoms from the surface has a much larger influence on the conductivity because the depletion layer caused by trapped charge carriers occupies a large fraction of the grain surface/volume. Consequently, the conductivity changes observed during UV irradiation and re-oxidation of the films are strongly dependent on surface morphology and type of contaminants incorporated in surface states.

5.3 Conclusion

In this chapter, the synthesis of horizontally aligned nanowires on conventionally fabricated silicon microchips based on a fracture approach is demonstrated. Furthermore, the basic electrical properties of these nanowires are examined and discussed, showing their suitability for applications. Different patterns of photoresist on silicon were treated to yield desirable and reproducible cracks. The fabrication of well-patterned cracks was successfully achieved by employing both bow-tie and a strip photoresist geometries. The microstructuring process was done by e-beam and conventional lithography for the bow-tie and strip shapes, respectively. For the simpler rectangular strip, it was observed that the strip dimensions play an important role in yielding cracks patterns. Therefore, among the stripes investigated, those with 10 μm width, 200 μm length, and 560-nm height showed ”zig-zag” pattern cracks with good reproducibility. This fracture approach allowed for the synthesis of different types of nanowire (such as Au, Ti, Ni, Pd, ZnO, Pt, etc.) after metal filling and removal of the excessive nanowire materials and remaining resist.

To investigate the suitability of these nanowires in devices, their conductivity and stability in an electric field was studied and compared to mesowires. Under ambient conditions, in the temperature range of (300 - 363) K, the nanowires showed a small increase in resistance, mainly due to hopping process. Lower-temperature measurements also showed completely different behavior. Unlike their bulk counterpart, their resistance decreases while temperature is increased. The conductivity through the nanowire in this temperature regime was found to be hopping assisted and was fitted to a both variable-range and power law hopping model for Ni and Au nanowires, respectively. In contrast, the resistance of the mesowires exhibits almost total stability in the temperature range of $(160 - 270)$ K. This stability could be a combination of two different conductivity mechanisms; hopping-assisted and bulk conductivity at relatively lower and higher temperature, respectively. The oxidization properties of Ni nanowires under different conditions were also studied. It was shown that field-driven oxidation occurred much more quickly than native oxidation. Field-induced oxidation can be observed in many electronic devices, which can also affect performance of

the nanowire integrated devices.

The local anodization of Ti nanowires based on electrochemical method was discussed. Highly purified deionized water meniscus as potential oxygen source was used. This helps to prevent any contamination of the nanowire during anodization process. The influence of different anodization voltage and anodization time at both the Ti nanowire and film were investigated. For instance, the rate of current decrease in thinner films was higher than thicker films during anodization process. This method provides an opportunity on fabrication of metal-metal oxide core shell nanowires in a simple and in well integrated system.

6 Synthesis and Characterization of Vertical Nanowires

One of the most attractive classes of materials for functional devices are semiconductors. Among these materials, zinc oxide (ZnO) is an outstanding semiconductor having a direct wide band gap energy of 3.37 eV and a large excitonic binding energy (60 meV) at room temperature. It's excitonic binding energy is much higher than the thermal energy at room temperature (26 meV) compared to other materials such as ZnSe (22 meV), ZnS (40 meV), and GaN (25 meV). Due to their wide range of applications, various techniques have been developed for the synthesis of functional semiconductor nanostructures including Vapor-Liquid-Solid (VLS) [9, 108] based, direct oxidation process [109], selective-area metalorganic vapor phase epitaxy technique [110–112] and others [113] etc. However, the main challenge in the usability of the synthesized functional nanostructures in electrical devices like gas-, photo- sensors etc., depends critically on the ability to form quality contacts and junctions. One of the solution to this problem is addressed in this part of the thesis.

This chapter discusses the synthesis and characterization of functional ZnO nanostructures based on two different techniques. Therefore, it is divided into two broad sections with respect to the technique used for the synthesis. Section one deals with the nanostructure synthesis by VLS technique. Under this section, both the structural and the morphological studies as well as the observed electrical properties of the as-synthesized ZnO nanostructures are presented. Whereas, the second section of the chapter focuses on the direct metal oxidation technique used for the synthesis of morphologically different ZnO nanostructures. The subsections are devoted for both the characterization and discussion of their corresponding electrical and sensoric properties of the nanostructures. Their detail analysis such as morphology, composition etc. were thoroughly investigated by

various characterization techniques including high resolution transmission electron microscopy (HRTEM), scanning electron microscopy (SEM) and *x*-ray photoelectron spectroscopy (XPS).
Generally, this chapter is devoted for the discussion of a simple, bio-safe, inexpensive, synthesis of functional ZnO nanostructures which are integrated into device in relatively simple steps.

6.1 Synthesis and Characterization of ZnO Nanosail

The catalyst-based VLS growth of vertical nanowires is a wide spread and very efficient technique [9, 108] for many semiconductors (including Si, III-V and II-VI compounds). Different catalysts such as tin (Sn) [114, 115], copper (Cu) [116] and Au [9, 117, 118] have been used for the growth of 1 D ZnO structures. The grown morphologies include nanowires [108, 119], -spirals [120] -belts [121], -combs [119], -cantilever [122] or -sails [123] which exhibit a high surface to volume ratios and superior mechanical stability making them ideal candidates for sensors [124], field effect devices or switches [125]. Also, an alignment of these esthetically pleasing structures is possible by combining the VLS growth with conventional microstructuring techniques [126, 127], which gives a well determined starting point for the subsequent VLS growth. However, forming contacts with the VLS grown structures to utilize them in a device is still tedious, because either the substrate material has to be the same like the VLS material or a laborious procedure has to be used. Such bridges between two contacts were fabricated from several semiconductors of ,e.g., GaAs, Si, GaN or ZnO. Typically this requires a careful process control and a large amount of process steps [112, 128–130]. Nevertheless, the great potential of these structures has been already demonstrated, e.g., as bio sensors, but requires manual and individual contacting by e-beam lithography and focused ion beam techniques [131].
In this part of the chapter, the contact formation in VLS growth by simply using the ability of individual crystals to interpenetrate each other in a self organized manner during the straight forward growth is presented. It was carried out by growing VLS structures directly on two neighboring Au circuit paths of a microchip; bridges over predefined gaps were formed by interpenetrations of the grown nanostructures. No special substrate has to be used in order to create

these bridges. By controlling the width and distance of the gap on the conventionally microstructured contact lines or the growth time, the density of the gap bridging intersecting nanostructures can be controlled in order to achieve a massively parallel set of intersecting nanowires.

6.1.1 Experimental Details

The synthesis of the zinc oxide (ZnO) nanostructures was done in collaboration with the group of Prof. Dr. C. Ronning (Physikalisches Institut, University of Göttingen). The sample preparation process consists of two major steps. First, the sputter deposition of Au on a microstructured photoresist film (see Figure 5.2 in chapter 5) on silicon substrates (76 mm-diameter, p-doped, $1-10$ Ωcm resistivity, 380 μm thick, $\langle 100 \rangle$ oriented and coated with 100 nm thick thermally grown SiO_2). The same type of microstructured photoresist film/substrate system was used for both the horizontal (see Chapter 5) and vertical nanowires. The microstructure pattering was done by using conventional photo-lithography. For better adhesion of Au on the substrate, about 3 nm of Ti was sputter deposited prior to the Au film formation to ensure that the deposited Au will not be removed during resist removing process. This process of removing the resist, to obtain the Au circuit, was done by soaking into acetone and using ultrasonic bath (BANDELIN, Sonorex, frequency - 35 Khz). Here, the Au circuits are used for two purposes : as a catalyst and electrical contact during and after synthesis, respectively. Both the Au film and the adhesion promoter, Ti, were deposited using argon ions at a pressure of about 3.0×10^{-3} mbar (with a base pressure of 8.6×10^{-7} mbar) and at the rate of 1.2 and 0.5 Å/s, respectively. For the sake of film uniformity, sample rotation was used while depositing both Au and Ti. Figure 6.2 (a) shows the part of the 50 nm Au contacts right after the resist removing process.
The second step of the process is growing the nanostructure by a VLS technique [132, 133] on the already Au deposited silicon sample. This procedure starts with placing both the source material and the catalyst (Au) coated substrate in the furnace. Figure 6.2 (a) shows the optical image of the as-sputter deposited 50 nm thick Au film on a silicon substrate. The clean Au deposited sample were then

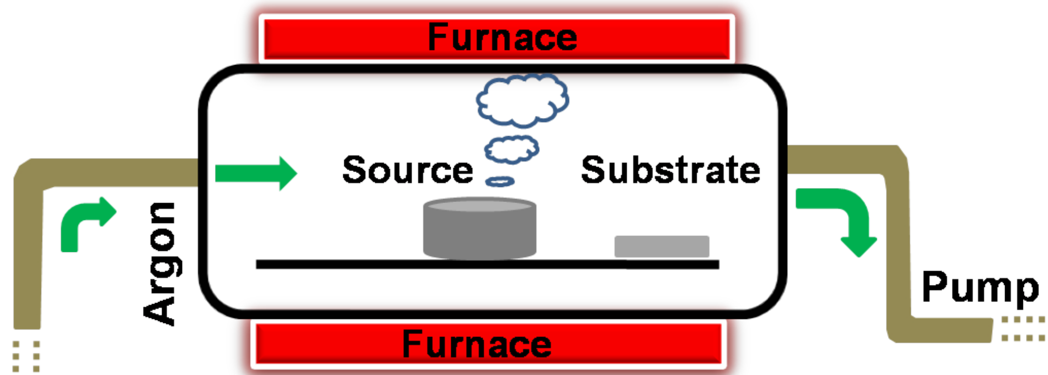

Figure 6.1: *Schematic diagram of the experimental set up used for the ZnO nanosail growth.*

placed at a position in the furnace with a sample temperature of about 1000 °C. And pure ZnO powders as source material were also put in an alumina boat and placed at the center of a tube furnace as schematically shown in Figure 6.1. The furnace was heated up to 1350 °C with a ramp of 190 °C per hour for 5 min. During the entire process an argon gas flow of 50 sccm (standard cubic centimeter per minute) with a system pressure of about 100 mbar was applied. The argon gas flow direction was adjusted to transport the ZnO vapor from source to substrate only at 1350 °C, but an opposite gas flow direction was applied during heating-up and cooling-down.

At about 1350 °C the ZnO vapor started to evaporate and was continuously carried out by the flow of argon to the already melted Au liquid droplets. The liquid Au droplet posses higher accommodation coefficient, it is therefore a predefined site for growth. Saturated growth ZnO in the Au liquid droplet will diffuse to and precipitate at the interface between the 100 nm silicondioxide layer and the melted Au. Continued precipitation or growth will separate the substrate and the liquid droplet. The sail-like nanostructure (denoted as nanosail in the following) will continue its growth at equilibrium temperature while the ZnO vapor continues to flow. The possible growth mechanism in a vapor-liquid-solid technique is discussed in chapter 2. The grown ZnO nanosails cover the whole Au area and bridges the gap between the Au contacts as shown in Figure 6.2 (b). The inset in Figure 6.2 (b) shows the interpenetration between the nanosails observed

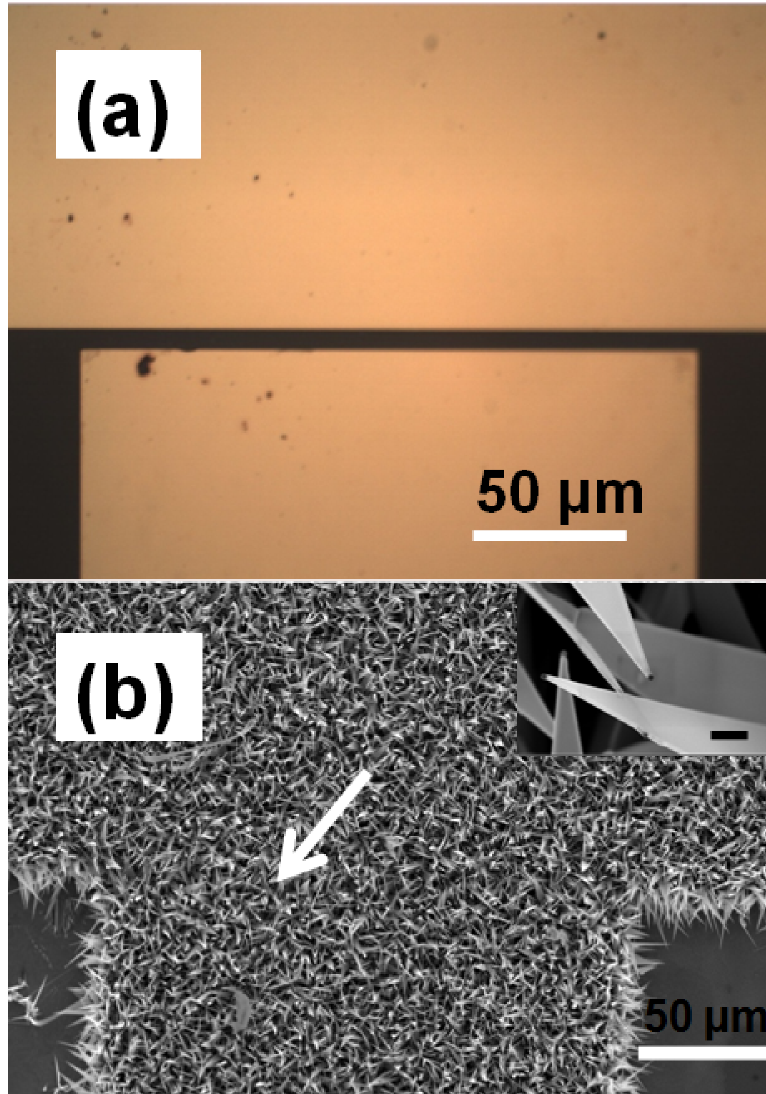

Figure 6.2: *The optical image of a* 10 μm *wide channel after* 50 *nm Au deposition (a)and scanning electron microscopy image after Zno nanosail growth (b). The gap between the contacts are bridged by the grown nanosails. The inset shows the interpenetration of nanosails.*

between the Au contacts. This bridging phenomena play a role on the functional properties of the nanosail integrated device formed.

For detailed investigation of the as-synthesized ZnO nanosails, they were scratched from an Au support and analyzed by high resolution transmission electron microscopy (HRTEM) with a Philips CM 30ST microscope (LaB_6 cathode, 300 kV, CS = 1.15 mm). Selected area electron diffraction (SAED) and precession

electron diffraction (PED) [134–137]) were carried out using a diaphragm which limited the diffraction to a circular area of 2500 Å in diameter. HRTEM micrographs (multislice formalism) were simulated with the EMS program package [138] (spread of defocus: 70 Å, illumination semiangle: 1.2 mrad). All images were evaluated (including Fourier filtering) with the programs Digital Micrograph 3.6.1 (Gatan) or Crisp (Calidris). Chemical analyses by EDX were performed with a Si/Li detector (Noran, Vantage System).

6.1.2 Result and Discussion

6.1.2.1 Characterization of ZnO Nanosails

The characterization of the as-synthesized ZnO nanosails enable careful and thorough investigations of composition, real structure and morphological studies of the nanosails. Figure 6.3 shows the SEM image of the nanosails grown on the Au contact pads. The grown ZnO nanosails bridges the 10 μm gap in between the contacts as shown in the dash line in Figure 6.3 (b). The inset in Figure 6.3 (c) shows the interpenetration of the nanosails which was observed in between the 10 μm gap. The high quality bridges by the interpenetrating nanosails in this way are the basis for the electrical and sensing properties of the nanosail-integrated device. The schematic representation in Figure 6.3 (d) shows how the interpenetrating nanosails appears after growth. The conductivity of the bridging nanosails was studied and presented in section 6.1.2.2.

Further more, the through TEM investigation (done in collaboration with Prof. Dr. Lorenz Kienle at CAU, Kiel) enables to obtain a detailed information about the ZnO nanosails. By taking into account the reference measurements performed on chemically pure ZnO, the equimolar ratio Zn:O and the absence of any contaminations was verified by STEM and nanoprobe EDX. The nanosails show uniform morphological attributes, which were described for nanobelts [139] in many conditions, namely that they grow along [01-10] of the wurtzite-type structure with top/bottom triangular surfaces parallel to the low energy (2-1-10) layers. The acute angle at the tip of the nanosails was determined to be close to 30^0. For zone axis orientation [2-1-10], one of the long edges of the triangle appears smooth on an atomic scale due to its parallel alignment to the growth direction. Hence, the

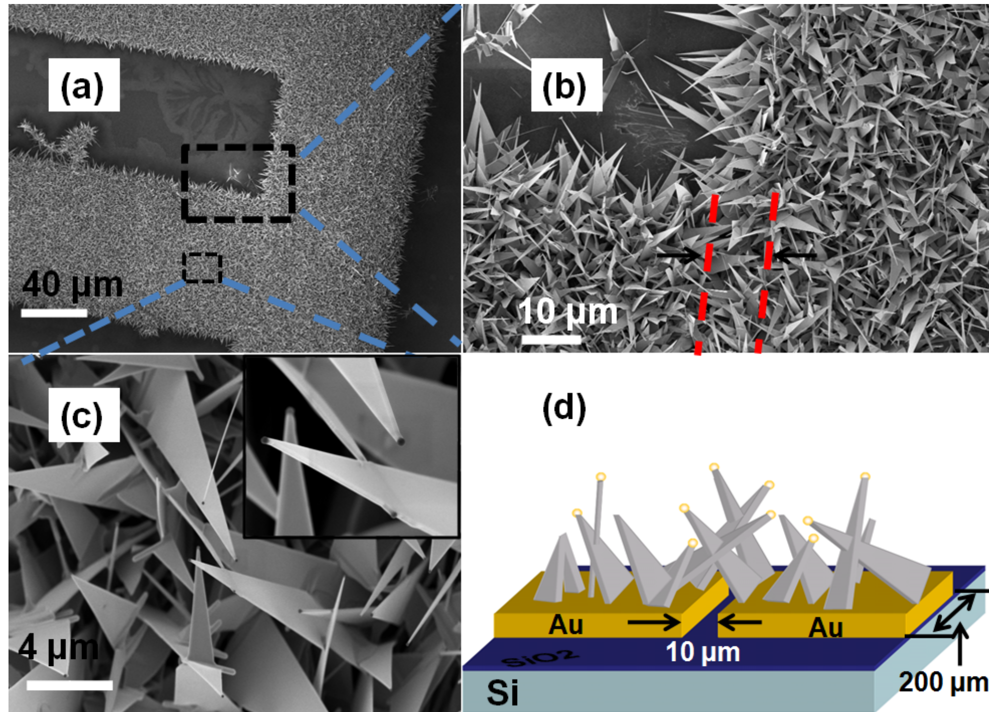

Figure 6.3: *The scanning electron microscopy image of the Au contacts after ZnO growth up on increasing magnification from (a) to (c). The inset in (c) shows the interpenetrating nanosails. The sketch shows the grown nanosails including the possible interpenetration which bridges the* 10 μm *gap between the contacts(d).*

nanosails are terminated on one side by (0001) layers, as shown in Figure 6.4 (a), while the opposite edge contains steps (see arrows in Figure 6.4 (a)) representing surface instabilities of the polar (0001) surface. The thickness of the nanosails appears uniform. The gold particle at the tip of the nanosails represents a twinned multi-domain single crystal consisting of consecutive (111) lamella separated at coherent boundaries. No preferred orientation of Au particle and ZnO nanosail was observed, including the minimum interface mismatch orientations with (0001) parallel to (111) [140, 141]. Actually, even orientations with strong mismatch, e. g., (0001) orthogonal to (111) produce well-aligned and flat interfaces with the corresponding precession electron diffraction (PED) pattern as shown in Figure 6.4 (b). All nanosails were fully crystalline up to the outermost edge and free of any crystal defects, like stacking faults. As demonstrated for zone axis [2-1-10] in Figure 6.4 (c), the high-resolution micrographs can be interpreted by

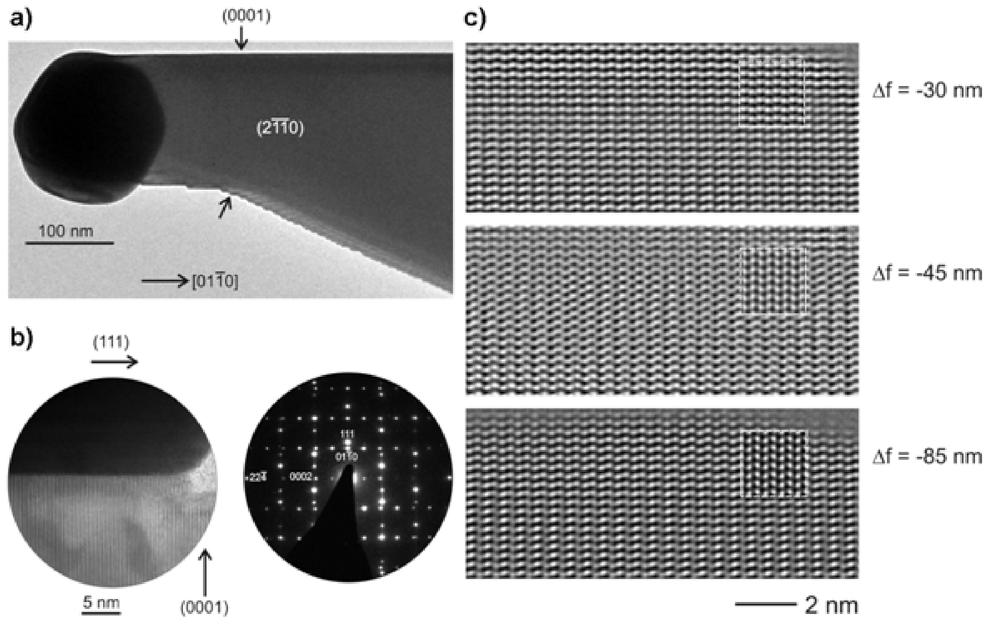

Figure 6.4: *TEM investigation of the nanosails structure: nanosails are terminated on one side by (0001) layers, while the opposite edge contains steps, see arrows (a), Bright-field high resolution micrograph near the interface Au / ZnO with corresponding PED pattern. (right, rotation corrected), all aligned in zone axis orientation [2-1-10] (b). Experimental and simulated HRTEM micrographs (inserted,* $t = 3.3$ *nm) for zone axis [2-1-10]. Here,* Δf *and* Δt *represents the change in focus and the specimen thickness, respectively (c).*

the inserted multislice simulations based on the wurtzite-type structure. For the change in focus (f = -45 nm), the imaging conditions of Scherzer focus are approximated, hence, the black dots represent the positions of the Zn and O atoms. As a rule, larger fragments of the specimen represent an aggregate of several nanosails fused by distinct types of interpenetration and intergrowth. Both phenomena could generally be described by the set of twin laws described in the past for ZnO nanostructures. In contrast to ZnO nanowires [142] and nanobelts [143] a bicrystalline morphology in a single nanosail was never observed, but twinning always includes several individuals. Such scenario reminds of self-assembled ZnO nanostructures, like octa-twin tetralegs [144], nanocombs [145]and others [146], however, the driving force for interpenetration seems dominant for the nanosails. One of the cases of interpenetration studied by HRTEM is shown in Figure 6.5 (a), for two nanosails with nearly rectangular orientation of the (0001) layers

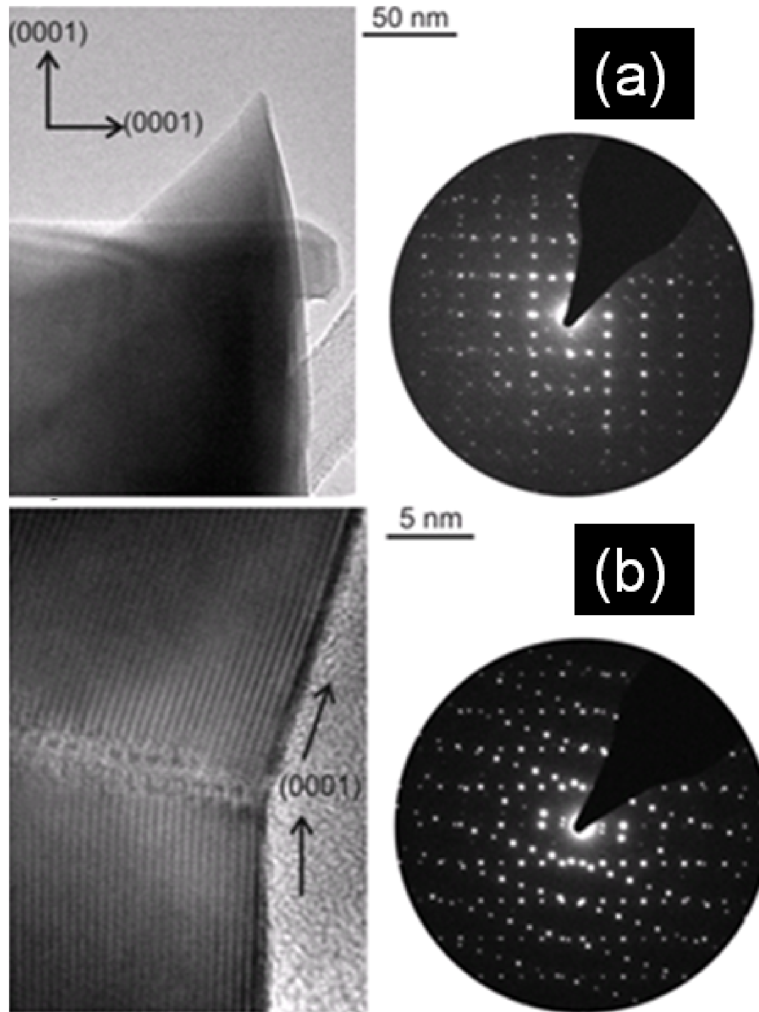

Figure 6.5: *Microscopic and electronic features of interpenetrated nanosails (a), and intergrowth (b) of two nanosails with PED patterns, common zone axis [2-1-10].*

according to coherent (10-1-2) twinning [147]. A non-merohedral twinning combining two nanosails at incoherent boundaries is shown in Figure 6.5 (b). In this case, the (0001) layers of two fused nanosails are rotated by 17.5^0 around [2-1-10], which represents the common zone axis of the individuals.

6.1.2.2 Electrical Properties Nanosails at Room- and Low-Temperature

The few step preparation of the circuit path and the nanosails emphasizes the advantage of the technique and makes it convenient for the analysis of the electrical properties. It turns out that a massive parallel connection of intersecting nanosails is preferable, as to less connections result in noise from individual defects and lead to non reproducible results. The reproducibility was verified by preparing two different density of nanosails which were synthesized by controlling the growth time. The electrical properties of the low and high density were then investigated. Figure 6.6 (a) shows the SEM micrograph of the as-synthesized low density nanosails. The I-V measurment of theses nanosails shows either no current or highly pronounced noise as shown in Figure 6.6 (b).

On the other hand, the high density nanosails shows highly reliable and reproduciable electrical properties, therefore further electrical analysis under different conditions is possible. Figure 6.7 (a) shows the I-V measurement of the high density nanosail-based device at room temperature with and without a bias gate field. Without the gate voltage, the single crystalline nanosails exhibit a typical non-linear behavior of two Schottky diodes in reverse series as schematically shown in Figure 6.7 (b), with a symmetrical characteristic around zero. With a gate field applied via the highly doped substrate used as bottom gate, the source-drain current through the nanosail device was measured. It is worth to mention that, the currents with a massive parallel connection were on the mA scale, which makes them very interesting for integration in conventional electronics.

The conductance of the high density ZnO nanosails was also influenced by temperature when it was measured at both low and room temperatures. Figure 6.8 shows the I-V characteristic comparison at 16 K and 300 K which exhibits an increase in the resistance of the nanosails at 16 K. Both temperature measurements were done at the pressure of 2 $mbar$. The change in resistance from room to low temperature can be attributed to the effect of charge carrier localization at lower temperature.

6.1.2.3 Nanosail-based UV- and Gas-Sensor Devices

The conductance of ZnO (with band gap 3.37 eV) nanostructures changes upon UV light exposure [148]. Figure 6.9 (a) shows the UV response of the synthesized

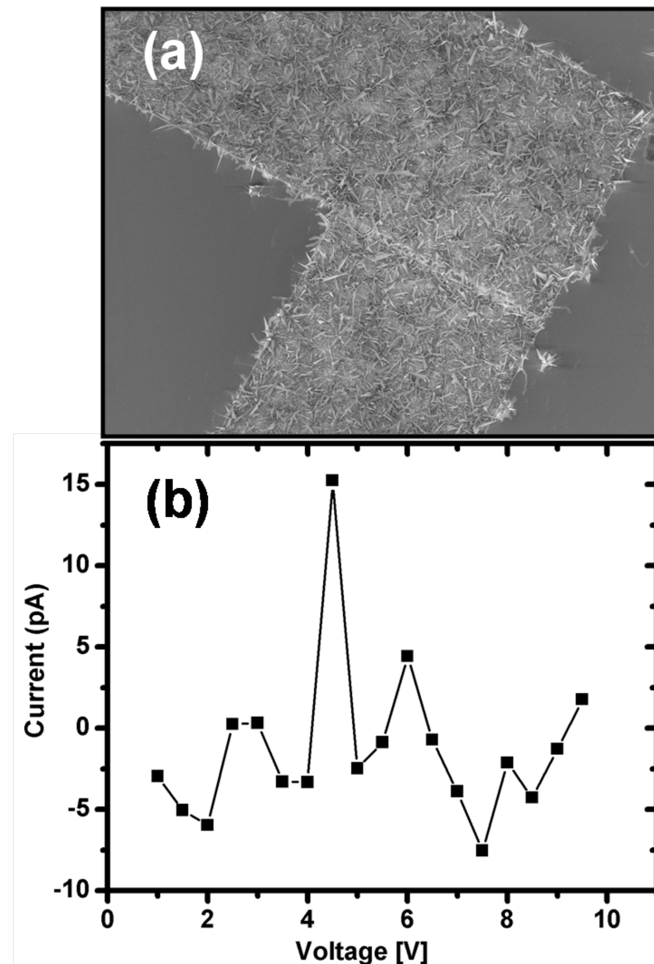

Figure 6.6: *The scanning electron microscopy image (a) and the I-V characteristics (b) of the low density ZnO nanosails. The I-V curve shows no current measured between the two Au contacts.*

ZnO nanosails which was measured at $6V$ bias voltage. The nanosail-integrated device was exposed to the UV light lamp (λ = 360 nm, UV spotlight H135, LABINO AB) at room temperature in ambient. The fast switching (change in conductance) was observed while the light was switched on and off in equal interval of time. When photons in higher energy (*e.g.*, UV light) falls on the ZnO nanosails, it leads to an increase of the electrical conductance. The photoconduction is mainly originated by the band-to-band electron-hole pair generation and the recombination mechanism swiftly contribute to recover the initial carrier concentration in the nanosails after the light is off. However, Figure 6.9 (a) shows the

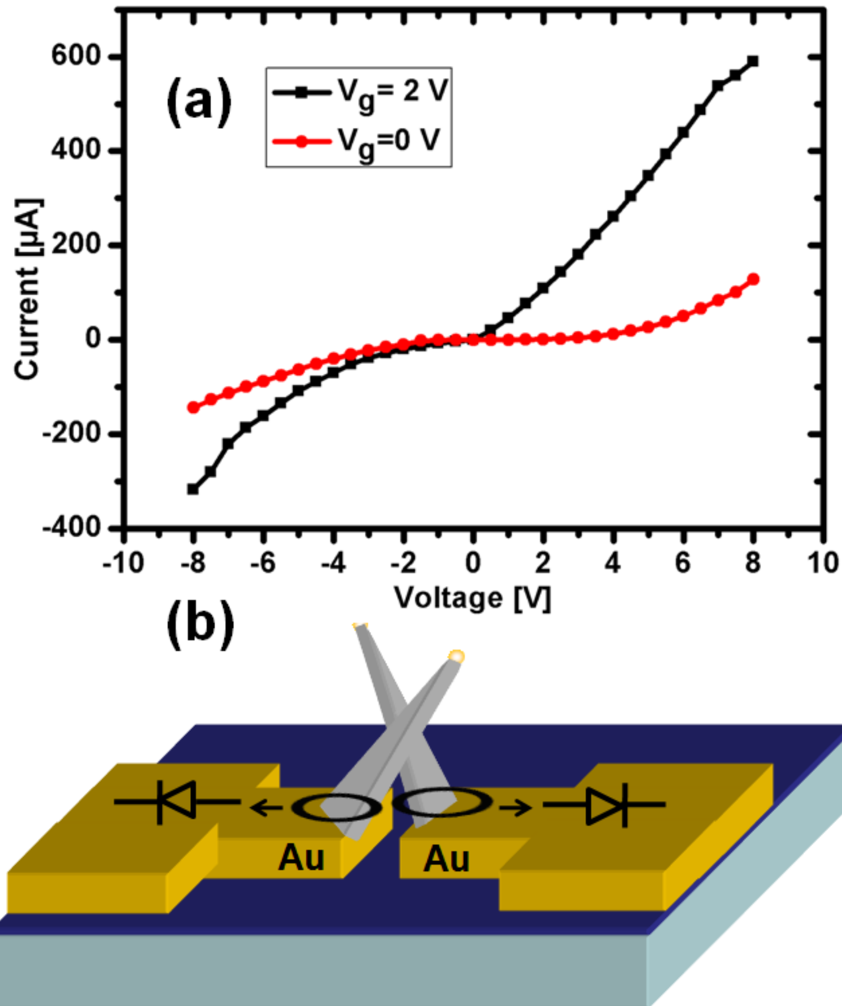

Figure 6.7: *The I-V characteristics of the ZnO nanosails at both* 0 *V and* 2 *V gate voltage(a), and the sketch showing the shottkydiode foramtion on the ZnO-Au contacts (b).*

initial current (taken as baseline) was not fully recovered after switching off the light. Various assumption have been given for this mechanism. The first assumption is based on the presence of intrinsic point defects which exhibit metastable charge states located between shallow and deep energy levels [149, 150]. According to this assumption oxygen vacancies can be excited to a metastable charged state after a structural relaxation. In these states, the recapture of the electrons is prevented by a thermally activated barrier [150]. The second assumption is based on the electron-hole separation related to the surface properties of the

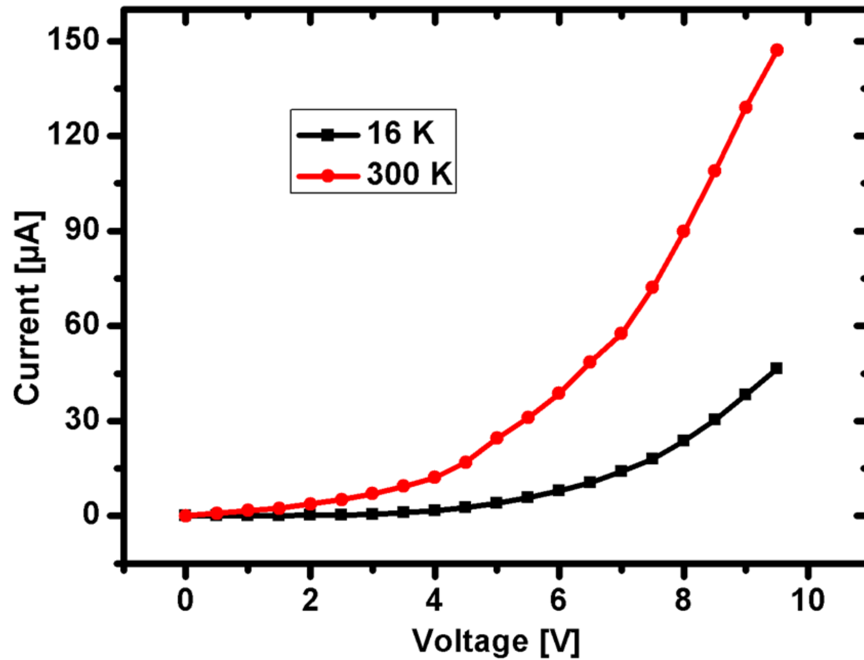

Figure 6.8: *The I-V characteristics of the high density ZnO nanosail which are integrated into device both at* 300 *and* 16 *K.*

metal oxides [151, 152]. This phenomenon is as a result of the adsorption of O_2 or OH molecule on to the nanosail surface [105]. This adsorption of O_2 molecules causes the built-in potential near the surface of the nanosail which separates the photogenerated pairs: holes accumulate at the outer and electrons remain in the inner part. This photogenerated effect prevents the recombination of a fraction of the pairs and results an increase in current after each cycle of UV exposure. Figure 6.9 (b) shows the UV- photoconductance comparison of the ZnO-nanosails under UV and in dark state. The resistance of the nanosails decreases characteristically upon the exposure of the UV-light which can be due to the migrations of the photo-generated holes to the surface and discharge the adsorbed oxygen ions through the electron-hole recombination process [105]. The photoresponse could also be attributed to the potential barrier lowering between the ZnO and the Au contact of the reverse biased diode. These basic electrical properties were demonstrated by using them as UV-light dependent resistor (UV-LDR). In addition, the oxygen chemisorption also plays a significant role on the sensitivity of ZnO nanostructures [153]. This UV-light sensitivity could be used for the fabri-

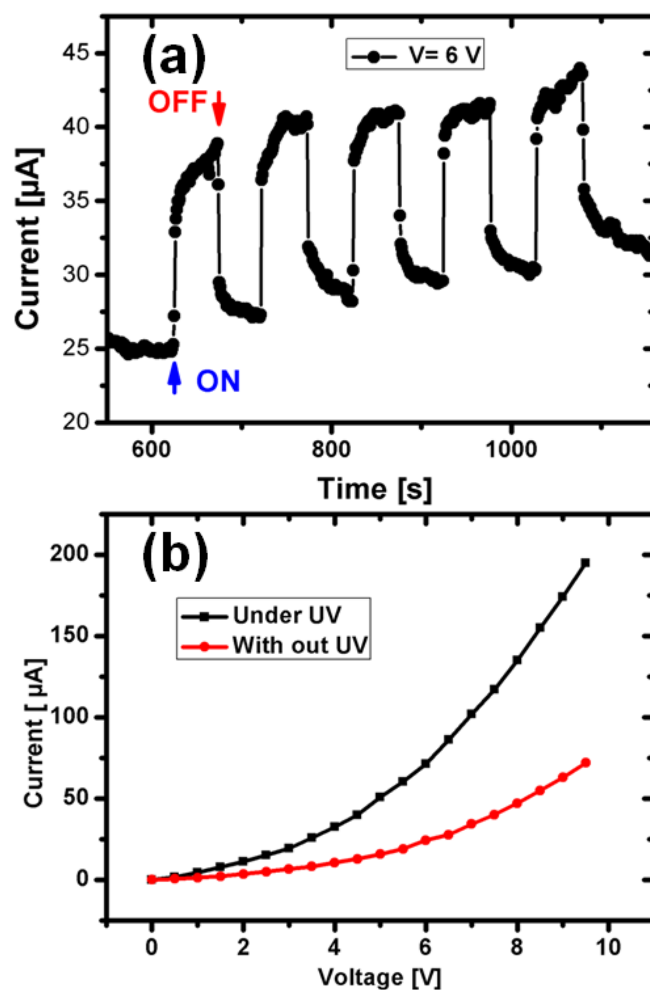

Figure 6.9: *The UV light response of the ZnO nanosails (a). The "ON" and "OFF" signs refer to the UV light exposure and dark states , respectively. The I-V characteristics comparison of the nanosails at both states (b).*

cation of optical switches or detectors [131, 154].

The large surface area of these nanosails and their environmentally friendly nature make them a candidate in various area of application including chemical, bio or medical sensing. Hydrogen detection based on nanostructures such as nanowires [39, 93] or nanorods [155] has been already investigated, where the chemisorption of reactive gases at the surface of a metal oxide (e.g ZnO) can increase the conductance of the material [156]. ZnO nanostructures are also one of the most promising candidates for detection of various gases such as carbonmonoxide (CO),

methane (CH_4), hydrogen (H_2), ethanol (CH_3CH_2OH), hydrosulfide (H_2S) etc. The sensing of these gases is based on the adsorption-desorption mechanism on the surface of the ZnO nanostructures. For instance, the hydrogen sensing mechanism can be explained on the basis of chemisorption of the hydrogen molecule on the ZnO nanosails. It produces a reversible change in the resistivity with the exchange of charges between H_2 and the ZnO surface leading to changes in the depletion length [157]. The oxygen vacancy in ZnO nanosails acts as an electron donor in ZnO to provide electrons to the conduction band of ZnO and makes ZnO nanostructures an n-type semiconductor [158]. Various studies have shown that the exposed surface of ZnO nanostructures adsorbs the oxygen molecules from the ambient gas components, which capture electrons from the conduction band and form O^{-1} as follows

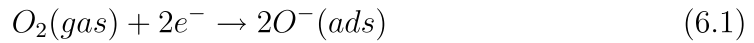

$$O_2(gas) + 2e^- \rightarrow 2O^-(ads) \tag{6.1}$$

Intuitively, a larger surface area provides more positions to adsorb oxygen molecules. Furthermore, a larger quantity of oxygen vacancy induces higher adsorptions of oxygen without lowering the expansion level of depletion layer for as-synthesized (undoped) ZnO nanstructures, which results in a further increase of the resistance of the sensors.
When the ZnO nanostructure based sensor is exposed to a reducing test gas such as hydrogen, its atoms react with these chemisorbed oxygen ions and produce H_2O molecules consuming chemisorbed oxygen from the surface by releasing electrons. The sensing mechanism for H_2 at room temperature can be represented by the following relation:

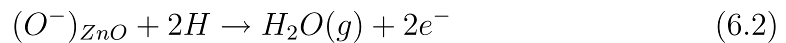

$$(O^-)_{ZnO} + 2H \rightarrow H_2O(g) + 2e^- \tag{6.2}$$

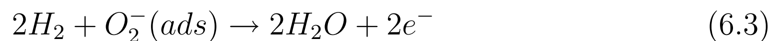

$$2H_2 + O_2^-(ads) \rightarrow 2H_2O + 2e^- \tag{6.3}$$

considering O^-_{ads} as the predominant adsorbed species on ZnO nanosail surface at room temperature [159]. As a result electrons will be released back to the conduction band and will contribute to current increase through the nanosail. This also results in a reduction of surface depletion region and increase conductance.

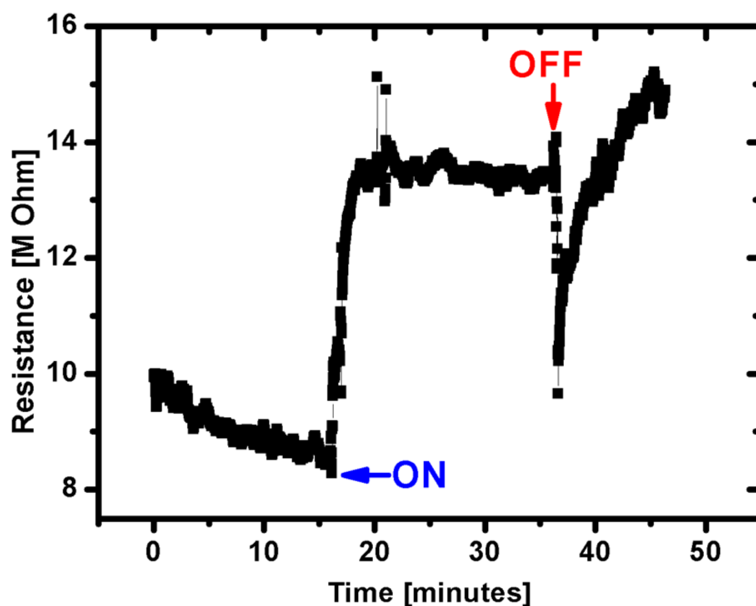

Figure 6.10: *The resistance response of ZnO nanosails to 10% hydrogen exposure.*

The reaction is exothermic in nature (1.8 $kcalmol^{-1}$) [160] and the molecular water desorbs quickly from the surface.
However, the response of ZnO nanosail integrated devices exhibits an increase in resistance upon the exposure of 10% H_2 in N_2 as shown in Figure 6.10. This measurment was carried out at room temperature while it was biased at 4 V . The decrease in conductance obtained here upon H_2 exposure is unlike to the explantion discussed above. This observed H_2 sensing mechanism is somehow complicated and need further understanding.

6.2 Synthesis and Characterization of ZnO Nanoseaurchins

This section of the chapter discusses the synthesis of the vertical nanowires without an additional catalyst material. The detailed characterization of this catalyst free ZnO nanostructure were also carried out by TEM, XPS and SEM techniques. The section is divided into different subsections which start by discussing about

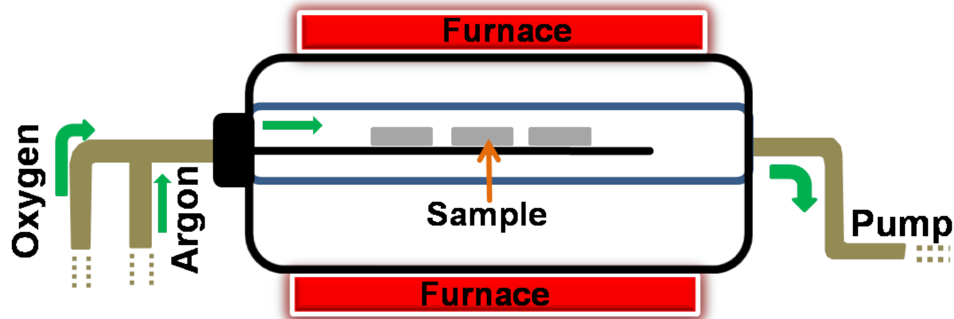

Figure 6.11: *The sketch shows the furnace used for the synthesis of sea-urchin-like ZnO nanostructures.*

the basic synthesis technique used, the structural and morphological analysis and finish with the analysis of their electrical properties.

6.2.1 Experimental Details

Unlike the VLS technique (discussed in section 6.1), the zinc oxidation based synthesis does not require a catalyst for growth of the nanostructure and can be done in a relatively low temperatures. This zinc oxidation was done in a horizontal vacuum furnace as shown in Figure 6.11 which consists of 30 cm long quartz tube. One side of the quartz tube is connected to two gas inlets (for both the carrier gas argon and the reactive gas oxygen (99.998% purity)) and the other side is connected to the rotary vacuum pump. Temperature control was done by integrated thermocouples. The synthesized ZnO nanostructures have a sea-urchin-like appearance which are composed a microscalled central core and nanowires as spikes(denoted as nanoseaurchins throughout the text).

The Zn metal powder from SIGMA ALDRICH (purity 99.995%, size < 150 μm) was mixed with ethanol for uniform distribution of the powder on a 1 cm x 1 cm silcon substrate (76 mm-diameter, $5 - 7$ Ωcm resistivity, 625 μm thick, $\langle 100 \rangle$). The uniformly dispersed and dried ZnO powder was then inserted into the furnace. The furnace was heated upto 600 °C at the rate of 20 °C/min after reaching a pressure of 30 mbar. For the success of the nanoseaurchins synthesis,

both the flow rate and the releasing time of the gasses were carefully controlled. The optimum flow rate for oxygen and argon was set at 60 and 40 normal liter per hour (Nl/hr), respectively. Both gases were introduced when the furnace temperature reaches at 600 °C and was kept for about three hours. Later the furnace was turned off to cool down slowly to room temperature.
The possible growth mechanism of the ZnO nanoseaurchins and nanowires is illustrated in Figure 6.12 and consists of two stages: nucleation and growth. When the Zn coated silicon (100) substrate is heated at 500 °C, the metal Zn powder (melting point = 419.53 °C) first starts melting and aggregating to form the micro-sized Zn droplets on the surface of the Si substrate as shown in Figure 6.12 (b). After the introduction of oxygen into the reaction chamber at 600 °C, the oxygen tends to react with the outer surface of the previously formed Zn droplets and form nanosized ZnO nuclei on the surface of these Zn droplets (Figure 6.12 (c)). As the aggregated Zn droplets become supersaturated, the liquid Zn reacts with oxygen and forms ZnO nuclei at the interface. These ZnO nuclei individually grow in the upper direction in the form of ZnO nanowires. The nuclei thus play a crucial role in the growth of ZnO nanowires, which grow until the Zn source is almost consumed. Therefore, from each zinc droplet there is an origination of several ZnO nanowires which leads to the formation of the nanoseaurchins. These structures are grown on the silicon substrate surface with a high density and cover large area of the substrate.

The morphology and structure analysis of the as-synthesized ZnO nanostructures were then characterized by different techniques as discussed in the next subsection.

6.2.2 Result and Discussion

6.2.2.1 Characterization of the ZnO Nanoseaurchins

The morphologies of as-synthesized ZnO nanoseaurchins on the silicon substrate were characterized by scanning electron microscopy. Figure 6.13 (a)-(c) shows the different microstructures including the microspheres and microbowls which were observed at various temperature regions. The various size of the microspheres seemingly have a solid Zn core. These different structures are the sites

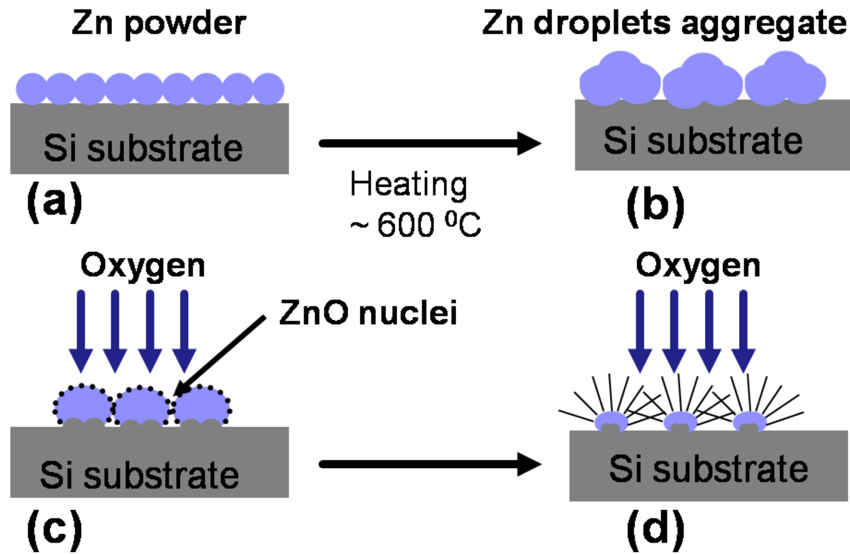

Figure 6.12: *The schematic illustration of the the nanoseaurchins growth process: the mixture of Zn powder and ethanol dispersed on Si substrate (a); formation of aggregated Zn droplets (b); formation of ZnO nuclei on the surface of Zn droplets (c); growth nanowires out of the droplets (d).*

where the nucleation and further growth of the nanostructures occurs. Figure 6.13 (d) shows the high density as-synthesized ZnO nanoseaurchins which consists of nanowires with various diameter and a length of several micrometer. The reduction in nanowire diameter projecting out were observed as shown in the inset of Figure 6.13 (d). Moreover, no branching was observed on the nanowires, which implies that the nanowires were grown from spontaneous nucleation.

The morphology and microstructure of the ZnO nanoseaurchins were further studied by TEM and HRTEM after selectively removing the nanowire by scratching. The detailed characterization of these nanostructures were done by Dr. Andriy Lotnyk in the group of Prof. Dr. Lorenz Kienle at CAU, Kiel. Figure 6.14 (a) shows the TEM bright-field image of a ZnO nanowire. The image shows that the nanowire consists of two areas. Figure 6.14 (b) presents a precision electron diffraction (PED) pattern taken from the ZnO nanowire shown in Figure 6.14 (a). Even though, the synthesis of the nanowires was done at a much lower temperature than the VLS technique discussed in section 6.1, the TEM and PED pattern studies reveals the nanowires are single crystalline. The pattern has three set of

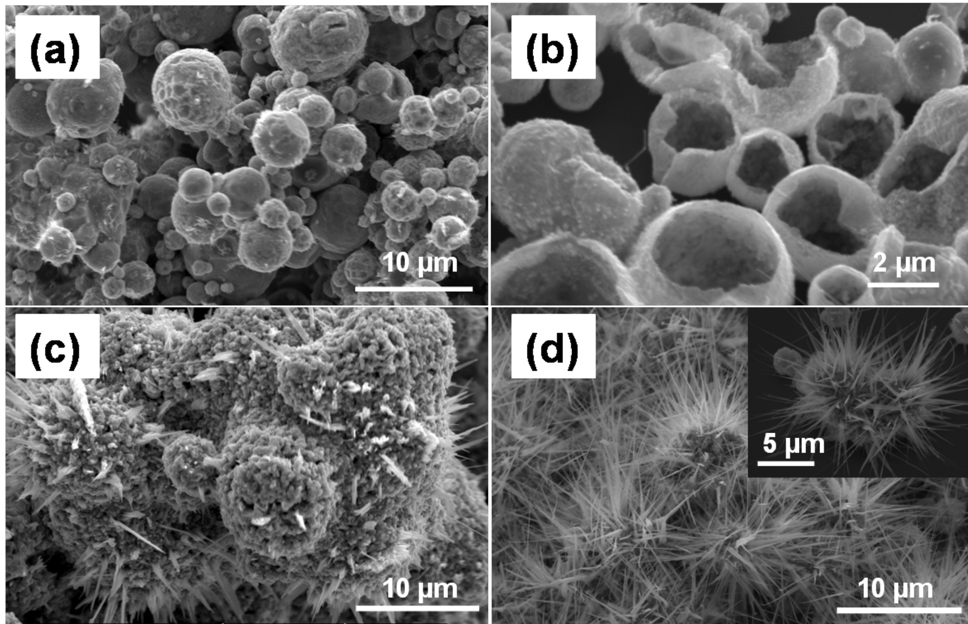

Figure 6.13: *The scanning electron microscopy of the ZnO nanoseaurchins at different stages. Microspheres (a) and microbowls shows the early stage of the synthesis. The melted and aggregated Zn powders and the as-synthesized ZnO nanoseaurchins are shown in (c) and (d), respectively. The inset in (d) shows the relatively high magnification of the nanoseaurchins.*

spots in viewing direction of ZnO. The TEM investigation of many others ZnO nanowires always showed such PED patterns. Two sets of spots in Figure 6.14 (b) are from a twin structure of ZnO with the twin plane. The third set is from double diffraction. The latter is most probably due to overlap of twinned regions of ZnO. Noticeably, similar electron diffraction pattern was observed for the ZnO whiskers grown by isothermal annealing of wurzite-type ZnO/Zn composite [161].

Figure 6.14 (d) is a high-resolution TEM (HRTEM) image of ZnO nanowires shown in Figure 6.14 (a). The image shows more clearly that the nanowire consists of two different areas (see also Figures 6.14 (d) and (e)). From the HRTEM image it was found that the ZnO nanowires grows in direction [01-10]. It should be noted that the twins of ZnO is usually imaged along the [01-10] or [2-1-10] direction of ZnO [162]. However, due to limitation of the microscope, it was not possible to tilt the ZnO to the appropriate viewing direction. In order to explain more accurately the lattice plane contrast of Figure 6.14 (d), the simulations of

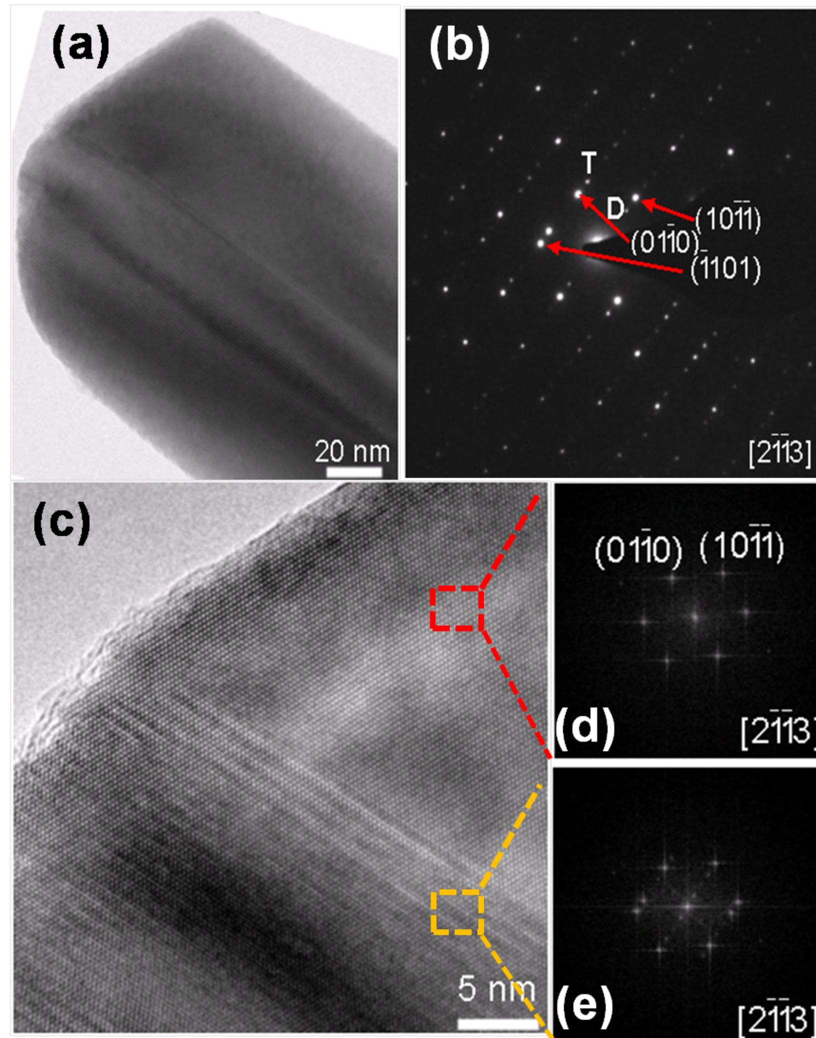

Figure 6.14: *The transmission electron microscopy of one of the nanowires (a), and the corresponding precision electron diffraction pattern (b) of the nanowire shown in (a).*

HRTEM needs to be done.
The confirmation of ZnO nanowires synthesis was further determined by the x-ray photoelectron spectroscopy (VGS 5000 ESCA). Figure 6.15 shows the three strong peaks located at 531.78 eV from O ($1s$), and both peaks at 1047.88 eV and 1022.73 eV due to the Zn ($2p\frac{1}{2}$) and ($2p\frac{3}{2}$) binding energies, respectively. Theses peaks ensures the formation of the ZnO nanostructures by direct oxidation technique used here.

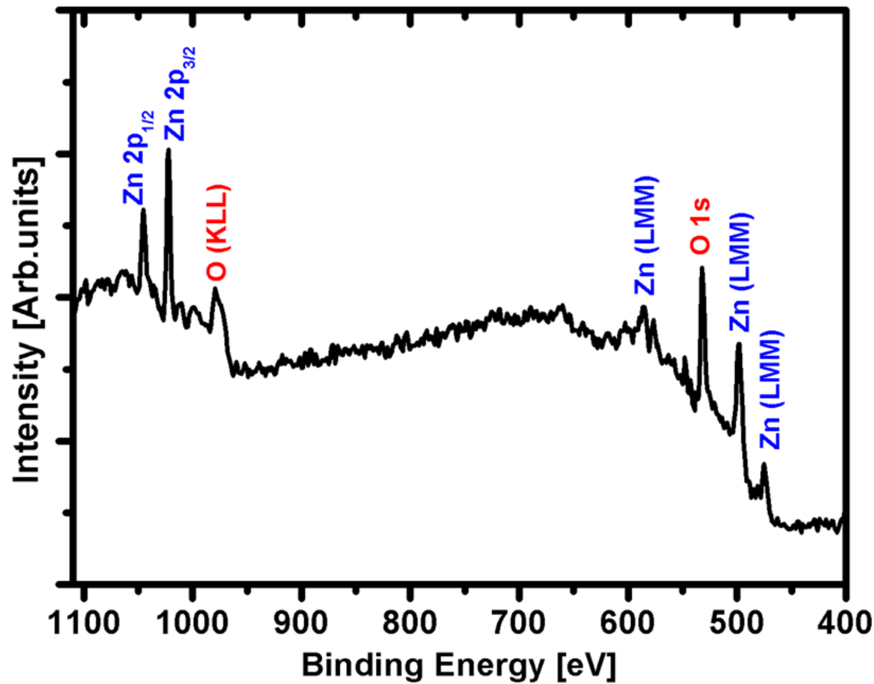

Figure 6.15: *The x-ray spectroscopy survey of the as-synthesized ZnO nanoseaurchins. The spectrum confirms the formation of ZnO.*

6.2.2.2 Electrical Properties of ZnO Nanoseaurchins

The electrical property of the as-grown ZnO nanoseaurchins was studied after making a metal contact. For comparison, the I-V characteristics of the synthesized nanoseaurchins and a pure silicon was carried out as shown in Figure 6.16 (a). This ensures that the conductance measured was from the grown nanostructures rather than the substrate. Figure 6.16 (b) shows the forward-reverse I-V measurement which indicates a typical ohmic behavior. The ketch in Figure 6.16 (d) shows how the electrical measurement was done across the two metal contacts in which they are bridged by the grown nanoseaurchins.

The UV light dependence of ZnO nanostructures is a widely known phenomena due to their large band gap (3.37 eV) and it is discussed in detail in section 6.1.2.3. Similar to UV detection experiment done for the nanosails, the UV light lamp (λ = 360 nm, UV spotlight H135, LABINO AB) was used. Figure 6.16 (c) shows the UV switching response of the ZnO nanoseaurchins while turning on and off in equal interval of time. Unlike the the switching behavior observed

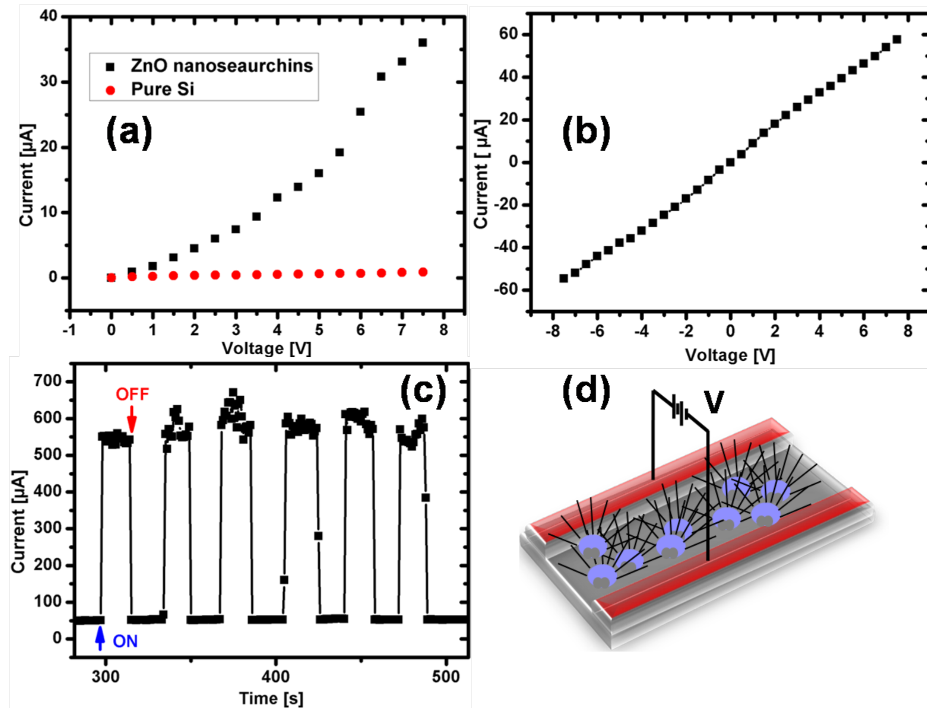

Figure 6.16: *The comparison of the I-V measurement of pure silicon and ZnO nanoseaurchins (a), the forward-reverse I-V measurement of the as-synthesized ZnO nanoseaurchins (b) and the observed UV switching response measured at 6 V (c). The sketch shows how the measurement was carried out (d). The red color on the substrate represents the metal contact.*

for the nanosails, the nanoseaurchins shows the complete recovery of the current after the UV was switched off. This effect could be attributed to the small surface area of the nanowires which has relatively less oxygen adsorption. The current increase by factor of five during UV light exposure shows a better sensitivity than nanosails shown in Figure 6.9.

6.3 Conclusion

This chapter presented two different techniques of synthesizing functional vertical ZnO nanowires: vapor-liquid-solid (VLS) and direct oxidation of Zn powder. The VLS technique resulted in the formation of high quality junctions by using Au as a catalyst on a silicon ($\langle 100 \rangle$) substrate which has a 100 nm SiO_2 insulation layer.

The junctions are formed by self organized interpenetration between nanosails during VLS growth. This effect has been capitalized for a very simple fabrication process of electrical circuits enabling the functional nanostructures in microchips. Thus, the nanosail-integrated devices showed all corresponding properties such as photo-detection or sensory features. Beside for the here demonstrated feasibility of the approach for ZnO, the process is also applicable to other VLS grown structures. The approach has been demonstrated for ZnO, but can be generalized in principle to other VLS-grown structures. For example, GaN shows the same structural features and phases.
On the other hand, the catalytic free metallic Zn oxidation technique was used to synthesize sea-urchin like nanostructures at relatively lower temperature. These nanostructures consist of ZnO nanowires with reduction in diameter in the direction of growth. In this method, large amounts of ZnO nanowires were possible to synthesize on a silicon ($\langle 100 \rangle$) substrates at temperature of 600 °C. The possible growth mechanism of these nanostructures is a direct oxidation of the metal powder which consists of two stages: nucleation and growth, in which the ZnO nuclei play a crucial role in the growth of ZnO nanowires. Most importantly, these ZnO nanowires have been produced by a simple, easy, and low cost method without the use of any catalyst which sometimes creates defects. The synthesized nanoseaurchins showed a fast switching upon UV light exposure. Moreover, it exhibited a complete recovery of the current as soon as the light was switched off.

7 Summary and Outlook

Due to their one dimensionality, nanowires are one of the best candidates for the fabrication of various novel functional devices that are based on nano scale effects such as high photo- and chemical sensitivity, quantum transport phenomena, etc., and remain still hot issue in the scientific community. Thus, various synthesis, characterization, as well as integration techniques of nanowires are being developed. However, one of the challenges in nanotechnology is the synthesis of these nanostructures in a fast, less complex, cost effective ways and on finding tolerable or easy means of integrating them into devices. This dissertation addresses some possible solutions for these problems. Therefore, three different approaches such as; thin film fracture based for the synthesis of horizontal nanowires; vapor-liquid-solid and direct oxidation of metal powders for the synthesis of vertical nanowires are used for a one step nanowire integrated device fabrication.

The thin film fracture based synthesis technique was used for the synthesis of a well aligned horizontal nanowires. This technique basically uses the mechanical failure of the photoresist for the formation of cracks. The cracks formed by the thermal cycling (drastic temperature change in the film/substrate system) could be used as a template. However, it is well known that the formation of cracks occur typically random in thin films. One method of guiding crack pattering is by creating a predefined site where the strain field is expected to concentrate. This was done by using a microstructured photoresist film using a photo-lithography. It is worth to note that the thin film stress which is the key for crack generation depends on the film thickness. For thermal cycling induced cracks, 560 nm thick shipley 1813 photoresist found to be optimal. Further filling of the cracks by physical vapor deposition method such as sputtering and further lift-off of the superfluous metal as well as photoresist by acetone ensures the formation of well

patterned polycrystalline nanowires on a thermally oxidized (100 nm thick) p-doped silicon at the same time with the conventional microstructures employed as circuit paths. This approach emphasizes the less complex, relatively inexpensive and a one step direct integration of the nanowires on a microchips. This part of the work, discussed so far, is a continuation of my master thesis where this type of synthesis was discovered, however, in this dissertation the basis for application as device was given by analyzing different properties of synthesized and already integrated nanowires.

The two dimensional confinement in the nanowires favors them to exhibit a unique electrical, magnetic, optical and mechanical properties unlike their macroscopic counter parts. To analyze these unique properties, the already integrated polycrystalline nanowires were characterized under different conditions. For majority of the nanowires the current-voltage curve seems to follow almost a linear relationship at room temperature. However, current fluctuations were discovered at a certain region of the voltage particularly in gold nanowires. On the other hand, this phenomenon was not observed for other type of nanowires including titanium and nickel. The observed fluctuation could be attributed to the type of bond formation of noble metals. The current fluctuation effect even gets pronounced for higher resistance *i.e.,* smaller diameter of the gold nanowires. Similarly, increasing and decreasing the voltage across the gold nanowires up to a particular voltage also shows an increase in conductance of the wire after each cycle. This effect could be due to the field induced grain fusing in the nanowire which decreases their interseparation. However, further increase of the voltage across the nanowires above a critical value can lead to a complete disintegration of the nanowires. These two mechanisms observed on gold nanowires implicates that the operating voltage of the devices integrated with these types of wires should be understood so as to avoid device malfunctioning.

The variable temperature electrical characterization of both gold and nickel nanowires as well as thicker nickel mesowire were also investigated. Unlike the bulk materials, both nanowires shows a drastic increase in resistance while decreasing the temperature. The typical conductivity mechanisms associated with this are believed to be a hopping assisted. In contrast, a mixed resistance response

could be created in the nickel mesowire which shows a bulk- and a nanowire-like response at various temperature regimes, allowing to tune in an almost constant conductivity value over a large temperature range as it is desired for many functional electronic devices.

The performance of nanowire integrated devices can be highly influenced by its oxidation behavior. To investigate this, two mechanisms were considered: the native oxide and the field induced oxidation. The former mechanism highly influences the shelf-life time of the device which can affect its efficiency as well as performance. The second mechanism, however, has relatively high oxidation rate and typically causes significant effect since it can be seen in any current carrying reactive materials. Therefore, to minimize or avoid this effect the device should operate at certain maximum voltage. The local, targeted anodization of nanowires by using pure water meniscus could also be achieved. This technique can be effectively used for different purposes such as for nanowire thickness control by forming core shell setups, as it could also be used for quantum wire fabrication.

The high aspect ratio of the nanowires enables them to posses a high sensitivity to a small concentration change of a chemical species as compare to their thin films and bulk counter parts. In this dissertation, palladium and ZnO polycrystalline nanowires were used to detect the presence of hydrogen and ozone, respectively. The hydrogen detection of palladium, particularly, shows two distinct responses: one an increase and the other a decrease in conductance up on exposure. This effect is associated to the response of the palladium nanowire at different hydrogen concentration where the two effects can be separately observed below or above of a certain critical value. The bulk gold material is believed to be inert however, detection of hydrogen by gold nanowire was also shown for the first time, suggesting that the so far reported interpretation in the literature might be modified.

A catalyst based vapor-liquid-solid is a widely used technique for the synthesis of various nanostructures including elemental semiconductors, II-VI semiconductors, III-V semiconductors, oxides etc. However, the integration of these

nanostructures into devices still remains typically tedious and requires many steps. In this dissertation, a direct applicable technique of one step integration of functional ZnO nanosails was developed. Synthesis of defect free high quality junctions formed by interpenetrating nanosails were able to be synthesized in an integrated surrounding. The density of interpenetrating nanosails can be enhanced by controlling the amount of gold which was used as both a catalyst during the growth and as a electrical contact later. Various electrical and sensing properties of the nanosail integrated device were carried out under various conditions. Mainly, the photo and gas sensitivity, and the field effect properties of these nanostructures showed their potential application in future nanoelectronics.

The catalyst free direct oxidation of Zn powder for the synthesis of the so called ZnO nanoseaurchins were also presented. This technique preserves a nanostructure with a high quality and free from defects such as dislocations. The development of the low temperature techniques to synthesize oxide nanostructures will be important for their integration with silicon based microelectronics and decreasing cost of fabrication. The current-voltage characteristics of the nanoseaurchins exhibited an ohmic behavior. The photo switchability of the nanoseaurchins showed a complete recovery of the current after the light is switched off. This could be due the defect free growth of the nanoseaurchins.

Generally, this dissertation is devoted on the fabrication of various nanowire integrated functional devices in a relatively simple approach. This is an important step, however, for integration of nanowires into the conventional silicon electronic processing. It is hoped that this will enable and contribute further detailed examinations of nanostructures from many more metals and semiconductors, and can be understood as one step forward for the utilization of functional nanowire devices.

Bibliography

[1] Chen., J., A brief overview of emerging nanoelectronics, *jur.rochester*, 5: p. 87 (**2008**).

[2] Beiser, A., *Concepts of Modern Physics*, The McGraw-Hill Companies, Inc. (**2003**).

[3] Mott, N. and Davis, R., *Electronic Processes in Non-Crystalline Materials*, Oxford University, Oxford (2nd Ed. ed.) (**1979**).

[4] Marzi, G., Iacopino, D., Quinn, A. J. and Redmond, G., Probing intrinsic transport properties of single metal nanowires: Direct-write contact formation using a focused ion beam., *Joun.Appl. Phys.*, 16: p. 3459 (**2004**).

[5] Wang, X. F., Zhang, J., Shi, H. Z., Wang, Y. W., Meng, G. W., Peng, X. S. and Zhang, L. D., Fabrication and temperature dependence of the resistance of single-crystalline Bi nanowires, *Journ. Appl. Phys.*, 89: p. 3847 (**2001**).

[6] Anderson, P., Absence of Diffusion in Certain Random Lattices, *Phys. Rev.*, 109: p. 1492 (**1958**).

[7] Klokhom, E., Delamination and fracture in thin films, *Communication*, 3: p. 585 (**1987**).

[8] Suo, Z., Fracture in thin films, *Princeton University, Princeton*, 26: p. 1 (**2000**).

[9] Wagner, R. S. and Ellis, W. C., Vapor-Liquid-Ssolid mechanism of single crystal growth, *Appl. Phys. Lett.*, 4: p. 89 (**1964**).

[10] Givargizov, E., *Highly Anisotropic Crystals*, Springer, New York (**1987**).

[11] Givargizov, E., Fundamental aspect of VLS growth, *J. Cryst. Growth*, 31: p. 20 (**1975**).

[12] Adhikari, H., Marshall, A., Chidsey, C. and McIntyre, P., Germanium Nanowire Epitaxy: Shape and Orientation Control, *Nano Lett.*, 6: p. 318 (**2006**).

[13] Lopez-Lopez, M., Guillen-Cervantes, A., Rivera-Alearez, Z. and Hernandez-Calderon, I., Hillocks formation during the molecular beam epitaxial growth of ZnSe on GaAs substrates, *J. Cryst. Growth*, 193: p. 528 (**1998**).

[14] Wang, Y., Zhang, L., Liang, C., Wang, G. and Peng, X., Catalytic growth and photoluminescence properties of semiconductor single-crystal ZnS nanowires, *Chem. Phys. Lett.*, 357: p. 314 (**2002**).

[15] Shimada, T., Hiruma, K., Shirai, M., Yazawa, M., Haraguchi, K., Sato, T., Matsui, M. and Katsuyama, T., Size, position and direction control on GaAs and InAs nanowhisker growth, *Superlattice Microstruct.*, 24: p. 453 (**1998**).

[16] Duan, X. and Lieber, C., General Synthesis of Compound Semiconductor Nanowires, *Adv. Mater.*, 12: p. 298 (**2000**).

[17] Huang, M. H., Wu, Y., Feck, H., Tran, N., Weber, E. and Yang, P., Catalytic Growth of Zinc Oxide Nanowires by Vapor Transport, *Adv. Mater.*, 13: p. 113 (**2001**).

[18] Nguyen, P., Ng, H., Kong, J., Cassel, A., Quinn, R., Li, J., Han, J., McNeil, M. and Meyyappan, M., Epitaxial Directional Growth of Indium-Doped Tin Oxide Nanowire Arrays, *Nano Lett.*, 3: p. 925 (**2003**).

[19] Mihi, A., Ocana, M. and Miguez, H., Oriented Colloidal-Crystal Thin Films by Spin-Coating Microspheres Dispersed in Volatile Media, *Adv. Mat.*, 18: p. 2244 (**2006**).

[20] Bomside, D., Macosko, C. and Scriven, L., On the modeling of spin coating, *J. Imag. Technol.*, 13: p. 122 (**1987**).

[21] Thompson, L., *Introduction to Microlithography*, The American Chemical Society, Wshington DC (**1983**).

[22] Moreau, W., *Semiconductor Lithography: Principles and Materials*, Plenum, New York (**1988**).

[23] Mattox, D., *Handbook of Physical vapour Deposition Processing*, Noyes Publications (**1998**).

[24] Mahan, J. E., *Physical Vapor Deposition of Thin Films*, Wiley-VCH (**2000**).

[25] Ohring, M., *The Material Science of Thin Films*, Aadamic Press (**1992**).

[26] Smith, D. L., *Thin-Film Deposition: Principle and Practice*, McGraw-Hill, Inc. (**1995**).

[27] Sauerbey, G., Verwendung von Schwingquarzen zur Wagung Dunner Schichten und Zur Mikrowagung, *Z. Physics*, 155: p. 206 (**1959**).

[28] Binnig, G. and Quate, C. F., Atomic Force Microscope, *Phys. Rev. Lett.*, 56: p. 930 (**1986**).

[29] T. Alford, J. M., L. Feldman, *Fundamentals of nanoscale film analysis*, Springer (**2007**).

[30] Murata, K., Matuskawa, T. and Shimizu, R., Monte Carlo Calculations on Electron Scattering in a Solid Target, *Jap. J. Appl. Phys.*, 10: p. 678 (**1971**).

[31] Shimizu, R., Ikuta, T. and K.Murata, The Monte Carlo technique as applied to the fundamentals of EPMA and SEM, *J. Appl. Phys.*, 43: p. 4233 (**1972**).

[32] C. Richard Brundle, J. S. W., Charles A. Evans, *Encyclopedia of Materials Characterization*, Manning Publications Co. (**1992**).

[33] E. Fuchs, H. R., H. Oppolzer, *Prticle Beam Microanalysis: Fundamentals, Methods and Applications*, VCH verlagsgesellchaft mbh (**1990**).

[34] Haghiri-Gosnet, A., Vieu, C., G.Simon, Majias, M., Carcenac, F., and Launois, H., Nanofabrication at a 10 nm length scale: limits of lift-off and electroplating transfer processes, *J. Phys. IV*, 9: pp. Pr2–133 (**1999**).

[35] Piner, R. D., Zhu, J., Xu, F., Hong, S. and Mirkin, C., Combinatorial Generation and Analysis of Nanometer- and Micrometer-Scale Silicon Features via Dip-Pen Nanolithography and Wet Chemical Etching, *Science*, 283: p. 661 (**1999**).

[36] Adelung, R., Aktas, O., Frank, J., Biswas, A., R. Kunz, M. E., Kanzow, J., Schürmann, U. and Faupel, F., Strain-controlled growth of nanowires within thin-film cracks, *nature materials*, 3: p. 375 (**2004**).

[37] Alcala, B. E., Sehitoglu, H. and Saif, T. A., Guided self accembly of metallic nanowires and channels, *Appl. Phys. Lett.*, 84: p. 4669 (**2004**).

[38] Elbahri, M., Rudra, S. K., Wille, S., Jebril, S., Schanberg, M., Paretkar, D., Kunz, R., Rui, H., Biswas, A. and Adelung, R., Employing Thin-Film Delamination for the Formation of Shadow Masks for Nanostructure Fabrication, *Adv. Matter*, 18: p. 1059 (**2006**).

[39] Jebril, S., Elbahri, M., Titazu, G., Subannajui, K., Essa, S., Niebelschuetz, F., Roehlig, C., Cimalla, V., Ambacher, O., Schmidt, B., Kabiraj, D. and D. Avasthi, R. A., Integration of Thin-Film-Fracture-Based Nanowires into Microchip Fabrication, *small*, 4(12): p. 2214 (**2008**).

[40] Griffith, A., The Phenomena of Rupture and Flow in solids, *Philos. Trans. R. Soc. London, Ser. A*, A221: p. 163 (**1920**).

[41] Klokholm, E., Delamination and Fracture of Thin-Films, *IBM, J. Res, Develop.*, 31: p. 585 (**1987**).

[42] Thouless, M., Cracking and Delamination of coatings, *J.Vac. Sci.Technol. A*, 4: p. 2510 (**1991**).

[43] Bai, T., Pollard, D. and Gao, H., Explanation for fracture spacing in layered materials, *Lett. to Nature*, 403: p. 753 (**2000**).

[44] Huang, R., Prevost, J., Huang, Z. and Suo, Z., Channel-cracking of thin films with the extended finite element method, *Eng. Fract. Mech.*, 70: p. 2513 (**2003**).

[45] Malzbender, J. and With, G., Cracking and residual stress in hybrid coatings on float glass, *Thin solid films*, 359: p. 210 (**2000**).

[46] Volinsky, A. A. and Gerberich, W., Nanoindentaion techniques for assessing mechanical reliability at the nanoscale, *Microelectronic Engineering*, 69/2-4: p. 519 (**2003**).

[47] Deshmukh, M., Ralph, D., Thomas, M. and Silcox, J., Nanofabrication using a stencil mask, *Appl. Phys. Lett.*, 75: p. 1631 (**1999**).

[48] Racz, Z., He, J., Srinivasan, S., Zhao, W., Seabaugha, A., Han, K., Ruchhoeft, P. and Wolfe, J., Nanofabrication using nanotranslated stencil masks and lift off, *J. Vac. Sci. Technol.*, B 22 (1): p. 74 (**2004**).

[49] Cook, R. and Suo, Z., Mechanisms Active durung fracture under Constraint, *MRS Bull.*, 27: p. 45 (**2002**).

[50] Hutchinson, J. W., Thouless, M. D. and Liniger, E. G., Growth and Configurational Stability of Circular, Buckling-Driven Film Delaminations, *Acta Metull. Muter.*, 40: pp. 295–308 (**1992**).

[51] Thouless, M. D., Hutchinson, J. W. and Liniger, E. G., Plane-Strain, Buckling-Driven Delamination of Thin Films,, *Acta Mefull. Muter.*, 40: pp. 2639–2649 (**1992**).

[52] Cotterell, B. and Chen, Z., Buckling and cracking of thin films on compliant substrates under compression, *Int. J. of Fractrure*, 104: p. 169 (**2000**).

[53] N. Matuda, A. K., S. Baba, Internal stress, Young's Modulus and Adhesion Energy of Carbon Films on Glass Substrates, *Thin Solid Films*, 81: p. 301 (**1981**).

[54] Volinsky, A., Moody, N. and Gerberich, W., Interfacial Toughness Measurements for Thin Films on Substrates, *Acta Mater.*, 50(3): p. 441 (**2002**).

[55] Yuse, A. and Sano, M., Transition between crack patterns in quenched glass plates, *Nature*, 362: p. 329 (**1993**).

[56] Audoly, B., Roman, B. and Pocheau, A., Secondary buckling patterns of a thin plate under in-plane compression, *Eur. Phys. J. B*, 27: p. 10 (**2002**).

[57] Adelung, R., Aktas, O., Frank, J., Biswas, A., Kunz, R., Elbahri, M., Kanzow, J., Schürman, U. and Faupel, F., Strain-controlled growth of nanowires within thin film cracks, *Nature materials*, 3: p. 375 (**2004**).

[58] Husain, A., Hone, J., Postma, H. W. C., Huang, X. M. H., Drake, T., Barbic, M., Scherer, A. and Roukes, M. L., Nanowire-based very-high-frequency electromechanical resonator, *Appl. Phys. Lett.*, 83: p. 1240. (**2003**).

[59] Kozinsky, I., Postma, H. W. C., Kogan, O., Husain, A. and Roukes, M. L., Basins of attraction of a nonlinear nanomechanical resonator, *Phys. Rev. Lett.*, 99: p. 20,720 (**2007**).

[60] *V. Cimalla, K. Brul ́ckner, A. W. Hassel, S. Milenkovic, M. A. Hein, F. Niebelschul ́tz, J. Pezoldt, H. Romanus, C. C. Röhlig, K. Tonisch, J. Weber, O. Ambacher, in Proceeding of International Workshop on Nanostructure Thin Films (NANOHARD 2007), Velingrad, Bulgaria, May 13Ű16, 2007, Eds. R. Kakanakov and L. Kolaklie, Institute of Applied Physics, Bulgaria, p. 27.* (**2007**).

[61] Durkan, C. and Welland, M. E., Size effects in the electrical resistivity of polycrystalline nanowires, *Phys. Rev. B*, 61: p. 14,215. (**2000**).

[62] Saha, S. K., Observation of giant dielectric constant in an assembly of ultrafine Ag particles, *Phys. Rev. B*, 69: p. 125,416 (**2004**).

[63] Dong, J. and Parviz, B. A., Using noise for controlled disassembly of nanoscale gold wires, *Nanotechnology*, 17: p. 5124 (**2006**).

[64] Strachan, D. R., Smith, D. E., Johnston, D. E., Park, T. H., Therien, M. J., Bonnell, D. A. and Johnsondy, A. T., Controlled fabrication of

nanogaps in ambient environment for molecular electronics, *Appl. Phys. Lett.*, 86: p. 043,109 (**2005**).

[65] Gornyi, I. V., Mirlin, A. D. and Polyakov, D. G., Interacting Electrons in Disordered Wires: Anderson Localization and Low-T Transport, *Phys. Rev. Lett.*, 95: p. 206,603 (**2005**).

[66] Yoon, C. O., Reghu, M., Moses, D. and Heeger, A. J., Transport near the metal-insulator transition: Polypyrrole doped with PF6, *Phys. Rev. B.*, 49: p. 10,851 (**1994**).

[67] Fogler, M. M., Teber, S. and Shklovskii, B. I., Variable-range hopping in quasi-one-dimensional electron crystals, *Phys. Rev. B*, 69: p. 035,413 (**2004**).

[68] Dynes, R. C. and Garno, J. P., Metal-Insulator Transition in Granular Aluminum, *Phys. Rev. Lett.*, 46: p. 137 (**1981**).

[69] Cabrera, N. and Mott, N. F., Theory of the oxidation of metals, *Rep. Prog. Phys.*, 12: p. 163 (**1949**).

[70] Mott, N. F., The theory of the formation of protective oxide films on metalls III, *Trans. Faraday Soc.*, 43: p. 429 (**1947**).

[71] Wagner, C., Theory of the tarnishing process, *Z.Phys. Chem.*, B21: p. 25 (**1933**).

[72] Lawless, K. R., The oxidation of metals, *Rep. Prog. Phys.*, 37: p. 231 (**1974**).

[73] Anderson, J. R. and Ritchie, I. M., The effect of an electric field on the oxidation rate of nickel between 250 and 380 C, *Proc. R. Soc. A*, 299: p. 371 (**1967**).

[74] Gordon, A. E., Fayfield, R. T., litfin, D. D. and Higman, T. K., Mechanisms of surface anodization produced by scanning probe microscopes, *J. Vac. Sci. Technol., B*, 13: p. 2805 (**1995**).

[75] Ebinger, H. D. and J. T. Yates, J., Electron-impact-induced oxidation of Al(111) in water vapor: Relation to the Cabrera-Mott mechanism, *Phys. Rev. B*, 57: p. 1976 (**1998**).

[76] Nawak, C., Kirchheim, R. and Schmitz, G., Electric-field-induced low temperature oxidation of tungsten nanowires, *Appl. Phys. Lett.*, 89: p. 143,104 (**2006**).

[77] Snow, E. S. and Campbell, P. M., AFM Fabrication of Sub-10-Nanometer Metal-Oxide Devices with in Situ Control of Electrical Properties, *Science*, 270: p. 1639 (**1995**).

[78] Avouris, P., Hertel, T. and Martel, R., Atomic force microscope tip-induced local oxidation of silicon: kinetics, mechanism, and nanofabrication, *Appl. Phys. Lett.*, 71 (2): p. 285 (**1997**).

[79] Day, H. C. and Allee, D. R., Selective area oxidation of silicon with a scanning force microscope, *Appl. Phys. Lett.*, 62: p. 2691 (**1993**).

[80] Matsumoto, K., Ishii, M., Segawa, K., Oka, Y., Vartanian, B. J. and Harris, J. S., Room temperature operation of a single electron transistor made by the scanning tunneling microscope nanooxidation process for the TiOx/Ti system, *Appl. Phys. Lett.*, 68 (1): p. 34 (**1996**).

[81] Sugimura, H., Uchida, T., Kitamma, N. and H.Masuhara, Scanning Tunneling Microscope Tip-Induced Anodization for Nanofabrication of Titanium, *J. Phys. Chem.*, 98: p. 4352 (**1994**).

[82] Minne, S. C., Soh, H. T., Flueckiger, P. and Quate, C. F., Fabrication of 0.1 ţm metal oxide semiconductor field-effect transistors with the atomic force microscope, *Appl. Phys. Lett.*, 66: p. 703 (**1995**).

[83] Yang, T. S., Cho, W., Kim, M., An, K.-S., Chung, T.-M., G.Kim, C. and Kim, Y., Atomic layer deposition of nickel oxide films using Ni (dmamp)2 and water, *J. Vac. Sci. Technol.*, A 23: p. 4 (**2005**).

[84] Clarke, L., Wybourne, M. N., Brown, L. O., Hutchison, J. E., Yan, M., Cai, S. X. and Keana, J. F. W., Room-temperature Coulomb-blockade-

dominated transport in gold nanocluster structures, *Semicond. Sci. Technol.*, 13: p. A111 (**1998**).

[85] Carrey, J., Seneor, P., Lidgi, N., Jaffre, H., Dau, F. N. V., Fert, A., Friederich, A., Montaigne, F. and Vaures, A., Capacitance variation of an assembly of clusters in the Coulomb blockade regime, *J. Appl. Phys.*, 95: pp. 1265–1268 (**2004**).

[86] Yano, K., Ishii, T., Hashimoto, T., Kobayashi, T., F.Murai and Seki, K., Room-temperature single-electron memory, *IEEE Trans. Electron. Devices*, 41: pp. 1628–1638 (**1994**).

[87] Yano, K., Ishii, T., Hashimoto, T., Kobayashi, T., Murai, F. and Seki, K., Transport characteristics of polycrystalline-silicon wire influenced by single-electron charging at room temperature, *Applied Phys. Lett.*, 67: pp. 828–830 (**1995**).

[88] Im, Y. H., Lee, C., Vasquez, R., Bangar, M., Myung, N., Menke, E., Penner, R. and Yun, M., Investigation of a Single Pd Nanowire for Use as a Hydrogen Sensor, *Small*, 2(8): p. 356 (**2006**).

[89] Wan, Q., Li, Q. H., Chen, Y. J., Wang, T. H., He, X. L., Li, J. P. and Lin, C. L., Fabrication and ethanol sensing characteristics of ZnO nanowire gas sensors, *Appl. Phys. Lett.*, 84: p. 3654 (**2004**).

[90] Gao, Z., Agarwal, A., Trigg, A., Singh, N., Fang, C., C.H.Tung, Fan, Y., Buddharaju, K. and Kong, J., Silicon nanowire arrays for label-free detection of DNA, *Anal. Chem.*, ,79: pp. 3291–3297 (**2007**).

[91] Lu, Y., Yang, M. and Qu, F., Enzyme-functionalized gold nanowires for the fabrication of biosensors, *Bioelectrochem.*, 71: pp. 211–216 (**2007**).

[92] Aravamudhan, S., Kumar, A., Mohapatra, S. and Bhansali, S., Sensitive estimation of total cholesterol in blood using Au nanowires based microfluidic platform., *Biosen. Bioelectron.*, 22: pp. 2289–2294 (**2007**).

[93] Favier, F., Walter, E. C., Zach, M. P., Benter, T., and Penner, R. M., Hydrogen Sensors and Switches from Electrodeposited Palladium Mesowire Arrays, *Science*, 293: p. 2227 (**2001**).

[94] Atashbar, M. and Singamaneni, S., Room temperature gas sensor based on metallic nanowires, *Sens. Actuators B*, 111/112: pp. 13–21 (**2005**).

[95] Walter, E. C., Favier, F. and Penner, R. M., Palladium Mesowire Arrays for Fast Hydrogen Sensors and Hydrogen-Actuated Switches, *Anal. Chem.*, 74: p. 1546 (**2002**).

[96] Kong, J., Chapline, M. and Dai, H., Functionalized Carbon Nanotubes for Molecular Hydrogen Sensors, *Adv. Matter.*, 13: pp. 1384–6 (**2001**).

[97] Wong, Y. M., Kang, W. P., Davidson, J. L., Wisitsora-at, A. and Soh, K. L., A novel microelectric gas sensor utilizing carbon nanotube for hydrogen gas detection, *Sens. Actuators B*, 93: p. 327 (**2003**).

[98] Grimes, C. A., Ong, K. G., Varghese, O. K., Yang, X. P., Mor, G., M. Paulose, E. C. D., Ruan, C. M., Pishko, M. V., Kendig, J. W. and Mason, A. J., A Sentinel Sensor Network for Hydrogen Sensing, *Sensors*, 3: p. 69 (**2003**).

[99] Yan, S., Maeda, H., Kusakabe, K. and Morooka, S., Thin Palladium Membrane Formed in Support Pores by Metal-Organic Chemical Vapor Deposition Method and Application to Hydrogen Separation, *Ind. Eng. Chem. Res.*, 33: p. 616 (**1994**).

[100] Sakamoto, Y., Takai, K., Takashima, I. and Imada, M., Electrical resistance measurements as a function of composition of palladiumŰhydrogen(deuterium) systems by a gas phase method, *J. Phys.: Condens.*, 8: p. 3399Ű411 (**1996**).

[101] Sanchez, A., Abbet, S., Heiz, A. U., Schneider, W., Hakkinen, H., Barnett, R. and Landman, U., When Gold Is Not Noble: Nanoscale Gold Catalysts, *J. Phys. Chem. A*, 103: p. 9573 (**1999**).

[102] Hakkinen, H., Moseler, M. and Landman, U., Bonding in Cu, Ag, and Au Clusters: Relativistic Effects, Trends, and Surprises, *Phys. ReV. Lett.*, 89: p. 033,401 (**2002**).

[103] Barnett, R. N., Haekkinen, H., Scherbakov, A. G. and Landman, U., Hydrogen Welding and Hydrogen Switches in a Monatomic Gold Nanowire, *Nano Lett.*, 4 (10): pp. 1845–52 (**2004**).

[104] Heo, Y., Kang, B., Tien, I., Norton, D., Ren, F., La, J., Roche and Pearton, S., UV photoresponse of single ZnO nanowires, *Appl. Phys. A*, 80: p. 497 (**2005**).

[105] H.Kind, Yan, H., Messer, B., Law, M. and Yang, P., Nanowire UV photodetector and optical switches, *Adv. Mater.*, 14: p. 158 (**2002**).

[106] Martins, R., Fortunato, E., Nunes, P., Ferreira, I., Marques, A., Bender, M., Katsarakis, N., Cimalla, V. and Kiriakidis, G., Zinc oxide as an ozone sensor, *J. Appl. Phys.*, 96(3): p. 1398 (**2004**).

[107] Kofsad, P., *Nonstoichiometry, Diffusion and Electrical Conductivity in Binary Metal Oxides*, Wiley, New York (**1972**).

[108] Wang, Y., Schmidt, V., Senz, S. and Gösele, U., Epitaxial growth of silicon nanowires using an aluminium catalyst, *Nature Nanotech.*, 1: p. 186 (**2006**).

[109] Sekar, A., Kim, S., Umar, A. and Hahn, Y., Catalyst-free synthesis of ZnO nanowires on Si by oxidation of Zn powders, *Journal of Crystal Growth*, 277: p. 471 (**2005**).

[110] Noborisaka, J., Motohisa, J., Hara, S. and Fukui, T., Fabrication and characterization of freestanding GaAs/AlGaAs core-shell nanowires and AlGaAs nanotubes by using selective-area metalorganic vapor phase epitaxy, *Appl.Phys.L ett.*, 87: p. 093,109 (**2005**).

[111] Mohan, P., Motohisa, J. and Fukui, T., Realization of conductive InAs nanotubes based on lattice-mismatched InP/InAs core-shell nanowires, *Appl.Phys. Lett.*, 88,: p. 013,110 (**2006**).

[112] Park, W. I., Lee, C.-H., Chae, J. H., Lee, D. H. and Yi, G.-C., Ultrafine ZnO nanowire electronic device arrays fabricated by selective MetalŰOrganic Chemical Vapor Deposition, *Small*, 5: p. 181 (**2009**).

[113] Morales, A. and Lieber, C., A Laser Ablation Method for the Synthesis of Crystalline Semiconductor Nanowires, *Science*, 279: pp. 208–211 (**1998**).

[114] Ding, Y., Gao, P. and L.Wang, Z., Catalyst-nanostructure interfacial lattice mismatch in determining the shape of VLS grown nanowires and nanobelts, *J. Am.Chem. Soc.*, 126: p. 2066 (**2004**).

[115] Gao, P. X. and .Wang, Z. L., Self-Assembled Nanowire -Nanoribbon Junction Arrays of ZnO, *J. Phys. Chem. B*, 106: p. 12,653 (**2002**).

[116] Li, S. Y., Lee, C. Y. and Tseng, T. Y., Copper-catalyzed ZnO nanowires on silicon (1 0 0) grown by vapor-liquid-solid process, *J. Cryst. Growth*, 247: p. 357 (**2003**).

[117] Zhao, Q. X., Willander, M., Morjan, R. R. ., Hu, Q. H. and Campbell, E. E. B., Optical recombination of ZnO nanowires grown on sapphire and Si substrates, *Appl. Phys. Lett.*, 83: p. 165 (**2003**).

[118] Ng, H. T., Chen, B., Li, J., Han, J., Meyyappan, M., Wu, J., Li, S. X. and Haller, E. E., Optical properties of single-crystalline ZnO nanowires on m-sapphire, *Appl. Phys. Lett.*, 82: p. 2023 (**2003**).

[119] Lao, C. S., Gao, P. X., Yang, R. S., Zhang, Y., Dai, Y. and Wang, Z. L., Formation of double-side teethed nanocombs of ZnO and self-catalysis of Zn-terminated polar surface, *Chem. Phys. Lett.*, 417: p. 359 (**2005**).

[120] Kong, X. Y. and Wang, Z. L., Spontaneous polarization-induced nanohelixes, nanosprings, and nanorings of piezoelectric nanobelts, *Nano Lett.*, 3: p. 1625 (**2003**).

[121] Wang, X., Ding, Y., Summers, C. J. and Wang, Z. L., Large-Scale Synthesis of Six-Nanometer-Wide ZnO Nanobelts, *J. Phys. Chem. B*, 108: pp. 8773–8777 (**2004**).

[122] Wang, Z. L., Kong, X. and Zuo, J., Induced Growth of Asymmetric Nanocantilever Arrays on Polar Surfaces, *Phys. Rev. Lett.*, 91(18): pp. 185,502–1 (**2003**).

[123] Chan, W. M., Tringe, J., Shalish, I. and Narayanamurti, V., Role of planar defects in compound semiconductor crystals: fom growth of nanomasts and nanosails to processing light emission in dualbeam FIB/SEM, *Microsc. Microanal.*, 13 (Suppl 2): p. 722 (**2007**).

[124] Comini, E., Faglia, G., Sberveglieri, G., Pan, Z. and Wang, Z. L., Stable and highly sensitive gas sensors based on semiconducting oxide nanobelts, *Appl. Phys. Lett.*, 81: p. 1869 (**2002**).

[125] Arnold, M. S., Avouris, P., Pan, Z. W. and Wang, Z. L., Field-Effect Transistors Based on Single Semiconducting Oxide Nanobelts, *J. Phys. Chem. B*, 107: p. 659 (**2003**).

[126] Fan, H. J., Werner, P. and Zacharias, M., Semiconductor nanowires: from self-organization to growth control, *Small*, 2 (6): pp. 700–717 (**2006**).

[127] Wang, X. D., Graugnard, E., King, J. S., Wang, Z. L. and Summers, C. J., Large-Scale Hexagonal-Patterned Growth of Aligned ZnO Nanorods for Nano-optoelectronics and Nanosensor Arrays, *Nano Lett.*, 4: p. 423 (**2004**).

[128] Haraguchi, K., Hiruma, K., Katsuyama, T., Tominaga, K., Shirai, M. and Shimada, T., Self-organized fabrication of planar GaAs nanowhisker arrays, *Appl. Phys. Lett.*, 69: p. 386 (**1996**).

[129] Islam, M. S., Sharma, S., Kamins, T. I. and Williams, R. S., Ultrahigh-density silicon nanobridges formed between two vertical silicon surfaces, *Nanotechnology*, 15: pp. L5–L8 (**2004**).

[130] Chen, R. S., Wang, S., Lan, Z., Tsai, J. T., Wu, C., Chen, L., Chen, K., Huang, Y. and Chen, C., On-Chip Fabrication of Well-Aligned and Contact-Barrier-Free GaN Nanobridge Devices with Ultrahigh Photocurrent Responsivity, *Small*, 4: p. 925 (**2008**).

[131] Patolsky, F., Timko, B. P., G. Yu, Y. F., Greytak, A. B., Zheng, G. and Lieber, C. M., Detection, stimulation, and inhibition of neuronal signals with high-density nanowire transistor arrays, *Science*, 313: p. 1100 (**2006**).

[132] Wang, Z. L., *Nanowires and Nanobelts - Materials, Properties and Devices, vol. 1: Metal and Semiconductor Nanowires*, Kluwer Academic Publishers, Amsterdam (**2004**).

[133] Borchers, C., Müller, S., Stichtenoth, D., Schwen, D. and Ronning, C., Catalyst-Nanostructure Interaction in the Growth of 1-D ZnO Nanostructures, *J. Phys. Chem. B*, 110: p. 1656 (**2006**).

[134] Vincent, R. and Midgley, P., Double conical beam-rocking system for measurement of integrated electron diffraction intensities, *Ultramicroscopy*, 53: p. 271 (**1994**).

[135] J.Gjonnes, V.Hansen and Krerneland, A., The Precession Technique in Electron Diffraction and Its Application to Structure Determination of Nano-Size Precipitates in Alloys, *Microscopy and Microanalysis*, 10: p. 16 (**2004**).

[136] Weirich, T. E., Portillo, J., Cox, G., Hibst, H. and Nicolopoulos, S., Ab initio determination of the framework structure of the heavy-metal oxide CsxNb2.54W2.46O14 from 100 kV precession electron diffraction data, *Ultramicroscopy*, 106: p. 164 (**2006**).

[137] Gemmi, M., Zou, X., Hovmoller, S., Migliori, A. and Andersson, M. V. Y., Structure of Ti2P solved by three-dimensional electron diffraction data collected with the precession technique and high-resolution electron microscopy, *Acta Cryst.*, A59: p. 117 (**2003**).

[138] Stadelmann, P. A., EMS - a software package for electron diffraction analysis and HREM image simulation in materials science, *Ultramicroscopy*, 21: p. 131 (**1987**).

[139] Wang, Z., Daemen, L. L., Zhao, Y., Zha, C. S., Downs, R. T., Wang, X., Wang, Z. L. and Hemley, R. J., Morphology-tuned wurtzite-type ZnS nanobelts, *Nature Mater.*, 4: p. 922 (**2005**).

[140] Ding, Y. and Wang, Z. L., Structure Analysis of Nanowires and Nanobelts by Transmission Electron Microscopy, *J. Phys. Chem. B*, 108: p. 12,280 (**2004**).

[141] Ay, M., Nefedov, A. and Zabel, H., Different growth modes of Au films on ZnO(000-1), *Surf. Sci.*, 600: p. 5062 (**2006**).

[142] Dai, Y., Zhang, Y., Bai, Y. Q. and Wang, Z. L., Bicrystalline zinc oxide nanowires, *Chem. Phys. Lett.*, 375: p. 96 (**2003**).

[143] Chen, Y. X. and Guo, S. W., Twinning-induced ZnO bicrystalline nanobelts, *Mater. Lett.*, 61: p. 5275 (**2007**).

[144] Dai, Y., Zhang, Y. and Wang, Z. L., The Octa-twin Tetraleg ZnO. Nanostructures, *Sol. State Commun.*, 126: p. 629 (**2003**).

[145] Huang, Y., Zhang, Y., Bai, X., He, J., Liu, J. and Zhang, X., Bicrystalline Zinc Oxide Nanocombs, *J. Nanosci. Nanotechnology*, 6: p. 2566 (**2006**).

[146] Chen, Y., Xing, Q. and Guo, S., Two-dimensional and three-dimensional ZnO nanostructures induced by twinnings, *Nanotechnology*, 18(1): p. 245,607 (**2007**).

[147] Bere, A. and Serra, A., Atomic structures of twin boundaries in GaN, *Phys. Rev. B*, 68: p. 033,305 (**2003**).

[148] J.Suehiro, Nakagawa, N., i. Hidaka, S., Ueda, M., Imasaka, K., Higashihata, M., Okada, T. and Hara, M., Dielectrophoretic fabrication and characterization of a ZnO nanowire-based UV photosensor, *Nanotechnology*, 17: p. 2567 (**2006**).

[149] Janotti, A. and deWalle, C. G. V., Oxygen vacancies in ZnO, *Appl. Phys. Lett.*, 87: p. 122,102 (**2005**).

[150] Lany, S. and Zunger, A., Anion vacancies as a source of persistent photoconductivity in II-VI and chalcopyrite, *Phys. Rev. B*, 72: p. 035,215 (**2005**).

[151] Melnick, D. A., Zinc Oxide Photoconduction, an Oxygen Adsorption Process, *J. Chem. Phys.*, 26: p. 1136 (**1957**).

[152] Reemts, J. and Kittel, A., Persistent photoconductivity in highly porous ZnO films, *J. Appl. Phys.*, 101: p. 013,709 (**2007**).

[153] Takahashi, Y., Kanamori, M., Kondoh, A., Minoura, H. and Ohya, Y., Photoconductivity of Ultrathin Zinc Oxide Films, *Jpn. J. Appl. Phys.*, 33: p. 6611 (**1994**).

[154] Li, Q. H., Liang, Y. X. and Wang, T. H., Near-term aging and thermal behavior of polyfluorene in various aggregation states, *Appl. Phys.Lett.*, 84: p. 22 (**2004**).

[155] Wang, H. T., Kang, B. S., Ren, F., Tien, L. C., Sadik, P. W., Norton, D. P., Pearton, S. J. and Lin, J., Hydrogen-selective sensing at room temperature with ZnO nanorods, *Appl. Phys. Lett.*, 86: p. 243,503 (**2005**).

[156] Mitzner, K. D., Sternhagen, J. and Galipeau, D. W., Development of a micromachined hazardous gas sensor array, *Sns. Actuators B*, 93: p. 92 (**2003**).

[157] H.L. Hartnagel, A. J. C. J., A.L. Dawar, *Semiconducting Transparent Thin Films*, IOP, Bristol (**1995**).

[158] Lin, C. C., Chen, S. Y., Cheng, S. Y. and Lee, H. Y., Properties of nitrogen-implanted p-type ZnO films grown on Si3N4/Si by radio-frequency magnetron sputtering, *Appl. Phys. Lett.*, 84: p. 5040 (**2004**).

[159] Heiland, G. and Kohl, D., *Chemical Sensor Technology*, Kodansha, Tokyo (**1983**).

[160] Saito, S., Miyayama, M., Kuomoto, K. and Yanagida, H., Gas Sensing Characteristics of Porous ZnO and Pt/ZnO Ceramics, *J. Am. Ceram. Soc.*, 68: p. 40 (**1985**).

[161] Huang, B.-H., Chen, S.-Y. and Shen, P., 10-11 and 11-21-Specific Growth and Twinning of ZnO Whiskers, *J. Phys. Chem. C*, 112: p. 1064 (**2008**).

[162] Ding, Y. and Wang, Z., Structures of planar defects in ZnO nanobelts and nanowires, *Micro*, 40: p. 335 (**2009**).

List of Figures

2.1 Schematic illustrating of electronic density of states (DOS) with their corresponding degree of freedom . Systems with 3, 2, 1 and 0 dimensions can be referred as bulk, quantum well, quantum wire and quantum dots, respectively. 6
2.2 Sketch showing the two possible electron transport mechanisms. Diffusive electron transport. Numerous scattering (top) and ballistic electron transport: Electrons are only backscattered at the boundary (bottom). l refers to the mean free path of the conduction electrons. 8
2.3 Sketch showing quantum tunneling: finite potential wall (top) and the incident, partly reflected and partly transmitted wave function of the particle as the function of distance (x) (bottom). 9
2.4 The volume of strain energy released by the formation of a crack is larger in a freestanding film under uniaxial tension (a) than in a film bonded to a substrate subjected to a biaxial film stress (b). 14
2.5 Schematic showing the principal steps of VLS growth : initial nucleation and continued growth (a), and a phase diagram of Au-Si binary system (b). 18

3.1 Spin coating stages: deposition (a), spin-up (b), spin-off (c) and evaporation (d). 21
3.2 Schematic representation of the photolithographic process sequence (a) such as positive resist coating (i), photoexposing (ii), and developing (iii), and the photo of the microstructured resist on a silicon wafer prepared by this technique (b). 23

3.3 The physical vapor deposition chamber used for thin film preparation: Photo (a) and inner part of the chamber (b). The numbers represent sputtering sources (1 and 2), evaporation source (5), quartz crystal microbalance (3) and a sample holder (4). 24

3.4 The sketch showing the metal evaporator with a power feed through (a), and both the external (b) and the internal (c) part of the metal evaporator cell. 26

3.5 Shadow effects observed in evaporated films. Arrows show the trajectory of the material atoms being deposited. 27

3.6 Sketch showing the principle of magnetron sputtering. 29

3.7 Quartz-crystal deposition monitor in crossection. 29

3.8 Schematic illustrating three basic modes of initial nucleation in film growth: Island (Volmer-Weber) growth (a), layer (Frank-van der Merwe) growth (b) and Island-layer (Stranski-Krastonov)growth (c) 32

4.1 Schematic illustration of reflection of light from the delaminated thin film. As the result the crack appears darker when it is observed by optical microscope. 35

4.2 Schematic representation of an atomic force microscope (a). The inset shows the close view of the tip-surface interaction. The tip-effect (b) and the force-displacement curve (c) are also shown. . . 37

4.3 Sketch depicting contact mode (a) and noncontact mode (b) of AFM. 38

4.4 The AFM image of the nanowires synthesized by using thin film fracture approach (see chapter 5). The inset shows the roughness of the nanowires. 39

4.5 Schematic diagram of a scanning electron microscope (a), and ray paths in SEM; standard arrangement for image formation (b). . . 41

4.6 Schematic diagram illustrating the volume of material that is probed by an incident electron beam together with the volumes from which x-rays and backscattered, Auger and secondary electrons emanates. 43

4.7 EDX spectra of the as-synthesized ZnO nansails which confirms the presence of Zinc as well as oxygen. 44

4.8 Sketch showing how the x-ray and auger electrons are emitted as the result of the energy release by the electron from the highre states returns to its ground state [33]. 45

4.9 Schematic layout and ray diagrams of a transmission electron microscope. Ray diagram for bright field imaging: the aperture angle of the bundle of rays leaving each object point is limited to approx. 1 mrad by the objective aperture (a), and ray diagram for selected area of diffraction (SAD). 47

4.10 Imaging mode: bright field (BF) mode (a), dark field (DF) mode (displaced aperture), dark field mode (centered) and high resolution mode. 48

4.11 A sketch showing the basic process of photoelectron emissions (a)and (b). 50

4.12 Photo of the microchip holder device which was used to measure the electrical properties of various nanowires. The inset (top-left) shows the microchip consists of horizontal nanowires at each of the contact junctions, and the number refers to the contact points. . . 51

5.1 General processing steps for nanowire fabrication based on thin film fracture. A well cleaned silicon substrate with 100 nm thick oxide is masked by a photoresist film by spin - coating (b). A microstructuring process by exposing the thin film with UV or e-beam lithography to create a suitable design (c) by using a mask yields a rectangular shape film after removing the UV exposed area (e.g. for positive resist). The cracks generation by thermal cycling (d) and finally the material deposition(e) and successive mask lift-off results formation of nanowires and electrical contacts (f). 57

5.2 Microstructured photoresist on Silicon substrate (a), the magnified image of one of the microchips (b) and the site where patterned cracks were observed (c). 58

5.3 Optical microscopy of different crack patterns on a 10 μm (a), 8 μm (b) and 6 μm (c) stripes. 59

5.4 The Scanning electron microscopy image of photoresist film upon thermal cycling. Buckling-driven delamination (a) buckled (b) and worm-like or telephone cord formation (c). 61

5.5 Images of Au nanowires (NWs) integrated in a microchip. Optical microscopy image showing a well-organized ”zig-zag” pattern of NWs between two electrical contacts (yellow areas) (a). In contrast, next to the contacts, an unorganized pattern of wires can be found. The photographs in the inset show the wafer (7.62 cm in diameter) consists of chips (each 1 cm^2); the position where the microscopy image was taken is marked with an arrow. AFM image of polycrystalline Au NWs (b). Magnification of (b) showing the typical thickness variation along the NW (c), indicating the granular nature of the wires, which is important for sensor applications. Typical fabrication problems (d). Arrow 1 points to a swing by of the NW caused by a thickness gradient in the step edge (magnified on the right), and arrow 2 shows a discontinuity. 63

5.6 Sketch of the NW formation steps for the bow-tie-type microstructure pattern (a) and SEM image of the contacted NWs after cracking of the resist film, metal deposition, and mask lift-off (b). A further etching step converts the wires into a free-standing bridge. 65

5.7 The I-V characteristics of both Au nanowires with resistances of 10 $k\Omega$ (a), and 2.6 $M\Omega$ (b), and Ti nanowires with resistance 4 $M\Omega$ (c) and 0.01 $M\Omega$ (d). Current fluctuation at higher voltage was observed in Au nanowires. 67

5.8 The I-V characteristics of Au nanowires with resistances of 3 MΩ (a),and 0.25 MΩ (b). Sketch indicating the polarization by the high electrical field between grains (c), and grain fusing leading to the formation of a path of enhanced conductivity (d). 68

5.9 Temperature dependence of nanowire resistance: I-V characteristics of Ti NWs upon heating from room temperature to 363 K (a). Resistance versus temperature at 100 mV for Au (b) where the red solid line represents the power-law fit to the data (R $\sim T^{-\alpha}$), and the fit for Ni NWs shows a 1D variable-range hopping (VRH) (R $\sim \exp(T_0/T)^{0.5}$ (c). 69

5.10 Resistance versus temperature for a Ni mesowire. The resistance changes by only 0.6 kΩ in a temperature range of more than 110 K, representing an effective temperature coefficient of 2×10^{-4}, one order of magnitude smaller than the bulk value of 3×10^{-3}. The increase in resistance indicates two mechanisms: hopping-assisted transport at low temperatures (b) (the solid line is a power-law fit (R $\sim T^{-\alpha}$)) to the data) and phonon scattering at relatively higher temperatures (c). 71

5.11 Electron energy level diagrams, before (a) and after (b) electron equilibrium, illustrating how the transfer of the electrons from the metal to oxygen adsorbed on the surface of a thin, growing oxide film generates a uniform Electric field according to Cabrera-Mott theory. E_b, $\Delta\phi$ and ϕ represent the Mott potential, the voltage across the film and the work function of the metal, respectively. . 73

5.12 The native oxidation (resistance versus time) (a) and the field-induced oxidation characteristic (b) of Ni nanowires as function of resistance and time. 76

5.13 Schematic representation of local anodization of nanowires (a) and the photo showing how the electrodes and the film are potentially biased (b). 77

5.14 The current versus anodization time of 10 nm (a) and 50 nm (b). The current was measured through the film during the anodization process. 78

5.15 x-ray photo spectroscopy (XPS) analysis of the 50 nm Ti film after anodization which reveals the formation of TiO_2. 79

5.16 Photo of the contact angle measuring device used for placing the water droplet(a), and the sketch featuring where the water droplet was placed (b). 80

5.17 The current measured through the Ti nanowire per time at 10 V anodization voltage (a) and the I-V characteristics of the Ti nanowire after anodizing with a voltage of 10 V for a period of 5 minutes (b). 81

5.18 The I-V characteristics of the Ti nanowire at different anodization voltage (a), and the change in conductance of the nanowire at various anodization voltage (b) 83

5.19 The temperature dependence of the current measured through the Ti-TiO_2 core shell nanowire measured at constant 0.2 V (a), and the current-Voltage characteristics of the core shell nanowire at different temperatures(b) 84

5.20 The I-V measurement of the Ti-TiO_2 core shell nanowire at room and low temperatures. 85

5.21 The resistance change of Pd polycrystalline nanowires per time upon hydrogen exposure (a) and current vesus time plot for the same type of nanowires in 10% hydrogen gas (b). 87

5.22 Response of Au polycrystalline nanowires upon exposure to hydrogen gas. 88

5.23 The resistance response of ZnO nanowires upon ozone exposure. The green and red arrows represent the UV photoreduction and subsequent ozone reoxidation of zinc oxide nanowire, respectively. 89

6.1 Schematic diagram of the experimental set up used for the ZnO nanosail growth. 95

6.2 The optical image of a 10 μm wide channel after 50 nm Au deposition (a)and scanning electron microscopy image after Zno nanosail growth (b). The gap between the contacts are bridged by the grown nanosails. The inset shows the interpenetration of nanosails. 96

6.3 The scanning electron microscopy image of the Au contacts after ZnO growth up on increasing magnification from (a) to (c). The inset in (c) shows the interpenetrating nanosails. The sketch shows the grown nanosails including the possible interpenetration which bridges the 10 μm gap between the contacts(d). 98

6.4 TEM investigation of the nanosails structure: nanosails are terminated on one side by (0001) layers, while the opposite edge contains steps, see arrows (a), Bright-field high resolution micrograph near the interface Au / ZnO with corresponding PED pattern. (right, rotation corrected), all aligned in zone axis orientation [2-1-10] (b). Experimental and simulated HRTEM micrographs (inserted, t = 3.3 nm) for zone axis [2-1-10]. Here, Δf and Δt represents the change in focus and the specimen thickness, respectively (c). . . . 99

6.5 Microscopic and electronic features of interpenetrated nanosails (a), and intergrowth (b) of two nanosails with PED patterns, common zone axis [2-1-10]. 100

6.6 The scanning electron microscopy image (a) and the I-V characteristics (b) of the low density ZnO nanosails. The I-V curve shows no current measured between the two Au contacts. 102

6.7 The I-V characteristics of the ZnO nanosails at both 0 V and 2 V gate voltage(a), and the sketch showing the shottkydiode foramtion on the ZnO-Au contacts (b). 103

6.8 The I-V characteristics of the high density ZnO nanosail which are integrated into device both at 300 and 16 K. 104

6.9 The UV light response of the ZnO nanosails (a). The ”ON” and ”OFF” signs refer to the UV light exposure and dark states , respectively. The I-V characteristics comparison of the nanosails at both states (b). 105

6.10 The resistance response of ZnO nanosails to 10% hydrogen exposure. 107

6.11 The sketch shows the furnace used for the synthesis of sea-urchin-like ZnO nanostructures. 108

6.12 The schematic illustration of the the nanoseaurchins growth process: the mixture of Zn powder and ethanol dispersed on Si substrate (a); formation of aggregated Zn droplets (b); formation of ZnO nuclei on the surface of Zn droplets (c); growth nanowires out of the droplets (d). 110

6.13 The scanning electron microscopy of the ZnO nanoseaurchins at different stages. Microspheres (a) and microbowls shows the early stage of the synthesis. The melted and aggregated Zn powders and the as-synthesized ZnO nanoseaurchins are shown in (c) and (d), respectively. The inset in (d) shows the relatively high magnification of the nanoseaurchins. 111
6.14 The transmission electron microscopy of one of the nanowires (a), and the corresponding precision electron diffraction pattern (b) of the nanowire shown in (a). 112
6.15 The x-ray spectroscopy survey of the as-synthesized ZnO nanoseaurchins. The spectrum confirms the formation of ZnO. 113
6.16 The comparison of the I-V measurement of pure silicon and ZnO nanoseaurchins (a), the forward-reverse I-V measurement of the as-synthesized ZnO nanoseaurchins (b) and the observed UV switching response measured at 6 V (c). The sketch shows how the measurement was carried out (d). The red color on the substrate represents the metal contact. 114

List of Publications, Patent and Other contributions

1. **S. Jebril**, M. Elbahri, G.Titazu, K. Subannajui, S. Essa, F. Niebelschutz, C.-C. Roehlig, V. Cimalla, O. Ambacher, B. Schmidt, D. Kabiraj, D. Avasti, and R. Adelung, Integration of Thin-Film-Fracture-Based Nanowires into Microchip Fabrication, small 4 (2008) 2214.
2. **S. Jebril**, H. Kuhlmann, S. Müller, C. Ronning, L. Kienle, V. Duppel and R. Adelung: Epitactically Interpenetrated High Quality ZnO Nanostructured Junctions on Microchips Grown by the Vapor-Liquid-Solid Method, Crystal Growth and design 10 (2010) 2842.
3. **S. Jebril**, Y. K. Mishra, M. Elbahri, L. Kienle, H. Greve, E. Quandt, and R. Adelung: Using thin film stress for nanoscaled sensors, Materials Science Forum, 638 - 642 (2010) 2028.
4. Y.K. Mishra, **S. Jebril**, D. Agarwal, S. Mohapatra, R. Adelung, D. Avasthi, S. Ogale: Solid-vapour-solid growth of ZnO nanorods: A photo-switchable nanocomposite with tunable gold surface plasmons, Appl. Phys. Lett. submitted.
5. M.Elbahri, **S. Jebril**, S.K. Raudra, D. Cengher ,V. Cimalla,O. Ambacher, D. Paretkar, S.Wille ,R. Adelung: New route of nanowire integration in microfabrication processes for sensor applications, Nanofair 2005: New Ideas for Industry , 1920 (2005) 17.
6. M. Elbahri, **S. Jebril**, S. Wille, and R. Adelung: Simple ways to Complex Nanowires and Their Applications, Advanced in solid state physics, 48 (2009) 27.
7. D. Gedamu, **S. Jebril**, A. Schuchardt, M. Elbahri, S. Wille, Y. K. Mishra,

R. Adelung: Examples for the integration of self-organized nanowires for functional devices by a fracture approach, Physica Status Solidi b 1-10 (2010) 1.

8. H. Takele, **S. Jebril**, T. strunskus, V. Zaporojchenko, R. Adelung, F. Faupel: Tuning of electrical and structural properties of metal-polymer nanocomposite films prepared by co-evaporation technique, Appl. Phys. A 92 (2008) 345.

9. A. Lotnyk, L. Kienle, **S. Jebril**, Y.K. Mishra, R.Adelung and V. Duppel: A TEM investigation of twinning in ZnO nano-spikes, MC Graz: Materials Science, Verlag der TU Graz Volume 3 (2009) 187.

10. H. Takele, A. Kulkarni, **S.Jebril**, V S K Chakravadhanula, C. Hanisch, T. Strunskus, V. Zaporojtchenko and F. Faupel: Plasmonic properties of vapour-deposited polymer composites containing Ag nanoparticles and their changes upon annealing, J. Phys. D: Appl. Phys. 41 (2008) 125409.

11. M. Elbahri, D. Paretkar, K. Hirmas, **S. Jebril**, R. Adelung: Anti-Lotus Effect for Nanostructuring at the Leidenfrost Temperature, Adv. Mater., 19, (2007) 1262.

12. M. Elbahri, S. K. Rudra, S. Wille, **S. Jebril**, M. Scharnberg, D. Paretkar, R. Kunz, H. Rui, A. Biswas, R. Adelung: Employing Thin-Film Delamination for the Formation of Shadow Masks for Nanostructure Fabrication, Adv. Mater., 18 (2006) 1059.

13. R. Adelung, M. Elbahri, S.K. Rudra, A. Biswas, **S. Jebril**, R. Kunz, S. Wille, M. Scharnberg, Materials, Technology and Reliability of Advanced Interconnects-2005, MRS PROCEEDINGS, 863 (2005) 91.

14. R. Adelung, M. Elbahri, S.K. Rudra, A. Biswas , **S. Jebril**, R. Kunz, S. Wille, M. Scharnberg: Thin Films Stresses and Mechanical Properties XI, MRS Proceedings, 875 (2005) 289.

15. Y.K. Mishra, **S. Jebril**, D.C. Agarwal, S. Mohapatra, S. Singhal, D.K. Avasthi and R.Adelung: Au-ZnO: A tunable plasmonic nanocomposite for SERS and switching, CLEO/Europe, EQEC 2009- European Conference on Lasers and Electro-Optics and the European Quantum Electronics Conference (2009).

16. R. Adelung, **S. Jebril**, M. Elbahri, S. Rheder: ”Verfahren zur Erzeugung einer Mehrzahl regelmäSSig angeordneter, Nanoverbindungen auf einem Substrat” **Patent-Nr** DE102005056879A1.

17. M. Elbahri, **S. Jebril**, R. Adelung, S. Rehders: Verfahren zur Erzeugung einer Mehrzhal regelmäSSig angeordneter Nanoverbindungen auf einem Substrat, Deutsches **Patentamt**, 24.11.2006, PCT/DE 2006/002068 (internationale Nachmeldung).

18. **S. Jebril**, M. Elbahri, and R. Adelung: Integration of nanowires into microstructures by thin film fracture, Deutsche Physikalische Gesellschaft (DPG), Spring Meeting 2008, Berlin, Germany (**poster**).

19. **S. Jebril**, K. Subannanjui, M. Elbahri, and R. Adelung: Electrical Properties and Oxidation Behavior of Nanowires, Deutsche Physikalische Gesellschaft (DPG), Spring Meeting 2007, Regenesburg, Germany (**Talk**).

20. **S. Jebril**, M. Elbahri, R. Adelung: Possibilities and properties of nanowires integrated in microchips, Fulda 2007 (Talk).

21. **S. Jebril**, K. Subannanjui, M. Elbahri and R. Adelung: Electrical Properties and Oxidation Behavior of Nanowires integrated in microchips, SSP workshop 2007, Nordenay, Germany (**Talk**).

22. R. Adelung, **S. Jebril**, M. Elbahri, and D. Paretkar: Properties and simple Fabrication of Nanowire based devices, International Conference 2005, Hyderabad, India (**Talk**).

23. **S. Jebril**, H. Kuhlmann, S. Müller, C. Ronning, L. Kienle, V. Duppe, R. Adelung: High quality junctions by interpenetration of vapor liquid solid grown nanostructures for microchip integration, Deutsche Physikalische Gesellschaft (DPG), Spring Meeting, 2009, Dresden, Germany (**Talk**).

24. Y.K. Mishra, **S. Jebril**, D.C. Agarwal, S. Mohapatra, R. Singhal, D.K. Avasthi, R. Adelung, Au-ZnO: A Tunable Plasmonic Nanocomposite for SERS and Switching, European Conference on Lasers and Electro-Optics (CLEO-Europe-EQEC-2009), Munich, Germany (**poster**).

25. Y. K. Mishra, **S. Jebril**, D. C. Agarwal, S. Mohapatra, R. Singhal, D. K. Avasthi, and R. Adelung: Synthesis of Nanostructures for Functional

Applications, AvH Network Meeting, 2009, Bonn, Germany (**Poster**).

26. Y. K. Mishra, **S. Jebril**, D. Kabiraj, A. Tripathi, D. K. Avasthi and R. Adelung: Synthesis of nanostructures and their applications, Humboldt-Kolleg on Interdisciplinary Sciences, 2008, Slubice, Poland (**Poster**).
27. Y. K. Mishra, **S. Jebril**, R. Singhal, D. K. Avasthi, R. Adelung: Direct Synthesis of Zinc Oxide Nanoseaurchins and Nanocups from Zn-Powder, Dresden, Germany (**Talk**).
28. Y. K. Mishra, **S. Jebril**, D. C. Agarwal, V. S. K. Chakravadhanula, S. Mohapatra, V. Zaporojtchenko, D. K. Avasthi, R. Adelung and F. Faupel: Noble metal-polymer nanocomposites as plasmonics and optoelectronics , 4th International Workshop on Polymer/Metal Nanocomposite 2009, Prague, Czech Republic (**Talk**).